Crystal structures and magnetism in jarosites: model *kagomé* antiferromagnets

William Geoffrey Bisson

Thesis for the Degree of Doctor of Philosophy
UCL

April 5, 2011

I, William Bisson, confirm that the work presented in this thesis is my own. Where information has been derived from other sources, I confirm that this has been indicated in the thesis.

William Bisson

Abstract

Jarosites are a family of minerals with the general formula $AFe_3(SO_4)_2(OH)_6$ ($A = H_3O^+$, NH_4^+, K^+, Na^+, Rb^+, Ag^+, $\frac{1}{2}Pb^{2+}$). Long known to earth scientists and the mining community, jarosites provide the most studied examples of model *kagomé* magnets: materials where the magnetic exchange interactions are frustrated by the *kagomé* geometry of vertex-sharing triangles. In most jarosites this frustration is insufficient to prevent the formation of magnetic order at low temperatures and two ordering transitions are observed. The primary transition at $60 < T_{N_1}/K < 65$ is to an umbrella spin structure, which flops into the *kagomé* plane at the secondary transition, T_{N_2}, between 45 and 55 K. The exception to this behaviour is hydronium jarosite ($A = H_3O^+$) which instead undergoes a critical freezing transition to an unconventional spin glass state at a much lower temperature, $T_g \sim 17$ K.

This thesis presents studies of the chemistry, crystallography and magnetism of the jarosites with the general aim of relating the observed magnetic responses to their chemistry and crystal structures. The investigations presented here concentrate on hydronium jarosite and relate the changes to the synthesis chemistry and crystal chemistry to the spin-glass transition temperature. A combination of powder and single-crystal X-ray diffraction and SQUID magnetometry are used to show that the spin-glass transition in hydronium jarosite is correlated to the degree of distortion of the coordination around the moment bearing Fe^{3+} ions. Samples with the most symmetric coordination of the magnetic Fe^{3+} ions feature the lowest values of T_g. As the defining influence in spin glasses is typically thought to be disorder, this observation is remarkable. Further, these studies show that in hydronium jarosite the key to the spin glass transition is a uniform (translationally invariant) energy scale that is associated with the crystallographic distortion. In so doing, they support the proposal that the spin-glass transition in hydronium jarosite is driven by anisotropy.

Further, elemental analyses show that the Fe stoichiometry has little effect upon the displayed magnetic properties of the jarosites. Rather, these are found to be most sensitive to small crystallographic changes in the Fe–O coordination octahedra associated with substitution of the A-site cation. In terms of the ratio between the Fe–O equatorial and apical bond lengths, greater deviation from O_h symmetry is shown to correlate with higher values for T_g and T_{N_2}.

Contents

List of Figures

List of Tables

Acknowledgements

The following people have made a valuable contribution to this work and whom I am pleased to have met throughout this work.

Royal Institution / UCL

Ian Watts (piecing back together any destruction I caused), Andrew Wills (supervisor), Mark Green (2nd supervisor), Adrian Smith (jarosites, ICP and Mulligan's), Mike Sheehy (work shop), Jeremy Cockcroft (crystallography and proof reading), Simon Jaques (proof reading and pal) Mark Ellerby (SQUID), Olivier Leynaud (Rietveld), Kevin Reeves (SEMs), Andrea Taroni (discussions on XY), Adeline Grace (help), Wing-Yen Li (help), Carolina Arevalo (support), Vesna Middlekoop (printing) and finally Richard Catlow (giving me the opportunity).

Elemental Analysis

Jacqui Duffet (ICP, Royal Holloway), Emma Tomlinson (ICP, Royal Holloway) and Jeanette Elizabeth Barker (ICP advice).

Neutron scattering

Kevin Knight (HRPD, ISIS) and Thomas Henson (D20, ILL)

Single Crystal - Southampton and Newcastle Universities - a very big thank you for the efforts made, in particular Simon Coles (Southampton), Bill Clegg (SRS), Richard Harrington (SRS) and Richard Stephenson (Southampton)

Chapter 1

Introduction

This thesis involves the synthesis, crystallographic and magnetic studies of jarosites, a subgroup of the alunite family with the general formula $AFe_3(SO_4)_2(OH)_6$, where A is typically a univalent cation. Jarosites have been broadly researched but with particular motivation coming from their ability to incorporate ions into their structure [1], and their application in the mining industry for the removal of unwanted metal ions [2]. As a result, the chemistry of jarosites has been comprehensively reviewed [1–24]. More recently, jarosites have been the subject of research in fundamental magnetism, as the Fe^{3+} ions ($S = \frac{5}{2}$) within the jarosite structure provide the best known examples of the 2-dimensional network of vertex sharing triangles known as the *kagomé* network. Antiferromagnetically coupled ions with this structure are highly frustrated, a characteristic which can lead to exotic electronic states [21].

Frustration in magnetism came to prominence after Anderson proposed that it was a key requirement for the resonating valence bond model of superconductivity [25–28]. Since then many frustrated materials have been synthesised in an effort to investigate what new and exotic electronic states are possible. Much of this work has concentrated on geometrically frustrated materials where the frustration arises from the geometry of the magnetic exchange. Such magnets typically feature very high frustration [29, 30], defined empirically by the degree of suppression of the ordering temperature with respect to the Curie-Weiss temperature [31]. This frustration of magnetic order can generate very interesting physics, and experimentally observed magnetic ground states include spin ice [32, 33], spin liquid [34] as well as unconventional spin glasses [35, 36].

1.1 Aims of this work

The principal aim of the project was to investigate the existence and effects of anisotropy upon *kagomé* antiferromagnets by careful examination of jarosites [37]. This family of materials was chosen because they have been extensively studied and shown to display both conventional magnetic order and exotic spin glass-like behaviour [36, 37]. These experimental studies are focused on the spin glass transition in hydronium jarosite and its differences to the other members of the series that undergo ordering transitions to a Néel state [37].

It is important to determine the effects of nonstoichiometery on the jarosite structure, to understand how the crystal structure and chemical environment affect the magnetism within jarosites. To achieve this, detailed elemental analysis was used together with chemical studies to explore and adapt different synthetic routes for jarosite formation. In turn, the structural differences between the various jarosites were studied using a combination of X-ray (single-crystal and powder) and neutron (powder) diffraction techniques.

1.2 Outline of thesis

In this chapter a brief summary of jarosites is given followed by a discussion of some basic magnetic concepts. The theory behind the magnetic concepts introduced here is discussed in more detail in Chapter 2.

Chapter 3 describes the different synthetic routes used to make the samples discussed in Chapter 4. Two varieties of hydrothermal synthesis are introduced, namely forced hydrolysis and oxidative methods. The use of oxidative methods is particularly interesting as it has allowed growth of the highest quality non-hydronium jarosites. The inability to grow hydronium jarosite via this technique demonstrates that the chemistry of its formation is unlike that of other jarosites. This observation, together with the data on chemical analysis and crystallography, are discussed in relation to the magnetism in Chapters 6 and 8.

A wide range of techniques have been employed in the analysis of the chemistry and crystallography of the jarosites studied in this thesis, *e.g.* synthesis and crystallite morphology (Chapter 4) and elemental composition (Chapter 6), lattice parameters (Chapter 7), and more detailed single-crystal crystallography (Chapter 8). Further, the analysis of powder neutron data is presented in order to reveal

the structural changes at the magnetic transitions and to determine the location of the deuterium atoms (Chapter 9) in H/D substituted samples.

The conclusions are then presented in Chapter 10 together with a brief summary and overview of the work carried out in this project.

1.3 Jarosites

Jarosites have been utilised for over 2000 years by man and are of great economic importance, despite being only secondary minerals formed through the weathering of pyrite, FeS_2 [38, 39]. The silver member of the family, argento jarosite, believed to be sourced from the Rio Tinto excavations in southern Spain, was traded in early history by the Phoenicians as a source of silver [40]. The jarosite name comes from the Barranco del Jaroso ravine in the Sierra Almagrera near Almeria (Spain), where it was first classified as a mineral in 1852 [41].

The chemistry of jarosite formation has been extensively researched because of the environmental impact that Acid Mine Drainage (AMD) has on local lotic systems adjacent to mine tailings; the presence of jarosite is evidence of AMD [14, 38, 39, 42–47]. Jarosite precipitation occurs where there are high concentrations of aqueous Fe^{3+} ions in low pH (< 2) conditions [3]. The problems associated with AMD instigated considerable research into the formation and dissolution of jarosites because of its ability to uptake many ionic species as a result of its changing stoichiometry, enabling the transport much further afield of toxic elements such as Pb, As, Hg and Tl [3, 4, 9, 14, 48].

The importance of jarosite continues to the present day with its precipitation providing a mechanism to remove waste deposits during zinc purification and refinement processes [7, 8]. The discovery of jarosite on Mars by the NASA MER-B Rover provides evidence that water was once present on Mars, because the jarosite structure contains a high water content [46, 49].

The alunite structure has the idealised formula $AB_3(SO_4)_2(OH)_6$, (A=H_3O^+, NH_4^+, K^+, Na^+, Rb^+, Ag^+, $\frac{1}{2}Pb^{2+}$ or Tl^+) where B=Fe^{3+} for jarosite and B=Al^{3+} for alunite [3]. The B-site can also be substituted for Cr^{3+} or V^{3+} [37]. Their crystal structure is best described in space group $R\bar{3}m$ [50], though there has been some debate whether the alunite/jarosite structure is centrosymmetric from infrared spectroscopy studies [51]. The jarosite structure is able to uptake a wide range of elements [1, 4, 7], suggesting that significant structural disorder may well be stable.

1.4 Magnetism

The topic of magnetism has a long and complicated history with many myths associated with the early discoveries of magnetic materials. Lodestone, the magnetised form of Fe_3O_4 was the first example of a ferromagnet material.

William Gilbert wrote the first authoritative text on the phenomena of magnetism in 1600 [52] and made two very important observations. Firstly, that Lodestone has a dipole, which led him to suggest that the Earth must also possess a dipole, thereby explaining why compasses pointed north. Secondly, the observation of what is now known as the Curie point, T_C through the heat working of iron. It was observed as the iron was cooled down after being heated to a very high temperature that the metal became magnetised. Above the Curie point iron will behave as a simple paramagnet with randomly oriented magnetic moments. Upon cooling through the Curie point spontaneous symmetry breaking occurs and all the moments align themselves in a particular direction giving rise to a very strong magnetisation. On further cooling far below T_C the magnetisation increases until the system reaches full magnetic saturation at T=0 K, where only quantum fluctuations remain to disrupt the magnetic order.

The magnetisation of ferromagnets increases rapidly with applied field until a value is reached at which it saturates. The magnetisation remaining after the external field is removed is termed the spontaneous magnetisation. According to the Curie Law, upon heating above the ferromagnetic ordering temperature the magnetisation decreases with increasing temperature in a form that is inversely proportional to temperature.

Another class of magnets are the antiferromagnets. Here the magnetic moments align in such a way as to produce zero net magnetisation in the absence of an applied field. There are many ways to achieve this type of situation, such as a simple head-to-toe arrangement of the moments, but more complex structures can also exist, such as helical and cycloidal ordering. On cooling through the Néel temperature [53] a transition from the paramagnetic to the antiferromagnetic state occurs which is marked by a maximum in the magnetic susceptibility. Antiferromagnets are quantified with a Néel temperature, T_N, and a Weiss temperature, θ_W, which is negative (θ_W is positive for ferromagnets). The magnitude of the Weiss temperature indicates the strength of the correlations between the moments.

At the atomic level an individual magnetic moment arises from the combination

of the orbital angular momentum, **L**, and the spin angular momentum, **S**. The phenomena briefly described above are determined by exchange interactions between atoms or ions that possess the magnetic moments associated with these angular momenta. The exchange interactions, represented by the symbol J, between individual moments are mediated by the chemical bonds of a system, be they metallic, ionic, covalent or dative. Direct interactions between the magnetic dipoles of the moments also exist, but these are typically far weaker in energy than those mediated by the chemical interactions of atoms and ions. Ultimately, understanding the finer details of the moment and the interactions with its neighbours are crucial to determining the energy scale that drives the system to a given electronic ground state.

1.5 Spin glasses

This project explores a new electronic ground state - the *kagomé* spin glass [21, 36] - and the reasons for its formation. Spin glasses have traditionally been considered to result from a combination of two components: disorder (site vacancies, doping, distortions, or random exchange interactions and exchange pathways) and magnetic frustration [54].

In magnetism, frustration refers to the inability of a system to satisfy all of the individual exchange interactions. This leads to a ground state that is therefore raised in energy with respect to the unfrustrated analogue, such as a ferromagnet. The consequences of frustration are far reaching as its presence changes the nature and temperature of critical transitions and forces the system to adopt unusual ground states. Spin glasses are a good example of how magnetic frustration can produce a system that is continually evolving, moving from one ground state to another on time scales from almost instantaneous to infinity [54]. Spin glasses are governed by kinetics and display out-of-equilibrium dynamics, analogous to other systems including protein folding [55] and neural networks [54, 56]. Hence, their study can provide important insight into more complex physical systems.

The possibility of a spin glass where disorder is negligible or its effects are insignificant is of tremendous interest. Such a system would display properties that are therefore the result only of its magnetic frustration. In this case its spin glass behaviour could be different in nature from canonical spin glasses [36, 57]. These differences may appear slight, but they could also be fundamental [36].

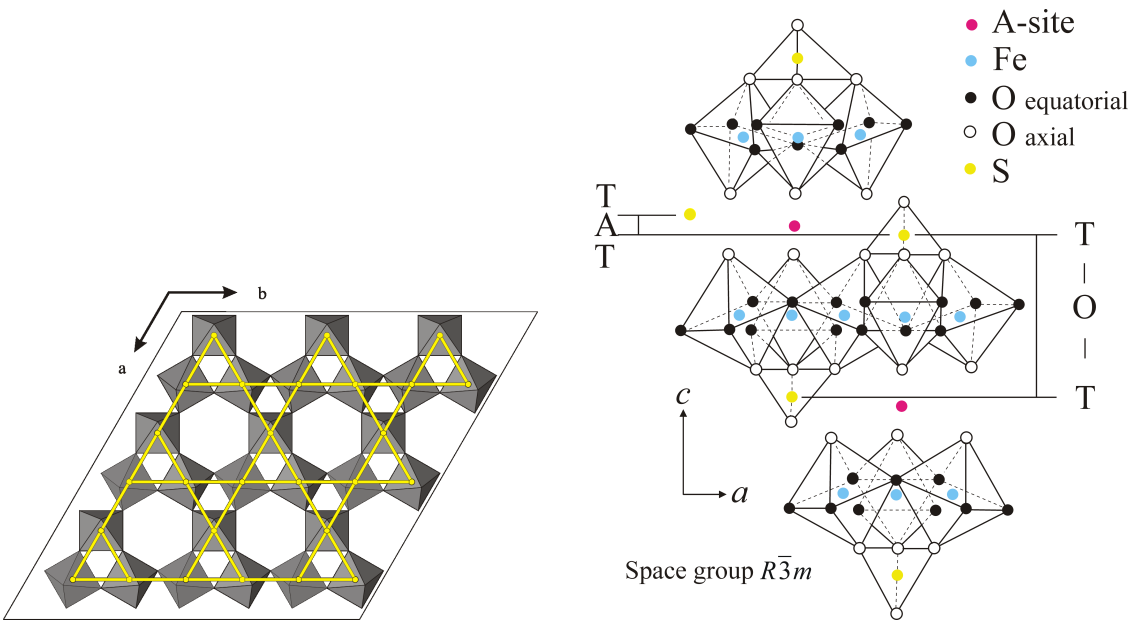

Figure 1.1: a) view of the jarosite structure along the c axis showing the canted Fe octahedra and the *kagomé* network overlaid to show the arrangement of the Fe^{3+} ions. b) a polyhedral representation of jarosite, where the bridging hydroxyl groups (●) situated just above and below the *kagomé* plane, lead to form a canted Fe-coordinated octahedra. The degree of canting has important consequences for the magnetism of the jarosite structure.

1.6 Jarosites - model *kagomé* antiferromagnets

Possibly the most highly frustrated 2-dimensional magnets are those based on the *kagomé* network: a network of vertex sharing equilateral triangles. The name *kagomé* derives from a form of Japanese basket weaving bearing this motif as shown in Figure 1.1(a). Jarosites provide the most studied realisations of this network [18–22,29,37,58–63]. In them, moment-bearing Fe^{3+} ions form layers of vertex sharing triangles making up the *kagomé* network as shown in Figure 1.1(b). The Fe^{3+} ions are bridged together by hydroxyl groups situated slightly above and below the *kagomé* plane. The bridging hydroxyl groups mediate the magnetic exchange between the Fe^{3+} ions to produce an antiferromagnetic exchange between the ions. The Fe-O coordinated octahedra are capped above and below by tetrahedrally coordinated sulphate groups to form the T-O-T sheets shown in Figure 1.1(b). Separating each of these T-O-T layers is the 12 coordinate site where the A-site ions resides that form the T-A-T sheet (Figure 1.1(a)). The *kagomé* layers of Fe^{3+} ions are therefore sufficiently separated that the magnetic system is essentially 2-dimensional.

In trying to understand the spin glass transition in hydronium jarosite and the

conventional magnetic ordering in the non-hydronium jarosites, this thesis gives evidence for crystallographic distortions that can relieve the frustration associated with the *kagomé* lattice. This then provides a simple explanation for the temperature dependence and nature of the magnetic transitions displayed for the iron jarosites.

Chapter 2

Theoretical background

The theory section will introduce the concepts related to the investigations into magnetism undertaken in this work. It begins with the Curie Law and Curie-Weiss Law, moves onto the theory of phase transitions and symmetry breaking, before introducing spin glasses, geometric frustration and *kagomé* systems. Finally, experimental model *kagomé* antiferromagnets, including the jarosites, are introduced.

2.1 Curie Law

All materials respond to a magnetic field: either a positive interaction where lines of magnetic flux concentrate in the material or a negative response where the material seeks to expel magnetic flux. Such materials are respectively known as paramagnets or diamagnets. The paramagnetic response results from unpaired electrons whereas diamagnetic samples are a result of paired electrons and using the simplification of Lenz's law seek to expel magnetic flux. Diamagnetic susceptibility is small and negative, independent of temperature and field strength, and is cumulative. The notable exceptions to this behaviour are superconductors, which are extraordinarily strongly diamagnets due to the Meissner effect.

In paramagnets an applied magnetic field $\boldsymbol{H}$ induces a linear response, termed the magnetisation, $\boldsymbol{M}$, that is proportional to $\boldsymbol{H}$:

$$\boldsymbol{M} = \chi \boldsymbol{H} \tag{2.1}$$

where χ is the magnetic susceptibility, a dimensionless fundamental parameter. In the paramagnetic region the susceptibility is described simply by the Curie law (2.2) where the susceptibility is inversely proportional to temperature:

$$\chi = \mathrm{C}/T \tag{2.2}$$

where C is the Curie constant, which is sample dependent. The Curie law provides the simplest approximation to the behaviour of a paramagnet and only applies to dilute magnetic systems where the separation between magnetic ions is large, or at high temperatures where thermal fluctuations are far stronger than the magnetic interactions.

The relationship between magnetisation, $\boldsymbol{M}$, and magnetic field, $\boldsymbol{B}$, expressed with regard to the Curie constant and the susceptibility, χ, is given in equation 2.3.

$$\frac{\boldsymbol{M}}{\boldsymbol{B}} \cong \frac{NJ(J+1)\mathrm{g}^2\mu_\mathrm{B}^2}{3k_\mathrm{B}T} = \frac{\mathbf{C}}{T} = \chi \tag{2.3}$$

The Curie constant rewritten in a form traditionally used by inorganic chemists is shown in (2.4a). From this the susceptibility, χ, can be used to give a direct measure of the effective moment (2.4b).

$$\mathbf{C} = \frac{N\mu_{eff}^2}{3k_\mathrm{B}} \tag{2.4a}$$

$$\mu_{eff}^2 = \mathrm{g}^2 J(J+1)\mu_\mathrm{B}^2 \tag{2.4b}$$

where g is the Landé g-factor

$$\mathrm{g} = \frac{3}{2} + \frac{S(S+1) - L(L+1)}{2J(J+1)} \tag{2.5}$$

and μ_B is the Bohr magneton, given as

$$\mu_\mathrm{B} = \frac{e\hbar}{2m_e c} = 2.9732 \times 10^{-21}\mathrm{erg\ Oe}^{-1} \tag{2.6}$$

For spin-only systems, g=2.0023, the equation for the effective moment, μ_{eff}, is commonly rewritten as:

$$\mu_{eff} = \mathrm{g}[S(S+1)]^{\frac{1}{2}}\mu_\mathrm{B} \tag{2.7}$$

The reader may wish to read the derivation of the Curie constant by referring to the text book by R. Carlin [64].

2.2 Curie-Weiss Law

A simple extension to the Curie law that accounts for interacting magnetic moments is the Curie-Weiss law (equation (2.8)):

$$\chi = \frac{\mathrm{C}}{T_{\mathrm{C}} - \theta_{\mathrm{W}}} \tag{2.8}$$

where the T_{C} term represents the Curie point, and θ_{W} is the Weiss temperature. The sign of θ_{W} characterises the nature of the magnetic interactions of the system: $\theta_{\mathrm{W}} > 0$ and $\theta_{\mathrm{W}} < 0$ for ferromagnetic and antiferromagnetic interactions, respectively. The magnitude of θ_{W} characterises their strength, *e.g.* for the iron jarosites values of $\sim -800\,\mathrm{K}$ [20, 65] to $\sim -1200\,\mathrm{K}$ [36, 37] have been reported; this thesis reports values closer to $-1500\,\mathrm{K}$.

2.2.1 Magnetic Anisotropy

Fundamental to our descriptions of magnetic systems are the degrees of freedom of the spins. Limitations away from spherical (Heisenberg) symmetry are broadly classified into anisotropies and can result from a combination of the spin-orbit interaction and the Crystal Field (CF). Writing the Heisenberg Hamiltonian as:

$$\mathscr{H} = -J \sum_{<ij>} S_i \cdot S_j, \tag{2.9}$$

positive J favours a parallel alignment of spins (ferromagnetism) while negative J favours an antiparallel arrangement (antiferromagnetism). A modification to this that describes a strong uniaxial anisotropy that constrains the moments to be along a specific direction (Ising character) can be written:

$$\mathscr{H} = D \sum_{i} (S_i^z)^2 \tag{2.10}$$

where D is negative. When D is positive the spins are forced to lie within a plane perpendicular to the z direction. This situation is termed XY anisotropy.

A final type of behaviour that behaves like an anisotropy, but has its origins in antisymmetric superexchange, is the Dzyalonshinky-Moriya interaction (DMI) [66, 67] ((2.11))

$$\mathscr{H}_{ij}^{\mathrm{DMI}} = -\mathbf{D}_{ij} \cdot (\mathbf{S}_i \times \mathbf{S}_j) \tag{2.11}$$

The $\mathbf{D}_{ij}$ is non-zero only if the centre of the non-magnetic bridge that mediates the super exchange is not an inversion centre. Unlike uniaxial symmetry that gives a preferred axis, DMI breaks time reversal symmetry and therefore its net effect is to ensure all the spins align in a single direction, frequently generating a ferromagnetic component.

2.2.2 Dimensionality and magnetic ordering

Magnetic systems provide relatively simple models with which to study critical phase phenomena including critical exponents and order parameters, and the effects of lattice dimensionality (d) and spin dimensionality (D). These last two characteristics which define the connectivity of the interactions and the degrees of freedom of the spins themselves, are responsible for both the nature of the magnetic ordering transition and its critical exponents, as summarised in Table 2.1. Through the principle of Universality the details of the ordering process for these magnetic systems will be the same as for other physical systems that feature the same dimensions of lattice connectivity and local degrees of freedom, such as the movement of atomic displacements at crystallographic phase transitions.

Table 2.1: A summary of whether a magnetic ordering transition can occur as a function of lattice and spin dimensionality. $\Diamond$ and $\times$ indicate systems that do or do not achieve long range order, respectively. $\odot$ indicates a particular type of phase transition observed in 2-dimensional XY magnets, termed a Kosterlitz-Thouless (KT) transition.

	$d=1$	$d=2$	$d=3$
Ising (D=1)	$\times$	$\times$	$\Diamond$
XY (D=2)	$\times$	$\odot$	$\Diamond$
Heisenberg ($D=3$)	$\Diamond$	$\Diamond$	$\Diamond$

Of particular interest for the 2 dimensional *kagomé* network is the Kosterlitz-Thouless transition (KT) [68] that occurs in XY systems, and is characterised by the binding and unbinding of vortices of spins (Figure 2.1), and this will discussed further in Section 2.5.

2.3 Spin Glasses

Spin glasses are systems where the competing interactions associated with frustration lead to a multitude of near degenerate ground states which are separated by

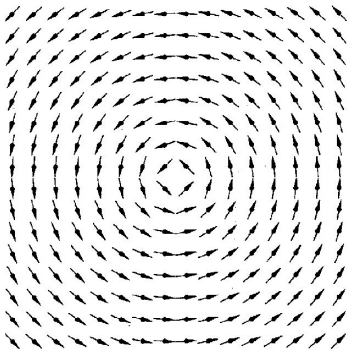

Figure 2.1: A simple depiction of a vortex of spins. The spins are centred around a point and there is high associated entropy with the development of vortices, $S = k_{\mathrm{B}} \ln[(N/a)^2]$, because number of points of creation increase with the size of the system.

energy barriers, such that the system cannot achieve a unique ground state and ergodicity is broken. They are therefore exotic states of matter that continue to evolve below the spin-glass freezing temperature, as evidenced by the relaxation of the remnant magnetisation over a wide range of timescales from the microscopic to millennia [54, 56, 69].

2.3.1 Traditional picture of frustration and random exchange

Frustration is an intrinsic component for spin glasses, though frustration can occur in many magnetic examples without leading to spin-glass behaviour. Frustration refers to the inability of the system to minimise simultaneously each of the independent terms in the magnetic Hamiltonian [70]. Such competing interactions can arise from an interference between a mixture of ferromagnetic and antiferromagnetic exchange pathways, or more simply, from the geometry of the system. In general, frustration leads to degeneracies that are only broken when smaller energy scales are brought into account, such as further-neighbour exchange. The breaking of degeneracies commonly facilitates the formation of conventional magnetic order, but there are situations where this is incomplete and some degeneracies survive.

The inability of a system to reach its lowest-energy ground state can cause produce unexpected properties. Research into frustrated systems began in ernest with the intense interest in spin glasses during the 1950s and 1960s. Frustration as a topic was reinvigorated after the discovery of the High Temperature Superconductors (HTS) which saw the current BCS theory (Bardeen, Cooper, and Schrieffer) [71] on superconductivity fail for many reasons, but primarily because the band gap in

the cuprates is greater than 50 meV and is beyond any phonon contribution [72]. P. W. Anderson suggested that underlying the electronic ground state of the new HTS was frustrated and that the ground state is similar to antiferromagnetically coupled ions arranged to form a triangular lattice [27]. The early 1990s witnessed an explosion in publications concerning magnetic frustration, many centred on systems where the geometric arrangements of moments produces frustration – so-called *geometrically frustrated magnets* – and their exotic behaviours (Section 2.4).

Before studies into geometrically frustrated magnetism developed, spin glasses were the main areas of research into frustrated magnets. The spin-glass phenomena were originally found in doped metal alloys, AuFe and CuMn, where small quantities of Fe or Mn can produce the spin glass phenomenon. At small levels of doping Fe distances would be too great to interact with each other and instead other phenomena, such as the Kondo effect [73] or weak moments, or the opposite effect, giant moments can be produced. It is only when the long range effects (20-30 Å) of the RKKY [74] interaction become involved that competition between moments occur. The oscillatory nature of the RKKY is dependent upon the separation of the impurity moments and creates both antiferromagnetic coupling and ferromagnet coupling, giving rise to competing interactions. As the doping increases so the proximity of the impurities will be closer and shorter range interactions will begin to dominate resulting in potential long range order [54]. In the limit of low dopant concentrations the susceptibility of an impurity, χ, oscillates with distance r, according to

$$\chi_{(0)}(r) \propto \frac{cos 2k_F r}{r^3}, \qquad 2k_F r \gg 1 \tag{2.12}$$

in the limit where r is large, thus $2k_F r \gg 1$ (k_F is the Fermi momentum).

These doped metal alloys provide all the necessary attributes to produce a spin glass because of the random distribution of the impurity ions which in turn gives rise to a random mixture of exchange interactions all competing with one another. It is a commonly held view that such randomness (either site or bond) is necessary, along with frustration, in order to make the complex structure of energy landscapes that lead to a spin glass [54, 75].

Covalently bonded materials provide other important directions for spin-glass research as extraordinarily high levels of magnetic frustration can be engineered. While such spin glasses are still commonly thought of as arising from a randomness in exchange, this thesis supports the idea that spin-glass behaviour can occur in a highly frustrated manifold *without significant disorder*, such as in the *kagomé*

antiferromagnet hydronium jarosite (Section 2.4.4).

2.3.2 Energy landscapes of canonical spin glasses

The properties of a spin glass are commonly understood in terms of a complex energy landscape with many valleys of energy minima, some stable, some metastable, as shown in Figure 2.2. The relaxation of the spin glass then corresponds to some random or biased (if a magnetic field is applied) walk through the accessible energy minima. As each different energy minima will display its own thermodynamics, it is not possible to describe spin glasses with a single order parameter and averages must be employed. Section 2.3.4 describes further the challenges of averaging needed to characterise the complex range of energetics associated with spin glasses.

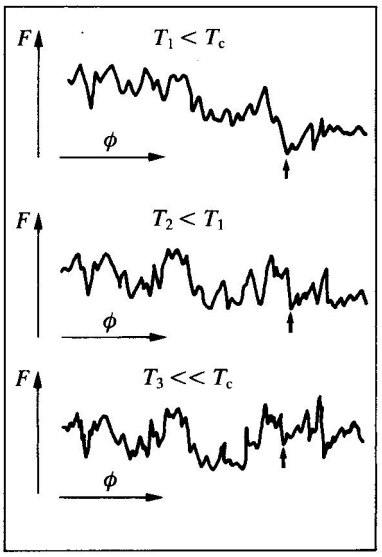

Figure 2.2: As the temperature of a spin glass system continues to fall below T_C more metastable states become accessible to the system. F is the free energy of the system and Φ is a coordinate of phase space. The arrow marks the ground state determined from a higher temperature regime, as the temperature is reduced, many more potential ground states appear [76].

2.3.3 Magnetisation measurements

Common experimental signatures of a spin glass are a separation between the dc field cooled (FC) and zero field cooled (ZFC) magnetisation measurements, as shown in Figure 2.3. It should be noted that the time-dependent response associated with spin glasses means that the freezing temperature depends on the frequency of the

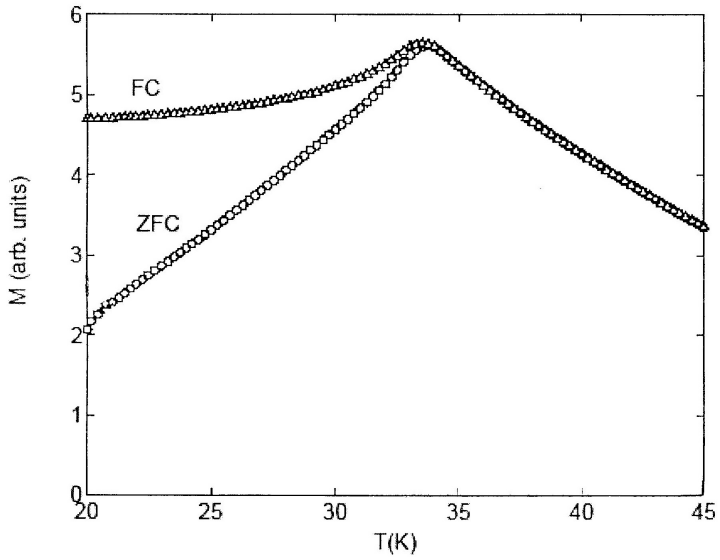

Figure 2.3: χ_{dc} measurements showing the separation of ZFC and FC responses of the metal alloy spin glass AgMn. Below the spin glass freezing transition, T_g, there is a separation in the measurements showing the onset of irreversibility [77].

measuring probe [54]. In dc magnetisation studies it is commonly taken as the temperature at which separation occurs between the FC and ZFC measurements.

Another physical property of a spin glass is remanence; in effect memory for previous ground states the system was in. This is discernible in hysteresis measurements below T_g, where the field is reversed from +ve through zero to a −ve field; here the sample magnetisation changes continuously from being positive, through zero (at the remnant field), to being of the same sign as the current applied field.

2.3.4 Edwards-Anderson model

Deriving an order parameter for spin-glass systems is extremely difficult considering the out of equilibrium dynamics associated with spin glasses, and advanced statistical mechanics must be used to describe the average associated with the large number of metastable states. The basis for the current models of spin glasses is the Edwards-Anderson (EA) model.

The (EA) model [78] is an extension of the RKKY model of oscillating exchange in a metallic sea of conduction electrons that encompasses properties including bond randomness in systems such as in $Eu_xSr_{1-x}S$, but in reality is a simplification of it. Here the distribution in J_{ij} is taken to arise from random (quenched) disorder and to have a Gaussian distribution. The great complexity of the magnetic interactions

can then be hidden within the standard Hamiltonian (2.13)

$$\mathscr{H} = -\frac{1}{2}\sum_{ij} J_{ij}\mathbf{S}_i \cdot \mathbf{S}_j \tag{2.13}$$

with the core difficulty being the averaging of the partition functions over this Gaussian distribution. This was achieved by the introduction of the so-called replica trick, which involves the representation of disordered bonds in terms of a set of identical replicas of the system. A more conventional simplification can be added, by making the magnetic interactions infinite range (thereby making the model compatible with mean-field theory, and consequently exact) and reducing the spin dimensionality from that of Heisenberg spins to those with Ising symmetry, as only one component is needed to define $\mathbf{S}_i$. This latter model is known as the SK model, after its developers Sherrington and Kirkpatrick [79]. The distribution of J_{ij} depends on the lattice vector separation $\mathbf{R}_i - \mathbf{R}_j$ giving rise to equation (2.14)

$$\left[J_{ij}^2\right]_{av} \equiv \delta_{ij} \equiv \delta(\mathbf{R}_i - \mathbf{R}_j) \tag{2.14}$$

where $[\,]_{\mathrm{av}}$ denotes averaging and δ_{ij} is in the infinite range so that it can be equated to mean field theories.

The success of the EA model was remarkable as it gave spin glasses a theoretical foundation, and enabled the definition of an order parameter q in the mean field limit. As there is no long range spatial order, the EA order parameter, q_{EA}, is based upon the autocorrelation function:

$$q_{\mathrm{EA}} = \lim_{t\to\infty} \langle\langle \mathbf{S}_i(0) \cdot \mathbf{S}_i(t)\rangle_{\mathrm{T}}\rangle_{\mathrm{C}} \tag{2.15}$$

where the inner and outer brackets represent thermal (T) and configurational averaging (C) respectively over all spins. q_{EA} will be zero, for ergodic systems, representing a paramagnet; and in a vanishing field, where this model breaks down. A value of $q_{\mathrm{EA}} \neq 0$ indicates that the system is trapped in an energy valley and is a measure of the local spontaneous magnetisation averaged over all the valleys. At short time scales where the system has not yet begun traversing the energy landscape q_{EA} is physically relevant. This is not the case of spin-glass systems where the system will evolve and travel from ground state to another ground state and thus more than one order parameter will be needed to describe a spin-glass system.

More advanced descriptions that are beyond the EA and SK models are needed

in order to ensure broken ergodicity is achieved in zero-applied field. Rather than go into details of the elaborate mathematics that these models involve, the comment will simply be made that better descriptions of spin glasses require far more complex order parameters, q, and that these continue to challenge theory. A great simplification to the theory of spin glasses would be possible if models without disordered Hamiltonians could be found that display glassy dynamics. The *kagomé* antiferromagnet with finite anisotropy is a potential candidate for this role and is consequently of great interest (Sections 2.6.2 and 2.7.3).

2.4 Geometrically frustrated magnets

2.4.1 Simple model of competing ferromagnetism and antiferromagnetism

It is important to stress that random exchange interactions are not the sole way of producing frustration. A simple disparity in the sign of the coupling between magnetic sites can lead to competition between exchange interactions and the generation of frustration. A simple example of this, is a square lattice with differing antiferromagnetic interactions as exemplified in Figure 2.4. It is evident that within this exchange topology, any system with an odd number of ferromagnetic bonds will be frustrated.

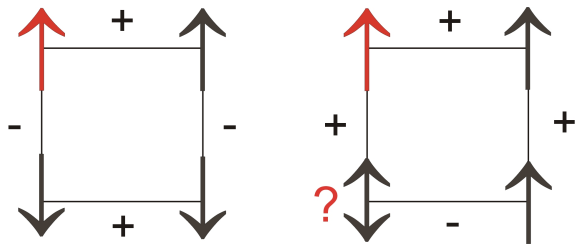

Figure 2.4: Simple depiction of a frustrated lattice through competing interactions. Following the interactions between the moments in a clockwise direction from the red coloured moment, the left plaquette with alternate ferro and antiferromagentic interactions leads to long range magnetic order. The right plaquette with a single antiferromagnetic interaction amongst three ferromagnetic interactions leads to the final moment to become frustrated as it can no longer satisfy the two interactions.

2.4.2 The frustrated triangle

Moving on from systems with a mixture of competing ferromagnetic and antiferromagnetic interactions, antiferromagnets are capable of being frustrated. As such systems feature only a single type of exchange interaction, and perhaps only one type of magnetic ion, they provide relatively simple examples of frustrated magnets. In these cases the frustration arises from the geometry of the magnetic lattice and its interactions, and is consequently referred to as *geometric frustration*.

The starting point for their understanding is a set of antiferromagnetically coupled ions arranged upon a single triangle. It is clear that all of the pairwise exchange interactions cannot be minimised simultaneously as it is not possible for all the spins to be antiparallel with both of its neighbours (Figure 2.5 a). The ground state of such a system is a compromise, where the moments align themselves 120°. This canting away from a unique direction leads to the formation of two distinct chiral forms [80] (Figure 2.5 b) – defined by κ, taken from the vector products of spins in a clockwise direction [81, 82]:

$$|\vec{\kappa} = \frac{2}{3\sqrt{3}}[\mathbf{S}_1 \times \mathbf{S}_2 + \mathbf{S}_2 \times \mathbf{S}_3 + \mathbf{S}_3 + \mathbf{S}_1]| \tag{2.16}$$

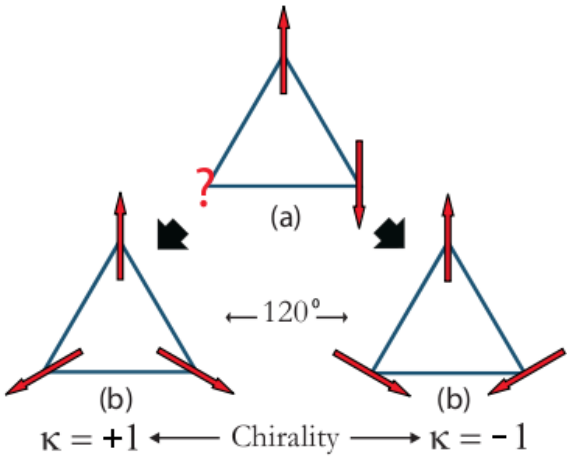

Figure 2.5: a) the system's inability to simultaneously minimise all the exchange interactions leads to frustration as shown by the third spin. b) shows two distinct compromise arrangements where the moments are oriented 120° from each other. This introduces the concept of chirality defined by κ: taking the vector product in a clockwise direction leads to either $\kappa = +1$ or $\kappa = -1$.

2.4.3 Triangular Lattice

How the triangles are tessellated to make an extended lattice dictates the degeneracy of a macroscopic system. Tiling based on edge-sharing will not further enhance the degeneracy as the sharing of two moments between triangles fixes the relative spin orientations (Figure 2.6). The spin structure is therefore coherently propagated through the lattice and the degeneracy of the system is the same as that of a single triangle, *i.e.* $\times 2$.

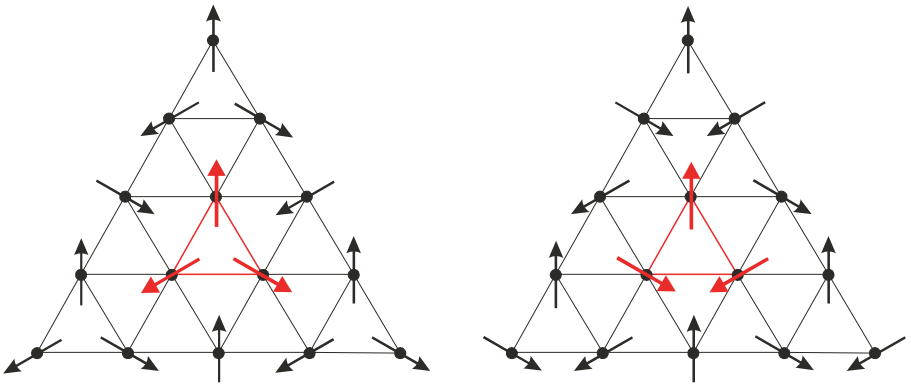

Figure 2.6: Two diagrams show a red triangle at the centre of an edge sharing lattice of triangles with moments placed at the vertex of each triangle. The red triangles represent the two different chiral forms of antiferromagnetically coupled ions, each moment aligned 120° from each other. Maintaining the 120° alignment the chiral form of the red central triangle propagates coherently throughout the structure because each triangle shares two moments with its nearest neighbours, therefore dictating the alignment of the third moment upon a triangle. The degeneracy therefore does not scale with size and the ground state remains only doubly degenerate.

2.4.4 *Kagomé* Lattice

Tessellating the triangles by their edges ensures that the orientation of only one moment of a triangle is determined by its neighbouring triangle. This connectivity is too poor for the spin orientation of a triangle to be coherently propagated to its neighbours. This is exemplified in Figure 2.7: one central chiral form does not dictate the spin configuration of an adjacent triangular plaquette. The degeneracy of such a lattice scales with its size, and the system is said to be macroscopically degenerate.

Small perturbations arising from either thermal or quantum fluctuations [83], further neighbour interactions or anisotropy, *e.g.* easy plane [36,84], easy axis [80,82,85]

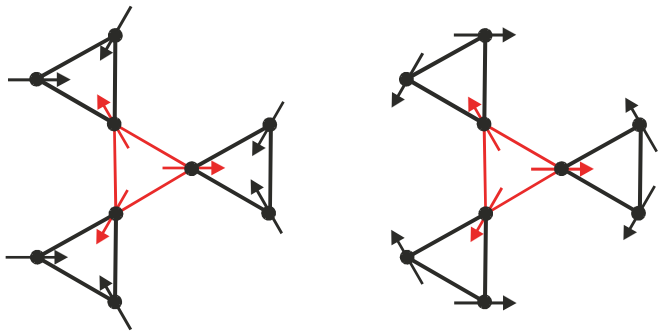

Figure 2.7: These two diagrams show a red triangle with the same chirality at the centre of a vertex sharing lattice of triangles, with moments placed at the vertex of each triangle. Maintaining the 120° alignment of spins, required for the spin structure to be a ground state, is an insufficient rule for the spins of the neighbouring triangles to be uniquely defined: each of the triangles is able to adopt either of the two chiral states. This degeneracy scales with the size of the system ultimately producing a macroscopically degenerate ground state.

and the Dzyaloshinsky-Moriya Interaction (DMI) [86], can have a strong influence over the ground-state manifold. Such perturbations can reduce the degeneracy of the ground state or select a particular spin configuration and so lead to magnetic order. These possibilities will be discussed further in later sections.

2.5 Spin folds and spin origami

As well as resulting in a macroscopically degenerate ground state, the vertex connectivity of the *kagomé* lattice has another particular feature: the ground states are said to be *connected*. This means that the system is able to evolve from one ground state to any other ground state through a sequence of steps that involve only other ground states. In practice, this involves the collective reorientation of spins of two of the sublattices about the axis defined by the third sublattice. In the absence of any energy barriers these spin reorientations, termed spin folds (Figure 2.8), will cause the Heisenberg *kagomé* antiferromagnet to remain fluctuating in a liquid-like state even at $T = 0\,\mathrm{K}$ [87] as there is no energy barrier for the folds [84]. The softness of the system is very robust to disorder as significant densities or clusters of disorder are needed to allow interactions between defects to build, and lead to the formation of an infinite cluster and eventually conventional spin-glass behaviour [69, 88]. The presence of anisotropy can, however, be very significant as it is able to cause the spins to lock and to induce a phase transition at finite temperature.

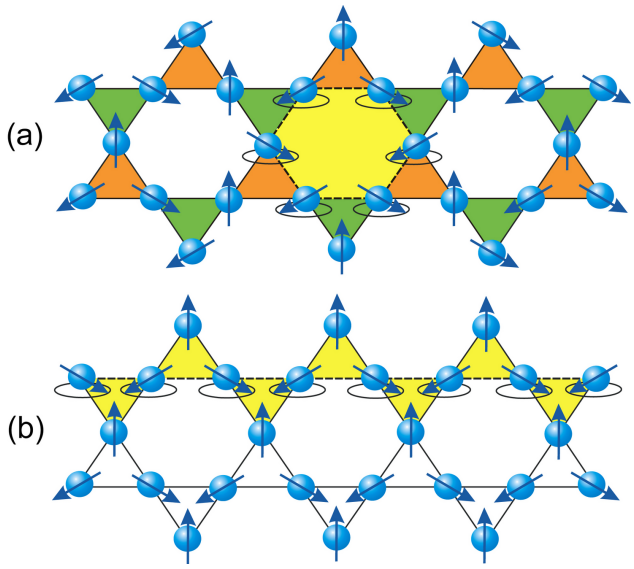

Figure 2.8: The different chiralities and spin folds possible for the *kagomé* antiferromagnet. The orange and green triangles have the $\kappa = +1$ and the $\kappa = -1$ chiralities respectively. Zero energy excitations termed 'spin folds' (highlighted in yellow) can occur within structures with both uniform and staggered chiralities: a) shows an 'open spin fold', which traverses a lattice if based upon the uniform chirality (the $\mathbf{q} = 0$ structure); b) shows a 'closed spin fold' based upon a lattice with staggered chirality (the $\sqrt{3} \times \sqrt{3}$ structure). The circles show the particular spin fold through the two coplanar structures also known as weather vane modes.

In order to study the ground state for a coplanar manifold, the spins on a *kagomé* network can be mapped onto a sheet of edge-sharing "spin triangles" [88]. Here the direction and magnitude of an individual spin determine the length of each side of the triangle. For a uniform *kagomé* network the "spin triangles" are equilateral and will allow folding of the ground-state manifold, which depends on the chirality of the ground-state. In a $\mathbf{q} = 0$ structure, where there is uniform chirality, the ground-state manifold corresponds to a flat sheet. A $\sqrt{3} \times \sqrt{3}$ structure, where the chirality alternates from one sublattice to the next, the ground-state can be folded into a single "spin triangle" [88]. Mapping this back onto a real *kagomé* network means any spin fold which preserves the 120° spin orientation within the $q = 0$, traverses the entire lattice and is known as an "open" spin fold as shown in Figure 2.8 (a). A spin fold within the $\sqrt{3} \times \sqrt{3}$ structure which preserves the 120° spin orientation is known as a "closed" spin fold which form localised loops shown in Figure 2.8 (b). Spin folds which retain the 120° spin orientation are known as π folds ($\alpha = \pi$).

Mapping the spins from a *kagomé* lattice onto "spin triangles" can also help

explain what happens if defects are introduced into the system from thermal fluctuations or site disorder by increasing or decreasing the lengths of the sides of the "spin triangle" or zero length in the case of a vacancy. This will result in a buckling of the flat sheet, and for a vacancy defect there will be non-coplanarity within a localised area of ten spins, shown from Monte Carlo simulations [88].

2.5.1 Order-by-disorder, and thermally induced defects

Spin folds are a non-site disordered defect: they break the continuous rotational symmetry of the system and correspondingly provide a stiffness to the magnetic system. For the *kagomé* lattice, these spin folds are non-Abelian [89]. This means two spin folds (defects) cannot cancel each other out or pass through each other unchanged. Instead, they entangle and bind with each other [84]. This non-Abelian character allows the system to trace paths between defects. Spin-folds that intersect at an angle $\alpha = \pi$ through a coplanar configuration create 180° point defects. When spin-folds of ($\alpha \neq \pi$) intersect one another there is a mutual stiffening. Increasing spin stiffness, γ, reduces the softness of the system. However, for a uniform *kagomé* system, where the only defects are created by thermal fluctuations, low energy spin-wave interactions will reduce γ to zero at long length scales, which allows a small density of defects to remain at low temperature.

At high temperatures defects are formed, but eventually on cooling entropy selects the coplanar manifold through order-by-disorder [81]. This crossover from high temperature with many defects to a very small density of defects at low temperature can cause a topological transition, termed a Kosterlitz-Thouless (KT) transition [68]. The formation of vortices of spins within the plane becomes thermodynamically favourable as the temperature increases and spin-stiffness, γ, is reduced. Here, even a small anisotropy contribution plays a significant role as it reduces the softening of the spin stiffness and allows a crossover from a high density of defects to a low number at a critical transition [84].

Entropy considerations show that even a *kagomé* antiferromagnet without spin anisotropy, *i.e.* the pure Heisenberg Hamiltonian, displays an effective anisotropy with coplanar states with nematic correlations being favoured by an effect called 'order-by-disorder' [69,90]. This arises from the higher number of zero energy modes that are accessible to a coplanar configuration, and is an entropic selection [81,91]. As $T \rightarrow 0\,\mathrm{K}$ [81], entropy favours spin states with the propagation vector $\mathbf{q} = \sqrt{3} \times \sqrt{3}$ because the spin folds based on this ordering vector have the form of

closed loops, and are greater in number than would be supported by spin structures with the ordering vector $\mathbf{q} = 0$, that traverse across the entire system [81].

2.6 Effects of anisotropy on the classical *kagomé* antiferromagnet

In the following section the effects of different types of anisotropy, Ising, XY and DMI, on the degenerate *kagomé* antiferromagnet will be considered. The observations of glassy magnetic behaviour in the Ising and XY models is remarkable as they provide theoretical backing to the proposal that the spin-glass state in hydronium jarosite is a result of finite spin anisotropy, and is not caused by the presence of disorder. Further, the non-Abelian nature of interactions and entanglements of spin folds on the *kagomé* antiferromagnet suggests that any spin-glass state based on them will have a 'memory' of past spin configurations.

2.6.1 Easy-axis (Ising) anisotropy

Monte Carlo simulations have shown that Ising (easy-axis) anisotropy can give rise to spin-glass behaviour and weak z-axis ferromagnetism [82, 85], where the anisotropy restricts the spins to lie along the z axis. The Hamiltonian (2.17), modeled by Bekhechi *et al.* [82], is based on antiferromagnetic exchange interactions between nearest neighbours and each spin is located on every site i on the *kagomé* lattice with unit magnitude.

$$\mathscr{H} = J \sum_{i<j} (S_i^x S_j^x + S_i^y S_j^y + A S_i^z S_j^z). \tag{2.17}$$

The A parameter describes the strength of the exchange anisotropy: $A > 1$ represents an easy-axis anisotropy. The limit $A \to 1$ describes the Heisenberg model whereas $A \to \infty$ is an infinite-spin Ising model.

The degeneracy with respect to rotation of the spins through the plane and $\mathbf{q} = 0$ sublattice occurs at $T = 0$ [80] for the *kagomé* system. This also occurs when $A > 1$, though at finite temperature the degeneracy is lifted by order-by-disorder effects which results in a canted 120° configuration. This gives rise to a net non-zero magnetisation along the z axis. Within the Heisenberg limit, $A \to 1$, the spin folds of the degenerate manifold can rotate about the x, y, z axes, but for $A > 1$, excitations

select the z axis leaving no spatial order in the xy plane. Eventually, defects break-up the chirality of the spins and the preference for z axis symmetry leads to a critical transition, T_{C}, similar to a two dimensional $S = \frac{1}{2}$ Ising ferromagnetic model. The value of $A \sim 2$ corresponds to a maximum in T_{C}. However, in the limit $A \to \infty$, T_{C} tends to zero and the system essentially becomes a $S = \frac{1}{2}$ Ising antiferromagnet, though the nature of the ground state appears to be complex. Measurements of the relaxation time, τ, increase sharply as the temperature is reduced:

$$\tau \sim (T - T_g)^{-\varphi} \tag{2.18}$$

where φ is the relaxation time exponent and its maximum is at $A \geq 1$. As the anisotropy increases, $A \geq 2$, T_{g} approaches T_{C} as a result of the canted moments in the triangle decoupling with the magnetisation and entering a glassy transition. When $A = 2$, the temperature at which the relaxation time diverges from high temperature equilibrium dynamics, T^*, is found to be significantly higher than the values of T_{C} and T_{g} for all other values of A. This has been related to a broad maximum in the specific heat attributed to the local degrees of freedom of the weather vane defect [85]. This gives rise to the possibility of another transition occurring, a critical transition, T_{C}, at a temperature slightly higher than T_{g}.

2.6.2 Easy-plane (XY) anisotropy

Easy-plane or XY anisotropy describes the situation where the magnetisation lies within a local plane. In the *kagomé* antiferromagnet it causes the spins folds to be stiffened along the z axis. A small amount of easy-plane anisotropy will be enough to cause a true topological phase transition, a remarkable result [84]. When cooling from high temperature in the pure Heisenberg limit, (where the anisotropy, $\epsilon = 0$), there is a sharp crossover from a high thermal-defect regime to an infinitesimal number at which a critical transition occurs at $T \to 0\,\mathrm{K}$. The transition temperature scales only weakly with anisotropy: $T \sim 1/\ln(1/\epsilon)$. However, when $\epsilon \neq 0$ there are two prominent length scales which can determine the nature of the crossover and whether it becomes a phase transition. The spin-correlation length, ξ, increases with increasing spin stiffness, γ, and the second, a new length scale l_0, which is an effective measure of the system deviating from coplanarity. Larger values of l_0 reflect a softening of the spin modes as $\epsilon \to 0$. At higher temperatures, where $\xi < l_0$, the defects are essentially free and unbounded and there exists no discernible

true transition. However, on cooling, $\xi > l_0$ and the 180° point defects bind and generate 120° point defects and the system enters into a Kosterlitz-Thoules (KT) transition [68]. Further cooling results in the all the defects binding as $\xi \to \infty$.

The presence of strong XY anisotropy creates many 120° point defects which lead to a decreases in the KT transition temperature, $T_{\mathrm{KT}} = JS^2\pi/36 \approx T_{\mathrm{W}}/48$ [84]. This occurs because vortices generated from 120° point defects adhere to one another with only a third of the full potential of 360° vortices. This particular KT transition turns out to be a true critical second order transition because there is a divergence in the specific heat and, more importantly, because the specific heat is proportional to T^2 rather than just T [84, 92].

The dependence of the specific heat on T^2, rather than the linear dependence characteristic of canonical random-site or bond spin glasses, is one of the most prominent features that distinguishes the anisotropic *kagomé* spin glasses. This has been calculated by theory [84, 93, 94] and observed experimentally [36, 95, 96]. The T^2 dependence is of the type observed in ordered 2-dimensional antiferromagnets and suggests that the *kagomé* spin glass contains the Goldstone modes characteristic of long-range magnetic order. This appears contradictory as the *kagomé* spin glass is necessarily based on disordered spin configurations. However, the *kagomé* spin glass is not entirely disordered as it is based on spin configurations that feature neighbouring moments at 120°, with the energy of each triangular plaquette being identical. The *kagomé* spin glass can therefore be considered as having a unique type of hidden order - a translationally ordered energy space that is able to support Goldstone modes. A definite test for this theory will be an enhancement of T_{g} with applied field [84].

2.6.3 Dzyaloshinsky-Moriya interaction induced anisotropy

The final anisotropy that we will consider is the Dzyaloshinsky-Moriya interaction, which was first considered on the *kagomé* lattice by Elhajal *et al.* [86]. The Hamiltonian used in these calculations is for two neighbouring magnetic ions of $S = \frac{1}{2}$ without spin anisotropy:

$$\mathscr{H}_{ij} = J_{ij}\mathbf{S}_i \cdot \mathbf{S}_j + \mathbf{D}_{ij}(\mathbf{S}_i \times \mathbf{S}_j) \tag{2.19}$$

In their model only isotropic antiferromagnetic exchange was considered ($J_{ij} > 0$)

and $\mathbf{D}_{ij}$ characterises the antisymmetric DMI.

It is useful to consider symmetry when looking into the effect of the DMI. These show that for the DMI to be non-zero, there can be no centre of inversion on the bond mediating the exchange, which holds for the *kagomé* lattice. Also, if the bonds that mediate the DMI are in the *kagomé* plane, then the DMI will be constrained to be perpendicular to the *kagomé* plane, as this is a mirror plane. If the crystal structure does not contain this mirror plane but the three perpendicular planes associated with the *kagomé* lattice are still present, then the $\mathbf{D}_{ij}$ vectors are constrained to be in the plane perpendicular to the bond $i - j$. Another requirement for the DMI to be non-zero is the presence of spin-orbit coupling.

When $\mathbf{D}$ is perpendicular to the *kagomé* plane, *i.e.* it lies along the z axis, even the smallest value for D will result in a phase transition to an ordered spin structure [86]. The sign of D, *i.e.* $D_z > 0$ or $D_z < 0$, dictates the chirality of this ordering. A large negative D results in ground states with $\kappa = -1$, while a large positive D produces those with $\kappa = +1$ chirality. The system undergoes a phase transition to a $\mathbf{q} = 0$ long range ordered state at low temperatures with the DMI acting as an easy-plane anisotropy.

In the *kagomé* antiferromagnet, the DMI has a first order effect on the degenerate ground-state at low temperatures. This is because the DMI does not contain a complete set of zero mode excitations and therefore selects a particular set of magnetic states. Elhajal *et al.* [86] showed that the critical temperature is almost linear in D and that the magnitude of J has little effect, unless both $|J|$ and $|D|$ are small and a disordered phase results.

When $\mathbf{D}_{ij}$ is in the plane perpendicular to bond $i - j$, the competition with J and D causes a canting of the moments out of the plane and acts as an easy-axis anisotropy producing a weak ferromagnetic component along the z axis. The strength of this ferromagnetic component, and the degree of canting away from the *kagomé* plane depends upon the amount of the in-plane component of $\mathbf{D}$.

The dependence of the ground-state spin structures on $\mathbf{D}$ are summarised in Figure 2.9. There is further competition between the out-of-plane component D_z and the in-plane component D_p depending on the sign of D_z. If $D_z > 0$, the chirality selected is the same as that from D_p, which is $\kappa = +1$ in Figure 2.9. However, if $D_z < 0$ then the chirality $\kappa = -1$ is preferred. Calculations of the energies for the two chiralities $\kappa = \pm 1$ indicate that the sign of D_z selects the chirality, whereas D_p always favours $\kappa = +1$ with weak ferromagnetism in the z axis. Therefore, for

$D_z > 0$ a canted configuration based upon chirality $\kappa = +1$ is selected with weak ferromagnetism in the z axis. If $D_z < 0$, then there is also a weak ferromagnetic component along the z axis with a canted structure based on chirality $\kappa = +1$ but along the direction of $-z$. As the strength of $-D_z$ increases, so the conformation becomes more canted until a critical point, which is dependent upon the strength of J, which favours coplanar configurations, is reached and the resultant configuration is coplanar ($\kappa = -1$). If there is no D_p component, then the conformation is coplanar based upon chirality $\kappa = +1$. Under these circumstances and with a negative D_z, the size of D_p is irrelevant as the spins are lying in the plane.

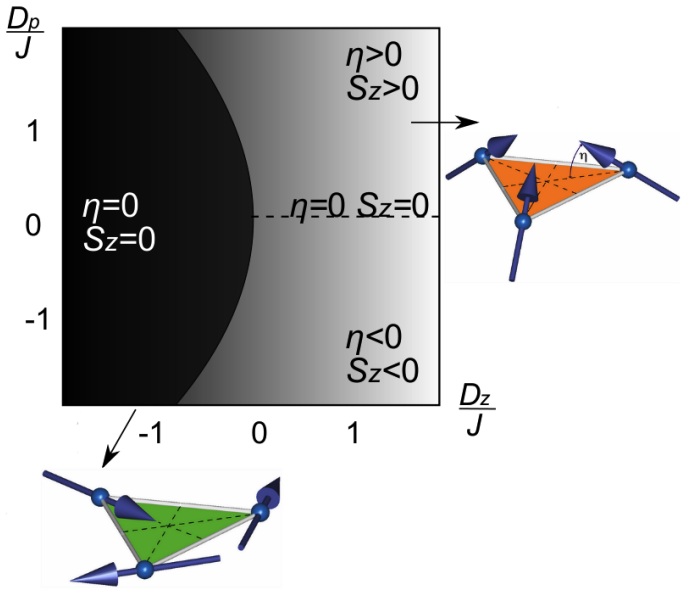

Figure 2.9: Different ground states obtained for the *kagomé* antiferromagnet as a function of J, D_p and D_z. η is the angle that describes the canting of the spins out of the *kagomé* plane and S_z is the direction of the magnetic component out of the plane [86].

This competition also effects the critical temperature: when $D_z > 0$ and $D_p \neq 0$ they drive the system to chirality $\kappa = +1$ and achieve a higher critical temperature. When $D_z < 0$ and $D_p \neq 0$ the other chirality is most likely to be selected with a lower critical temperature.

2.7 Experimental systems

Historically, much interest in frustrated *kagomé* antiferromagnets arose from experimental studies of $SrCr_{8-x}Ga_{4+x}O_{19}$ (SCGO), and the observation properties that could not be understood within the accepted models of the spin glass state. This

fuelled a wide range of theoretical and experimental work into the possible ground states of the *kagomé* antiferromagnet. Experimental studies of later model systems, such as the jarosites and the recently discovered Herbertsmithite ($ZnCu_3(OH)_6Cl_2$), have continued this trend, further challenging theory to include effects such as the DMI, within models in both the classical and quantum limits.

2.7.1 $SrCr_{8-x}Ga_{4+x}O_{19}$ (SCGO)

The frustrated magnetic moments in $SrCr_{8-x}Ga_{4+x}O_{19}$ (SCGO) are borne by Cr^{3+} ($S = \frac{3}{2}$) ions that make up a pyrochlore slab formed by two *kagomé* layers interleaved by a triangular layer [95–98].

Magnetisation and neutron powder diffraction measurements showed SCGO to display a very high empirical frustration index of $|\theta_W|/T_C \sim 150$ ($\theta_W = -515\,K$, $T_C = 3.5\,K$) [96], and not to order into a Néel state upon cooling. Instead, a spin glass-like transition was observed at low temperature that was shown to involve short ranged magnetic order based on the $\sqrt{3} \times \sqrt{3}$ ordering vector [96].

Unfortunately it has been shown that Ga^{3+} / Cr^{3+} substitution and non-stoichiometry appear to play important roles in the underlying magnetic properties, with the value of the spin-glass transition temperature, T_g, ranging between 3.5 and 7 K depending on the degree of Ga^{3+} over-incorporation, x [96]. The spin glass state was, however, shown to be unconventional, as it displays a T^2 heat capacity, SCGO cannot, therefore, be considered as a canonical spin-glass system that is the result of disorder and frustration [95, 96]. Though it is difficult to untangle the properties of the *kagomé* lattice from those that arise from disorder, a recent reappraisal of SCGO by NMR suggests the spin glass properties may be intrinsic to the *kagomé* lattice as some aspects of the microscopic susceptibility are robust to disorder [99].

2.7.2 Herbertsmithite

Recently there has been a flurry of activity regarding a new $S = \frac{1}{2}$ *kagomé* antiferromagnet called Herbertsmithite[1], originally hailed as a 'perfect *kagomé* antiferromagnet' [100–105]. This mineral is the end member of the paratacamite mineralogical species which has the general formula $Zn_xCu_{4-x}(OH)_6Cl_2$ [106] where for Herbertsmithite $x = 1$.

[1]The mineral was named after Herbert Smith in honour of his discovery of paratacamite.

Herbertsmithite is defined as a distinct species because the Zn^{2+} ions reside in the interstitial sites between the *kagomé* layers made up of highly Jahn-Teller distorted Cu^{2+} ions. It therefore appeared to be an ideal candidate for a $S = \frac{1}{2}$ *kagomé* Heisenberg antiferromagnet. The crystal structure highlighting the Cu^{2+} ions is shown in Figure 2.10.

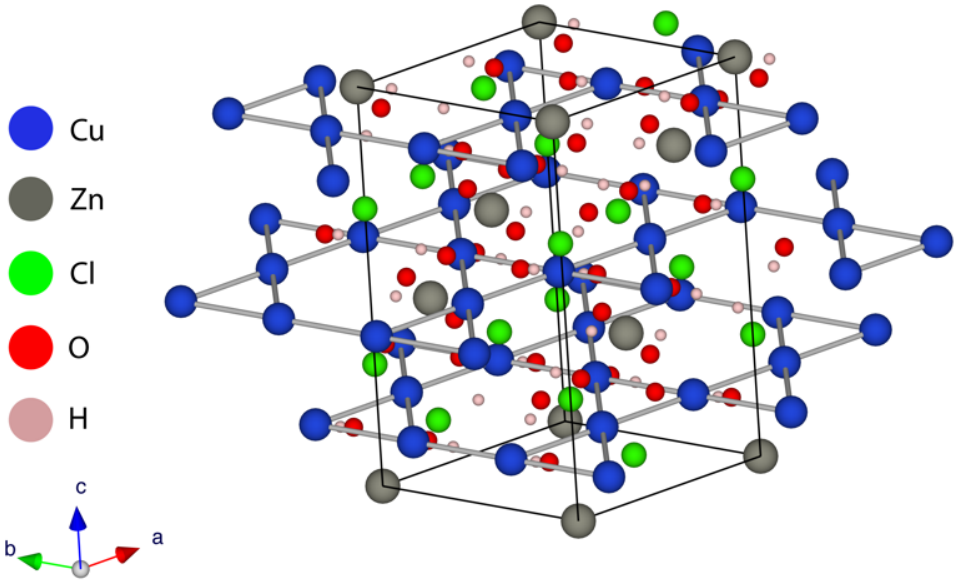

Figure 2.10: In Herbertsmithite the arrangement of the Cu^{2+} ions form the *kagomé* network. The ordering of the zinc and copper ions makes Herbertsmithite a very compelling candidate for a $S = \frac{1}{2}$ *kagomé* antiferromagnet.

Despite a large Weiss temperature $\theta_W = -300\,K$ Herbertsmithite displays neither a magnetic transition nor spin-glass ordering down to the lowest temperatures studied, 50 mK [100, 105, 107]. It does, however, display a specific heat that is approximately proportional to T^3 above $\sim 5\,K$, that drops to a $C \sim T^{\frac{1}{2}}$ dependence below 5 K [100]. The material also appears not to have a spin gap [103, 107] down to 50 mK [100] suggesting the absence of any triplet-singlet gap in its low temperature quantum-spin liquid state.

All the work on Herbertsmithite to try and understand the magnetism has focused on the DMI as the principal source of anisotropy [100, 104, 108, 109]. EPR has shown that that the strength of the DMI is indeed significant ($|D|/|J| \sim 8\,\%$) and could affect the magnetism at low temperatures [101, 104]. In this vein, there have been suggestions that the presence of the DMI in such a system with large Jahn-Teller distortions or a high degree of stoichiometric imperfections may produce glassy dynamics that increase with the non-stoichiometry [103].

2.7.3 Jarosites

The most studied *kagomé* antiferromagnets are the jarosites, which have the idealised formula $AFe_3(SO_4)_2(OH)_6$, (A = H_3O^+, NH_4^+, K^+, Na^+, Rb^+, Ag^+, $\frac{1}{2}Pb^{2+}$ or Tl^+) in which Fe^{3+} ($S = \frac{3}{2}$) makes up the *kagomé* network [18]. Most of the jarosites display magnetic long-range antiferromagnetic order at low temperatures and have a frustration index of ~ 30 ($|\theta_W| = 1500\,K$, $T_N = 45 - 55\,K$) [18, 37], though the magnetic ordering appears to be sequential with one strong magnetic transition, T_{N_1}, at $\sim 60\,K$ occurring before a weaker transition at $T_{N_2} < 55\,K$ [37]. These transitions involve initial order to an umbrella structure (with the propagation vector $\mathbf{q} = 00\frac{3}{2}$), that flops into the *kagomé* plane upon cooling through T_{N_2} [22, 58, 110].

The exception to this behaviour is hydronium jarosite, which undergoes a transition to a spin-glass state at $T_g \sim 13\,K$ [21]. This spin glass appears unconventional and has been put forward as an example of a 'topological spin glass' as its responses correspond to those predicted for the easy-plane *kagomé* antiferromagnet (Section 2.6.2): the specific heat has a quadratic dependence [37] and the out-of-equilibrium dynamics display the temperature independent memory effects expected for a spin glass based on non-Abelian interactions between spin folds [36].

The nature of disorder and non-stoichiometry in the jarosite crystal structure, and answers as to why the only known jarosite not to undergo any long-range order is hydronium jarosite are key to understanding what properties of the jarosites are intrinsic to the frustrated *kagomé* lattice. It is the goal of this thesis to find the key through studies of the chemistry, magnetism and crystallography of jarosites, and of the hydronium jarosite in particular.

Chapter 3

Experimental Methods

This chapter describes the techniques used to investigate the synthesised samples and includes: elemental analysis, morphology studies, magnetic characterisation and crystallography. More detailed synthetic conditions and results are discussed in Chapter 4.

3.1 Hydrothermal synthesis of Fe jarosites

The synthesis of the Fe-jarosites were carried out using Pyrex pressure tubes (Figure 3.1) rather than the more conventional PTFE-lines steel bombs. These were manufactured by Ace Glass Inc., and used a PTFE screw top (Ace Glass # 15) with a front mounted O-ring. Front mounted O-rings maintained the internal pressure at higher temperatures for longer periods of time. Two capacities of tubes were used: 23 cm^3 or 38 cm^3 filled with 15 cm^3 or 25 cm^3 of solution, respectively, filling the capacity of both by ∼66%. There was a limit of the maximum working temperature: approximately 170 °C, or up to 180 °C for shorter periods, compared with approximately 220 °C for the PTFE/steel bombs. Despite the limited temperature range of the pressure tubes there were clear advantages to use Pyrex pressure tubes instead. The tubes allowed for a better temperature gradient through the reaction vessel, the cleaner surface aided jarosite crystal growth, and the ability to observe the progress of a reaction. Overall, Pyrex pressure tubes allowed for a rapid turnaround and mass production of jarosite samples.

Reactions were carried out at temperatures ranging from 120-150 °C for 21 hours. There was no stirring or suction filtration as this damaged the jarosite crystals due to their softness. The jarosite precipitates from these reactions were washed several

times with distilled water, the water was decanted off each time, and the precipitates were dried in an oven between 110-120 °C for a minimum of 4 hours. Yields ranged from 0.2 g to 0.8 g.

Figure 3.1: Ace Glass Pyrex pressure tubes with front mounted O-rings. The major benefit of these vessels is to be able to look inside and they provide a far better temperature gradient for synthesis [111].

3.2 Inductively coupled plasma (ICP) elemental analysis

Inductively Coupled Plasma (ICP) for elemental analysis provides a very accurate and precise means for determining elemental analysis for samples that require simultaneous analysis and trace elemental analysis. The ICP produces a plasma containing ionised species from the sample to be analyzed, and elemental analysis is determined either from analysis of the emission spectra of the ionized species or by mass-spectrometry. The technique used in this project is ICP-Atomic Emission Spectra (ICP-AES) also known as ICP-Optical Emission Spectra (ICP-OES); these terms can be used interchangeably throughout ICP discussions. A detailed discussion of ICP, in particular ICP-AES, is given in Appendix A.

ICP-AES data were collected with two different machines. One of them was a commercial service using the Varian Vista-Pro ICP-AES with a simultaneous solid-state detector at the Natural History Museum, London. The results were returned as percentage weight and, as a service, the sample preparation and data collection were undertaken by the machine operator. The solutions were dissolved in HCl following the method set out by A.M. Smith [14]. The ICP-AES ran with a high

argon flow (low oxygen) and the optics were fully functional.

The second machine used was a Perkin-Elmer ICP-AES 3300RL with a segmented-array charge-coupled-device detector at Royal Holloway University. As there was uncertainty in the sulphur being adequately detected in the first batch of samples, a second batch was run.

The results from these experiment were returned in units of parts per million (ppm) and were converted to percentage weight. This requires normalisation to an element. As oxygen was not recorded because of the air content, the assumption was made that there are two sulphate groups per formula unit. Detailed explanation of how the results were obtained is given in Chapter 6.

3.3 Scanning Electron Microscope

Scanning Electron Microscopy (SEM) is a very good tool for visualisation of samples at the meso, micro (μm) and nano (nm) length scales, showing clearly the morphology, size and surface details of crystals and crystallites. SEM also provides a visual confirmation of any impurities and allows the observation of amorphous content or impurity phases, or simply how crystallite morphology changes over a solid solution series.

SEM uses a highly focused beam of electrons for the visualisation of microscopic objects in real space by projecting the beam onto the surface of the sample. Scanning microscopes utilise the resultant electron interaction with the surface to obtain a variety of data. Electrons that are backscattered by the direct interaction between an incident electron and the electronic shells of atoms on the sample surface produce the visual information about the morphology. The degree of backscattering varies with atomic number: the heavier the atom, the brighter the backscattering.

Secondary electrons provide information about the topology of the surface. As an incident electron travels into an atom, it will energise one or more electrons in the K shell. The resultant kinetic energy of the excited electron is small (5 keV) and provides detailed information of the sample topology because of contrast due to the angle of incidence of the electron beam upon a surface. Electrons scattered or emitted from a perpendicular surface will give a uniform but less brilliant signal as some secondary electrons will penetrate into the sample, whereas edges and high angle of incidence will result in more secondary electrons being counted.

Auger electrons and X-rays generated by the excitation of the K shell electrons

can be used to determine elemental analysis as they are characteristic of individual elements. Their use corresponds to a variant of SEM called Energy Dispersive X-ray Spectroscopy (EDX SEM). This efficient and effective method for elemental analysis requires minimal sample preparation. Detailed discussion on both morphology and elemental analysis using scanning electron microscopy can be found in the book *Modern Analytical Geochemistry* [112].

3.3.1 SEM morphology studies

Morphology studies were carried out using a JEOL JSM-6301F operating with a 15 kV electron beam and a probe distance of 16 mm. As jarosites are insulating, they were coated in gold to prevent charge from building up on the surface of the samples. The samples were not polished because of the brittleness of jarosites. They were instead sprinkled onto an aluminium stub with a very tacky black surface. The stub is then placed into a gold sputterer to coat the surface. The JEOL JSM-6301F can achieve very high magnifications - up to 270,000× magnification, but requires a high vacuum to obtain this. Therefore, it is important that the samples are dry before placing them into the vacuum chamber. Furthermore, only 1-3 samples at a time can be studied.

3.3.2 EDX SEM elemental analysis

Elemental analysis was carried out using a Philips Environmental SEM with EDX analysis. Environmental SEMs run at a lower vacuum and are not suitable for morphology studies but are very successful for elemental studies. Attached to the instrument there is an Oxford Instruments INCA energy dispersive X-ray spectroscopy which analyses the energy of the associated electrons emitted from the sample surface which is dependent upon the atomic number of the atoms.

3.4 Superconducting Quantum Interference Device Magnetometery - SQUID

The SQUID magnetometer is the most sensitive instrument available to measure the magnetisation of a sample. It measures, as an interferometer, changes in magnetic flux as slight as $2.07 \times 10^{15}\,\mathrm{T\,m^2}$, which is one unit of quantised magnetic flux.

The SQUID uses a superconducting loop with Josephson Junctions (a very thin insulating layer, which still allows a super-current to tunnel through without loss of phase coherence) (Figure 3.2). One Josephson junction (X) is coupled to the magnetic environment of the sample by two pick-up coils wound in opposing directions; the current is able to pass freely through the second junction (Y). A constant persistent current is passed throughout the ring and any magnetic field passing through the pickup coils will lead to a phase difference in the currents passing through the two junctions, creating oscillations in the super-current. Counting these oscillations relates to the number of quanta of flux the SQUID is exposed to.

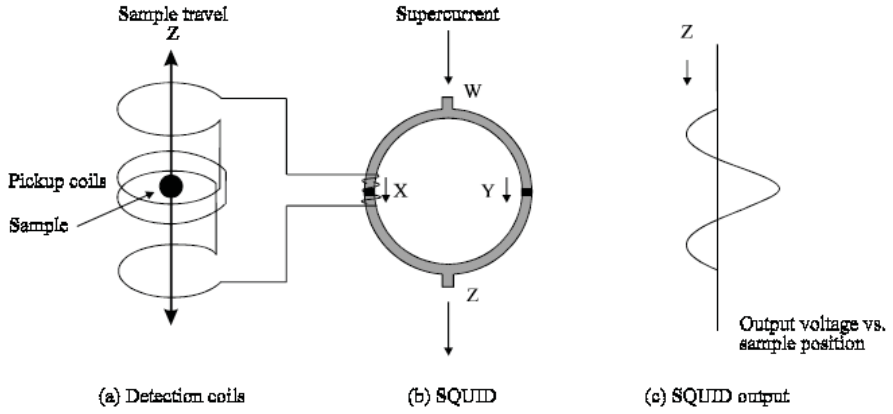

Figure 3.2: Schematic diagram of a DC SQUID. a) shows the pickup coils where the magnetic flux from the sample is detected, either in the absence or with an applied field. b) shows the loop with the two Josephson junctions at points X and Y. The current is recombined at Z and the output from Z is shown in c). The oscillating voltage relates to the magnetic flux applied at X, obtained from the interference of the two superconducting phases passing through X and Y [61].

All the magnetic measurements were made using a Quantum Design MPMS-7 DC SQUID. This machine is capable of measuring the magnetisation of samples from temperatures of 1.8 K up to 310 K. The maximum applied magnetic field is 7 T and applied fields as small as a tenth of a Gauss can accurately be applied. Two MPMS-7 DC SQUIDs instruments were used and both had slightly different capabilities. The RI SQUID at the Royal Institution of Great Britain is capable of taking continuous measurements below 4.17 K and has a sweep facility to enable measurements to be taken without having to wait for temperature stability, which is useful for quick characterisation. However, the RI SQUID has a poor temperature stability which meant that 4 measurements per data point were required to reduce

errors. The CMMP SQUID in Condensed Matter and Materials Physics, UCL does not have the temperature sweep and continuous low temperature capabilities of the RI SQUID, but has a better temperature stability so only 2 measurements per data point were needed, it also contains a magnet reset facility.

All jarosite samples were ground and approximately 50 mg of each sample was placed inside a gelatin capsule, ensuring no contamination to the capsule or the sample with any impurities, which may provide a ferromagnetic response. The gelatin capsule was then inserted ~ 5 cm into a Quantum Design straw. Two small T-shaped incisions across the straw were made above and below the gelatine capsule, and the flaps created pushed into the straw to help ensure the gelatin capsule did not move too much inside the straw. In some cases the capsule was wrapped in Kapton tape to provide a tighter fit inside the straw. Several small incisions were made near the top of the straw which was pushed about 1 cm onto the end of a long thin brass/stainless steel rod. Kapton tape is used to cover the end of the straw nearest to the sample to prevent the sample from falling out during the experiment. This rod with a sample mounted straw at the end is gently pushed all the way inside the Quantum Design SQUID.

The sample is then centred between the two pick up coils and either any remnant magnetisation is removed or an opposing field is applied to produce an effective zero applied field. The scan length was always set to 4 cm, and depending on the instrument, 2 or 4 measurements were averaged per data point. Positioning the sample and determining zero field were always performed at a relatively high temperatures (100 K), far removed from any magnetic transitions for the jarosite samples.

The susceptibility, χ_{mol}, was calculated from the observed magnetisation after correction for the diamagnetic contribution from the straw, gelatin capsule and the sample itself according to:

$$\chi_{\mathrm{mol}} = \frac{A_r emu}{(B\mathrm{S}) - \mathrm{D}_{\mathrm{mol}}} \tag{3.1}$$

where A_{r} is the molar mass (g), emu is the magnetisation (cgs units), B is the magnitude of the applied field in Gauss, S is sample mass (g) and D_{mol} is the molar diamagnetic contribution from the constituent ions [64].

The effective moment, μ_{eff} is calculated from χ_{mol}:

$$\mu_{\text{eff}} = \sqrt{(8\chi_{\text{mol}}T)} \tag{3.2}$$

where T is the temperature (K) and the units for μ_{eff} in cgs are ergs/Gauss.

The Weiss temperature, θ_{CW}, is determined from the intercept with the x axis by fitting a straight line fit to χ_{mol}^{-1} in the region where the data linear (paramagnetic region).

3.4.1 Determination of transition temperatures

The spin glass like transition temperature for hydronium jarosites is determined from the temperature at which the separation between the ZFC/FC susceptibility occurs. This was also aided by looking at the first derivative ($d\chi/dT$) of the FC data to highlight the transition. The non-hydronium jarosites display a very prominent first transition, T_{N_1} which is easily obtained from the maxima in the susceptibility. The weaker second transition, at lower temperature, can be harder to identify and sometimes required looking at the first derivative of the FC data for a noticeable change in gradient.

3.4.2 Field sweep measurements

Field sweep measurements were used to determine the presence of hysteresis. Three different types of hysteresis measurement used are discussed below. Further details of the hysteresis methods used are discussed in Chapter 5.

Standard hysteresis measurements involve sweeping from zero to positive and negative field, before returning to the maximum positive field. Data are taken at a fixed temperature with fields up to $\pm 7\,\text{T}$. An example is given in Figure 3.3 where the red and blue curves show an example of hysteresis in high fields.

Displacement hysteresis measurements comprise of two standard hysteresis measurements. Initially, a standard hysteresis measurement is undertaken. This is repeated again after the sample is warmed and field cooled in a small field. Expected results are shown in Figure 3.3 and feature displacement along the magnetisation (y) axis between the two sets of hysteresis measurements. Displacements along

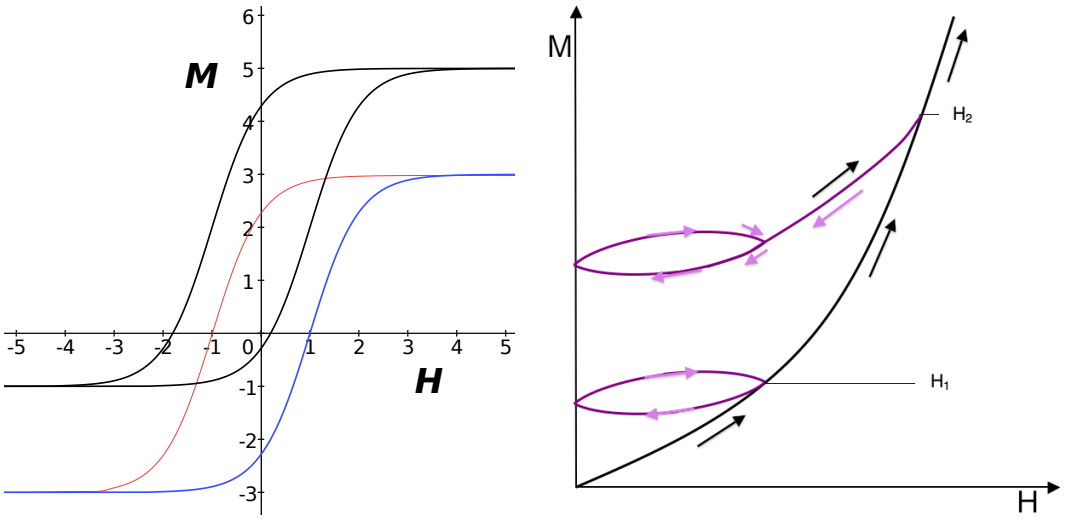

(a) An expected hysteresis loop by applying large positive and negative fields

(b) Hysteresis loops in a small positive field

Figure 3.3: a) Shown are two hysteresis loops generated in high fields. The red curve is the initial magnetisation curve returning from high positive field, the blue curve is the return from maximum negative field sweeping back to maximum positive field. The hysteresis loop in black is an exaggerated expectation when the sample is field cooled in high field before undergoing an hysteresis measurement. b) Loops generated from a virgin curve can be seen by following the arrows. The expectation are for the sub-loops to be incongruent if spin-spin correlations are present.

the y axis suggest uniaxial anisotropy and displacements along the x axis suggest unidirectional anisotropy, *e.g.* DMI.

Hysteresis sub loops in small positive fields are created from a virgin curve are used to investigate the build up of spin-spin correlations (Figure 5.8). The applied field is gradually increased to field, H_1, before being reduced back to zero. The field is then increased back to a value above H_1, H_2, before reduced back to zero. The field is increased again to H_1, then back to zero. The loop is completed by increasing to H_2 again. These processes are repeated again using increasing fields.

It is expected that far above a spin glass transition temperature the sub-loops generated should be congruent. Below the transition temperature the sub-loops should no longer overlay due to the build up of spin-spin correlations [113].

3.5 Diffraction

For a comprehensive text on the subject of diffraction and crystallography the reader is referred to the work edited by C. Giacovazzo [114].

Scattering occurs when the wavelength of the incident wave front and the characteristic lengths in the medium through which the wave passes through are similar in size. Bragg diffraction is where this process is elastic and coherent, and occurs from periodic structures. An example of periodic structures are seen within crystals; where a unit cell defines the necessary arrangement of atoms which can be repeated to generate the crystal structure. The unit cell is defined by a set of lattice parameters; the space group, the spatial relationship between the atoms and their subsequent multiplicity; and the thermal vibration of the atoms. The relationship between the separation of crystallographic planes within a unit cell, X-ray wavelength, and the diffraction angle was derived by Lawrence Bragg leading to Bragg's law (3.3):

$$n\lambda = 2\mathrm{d}\sin\theta \tag{3.3}$$

The derivation of the Bragg's law considers consecutive reflective parallel planes, where each plane is partially reflective. A Bragg reflection is only observed when the reflective beams constructively interfere as shown in Figure 3.4.

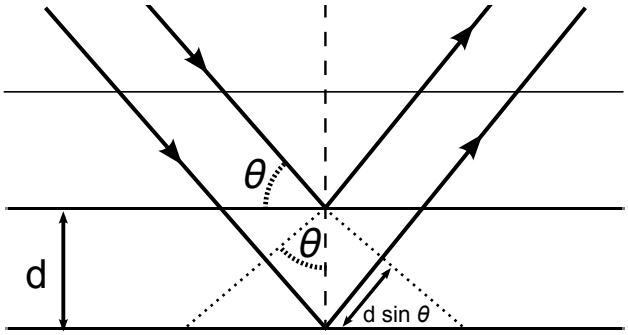

Figure 3.4: In order for constructive interference to occur, the beam traverses an extra distance of 2d $\sin\theta$, that distance must equal an integral number of wavelengths, $n\lambda$: as θ increases so the d spacings become smaller.

The d-spacing between crystallographic planes, labelled as Miller indices, h, k, l, are related by the lattice parameters, a, b, c in equation (3.4) for orthorhombic unit cells.

$$\frac{1}{d_{hkl}^2} = \frac{h^2}{a^2} + \frac{k^2}{b^2} + \frac{l^2}{c^2} \tag{3.4}$$

The relationship between intensity and the structure factor is given in equation (3.5),

$$I_{hkl} = cjPLA|F_{hkl}|^2 \tag{3.5}$$

where c is a factor to consider minor effects, such as the sensitivity of the instrument and j is the multiplicity, denoting the number of equivalent crystallographic planes for a given d-spacing. P is the polarisation factor which depends on the state of polarisation of the radiation and the angle of interaction with the crystallographic planes. L is the Lorentz factor which arises from two contributions in powder diffraction. Firstly, the non-uniformity of crystals or distribution of arrangements of crystallites in a powder sample increases the possibility of achieving a Bragg condition at lower angle: the dependence is $1/\sin\theta$. Secondly, at low angle more counts will be recorded because more of a given Debye-Scherrer cone is measured: the relation is $1/\sin 2\theta$. A is the absorption factor, intensity is reduced due to sample absorption and the path taken of the X-rays or neutrons through a sample and holder. The structure factor F is given in equation (3.6):

$$F = \sum_j f_j N_j \exp[-i2\pi(hx_j + ky_i + lz_j)]\exp(-B_j \sin^2\theta/\lambda) \tag{3.6}$$

where f_j is the atomic form factor for atom j in the cell, which is modified by an isotropic temperature factor $B = 8\pi^2 < \mu^2 >$ to give a temperature dependent atomic factor g_j, where $< \mu^2 >$ is an isotropic average root mean squared thermal displacement given in Å^2. N_j measures the disorder of a crystal, for instance whether a site is fully occupied.

3.5.1 Powder diffraction

Powder diffraction is extremely useful for checking phase purity and amorphous content of samples. The 2θ resolution of powder diffractometers is typically much better than of single crystal instruments, and the ability to collect data from reflections over a much larger d-spacing range allows for greater precision of the lattice parameters. The production of crystals suitable for single crystal diffraction may be extremely challenging and powder diffraction can frequently be the only viable techniques for obtaining a desired crystal structure. A key advantage of the technique is the accessibility of laboratory diffractometers and for this reason it is widely used for quantitative phase analysis and structure refinement.

Both X-rays and neutrons are used for powder diffraction and the related tech-

niques are introduced below.

3.5.2 X-ray Powder Diffraction

The scattering strength of X-rays is proportional to the electron density of the scatterer. For this reason elements and ions with similar electronic configurations are hard to distinguish. X-ray powder diffraction suffers from a fall-off in intensity with increasing scattering angle. This is due to several effects: geometric, the decrease in atomic scattering with increasing 2θ angle, and atomic vibration. The form factor falls-off with increasing $\sin\theta/\lambda$.

3.5.3 Neutron Powder Diffraction

A. K. Cheetham and P. Day [115], and G. L. Squires [116] provide good introductory texts to neutron scattering.

Neutrons are scattered by the nuclei of the atoms, rather than the electrons. Because of this, the strength of the scattering, characterised by a scattering length b, changes in an apparently random manner throughout the periodic table. In some cases, most notably hydrogen (^{1}H) the coherent neutron scattering length is negative, which corresponds to a phase shift between the incident and scattered neutrons. As nuclei scatter as point sources, neutron diffraction does not suffer from a form factor related fall-off of intensity with scattering angle as associated with X-rays.

One of the benefits of using neutrons for diffraction experiments is the wide range of wavelengths that are accessible, commonly from 0.2 to 10 Å. Others include the high penetration of neutrons, due their relatively weak interaction with nuclei, and their spin, ($S = \frac{1}{2}$), which allows neutrons to be used for magnetic scattering.

3.6 Rietveld refinement

Rietveld refinement method was developed by Hugo M. Rietveld [117, 118] in the late 1960s when he realised that whole pattern fitting of powder neutron diffraction data using a model crystal structure in combination with instrument parameters can be used to describe peak shape and width. Prior to Rietveld's work, only simple or high symmetry crystal systems could be analysed from powder diffraction as the overlapping of reflections left more complex systems too difficult to study. There

are a large number of texts on the Rietveld method, though the book edited by R. A. Young covers most aspects [119].

The computer program devised by H. M. Rietveld is an iterative method for crystal structure refinement and requires an initial model structure. The Rietveld method carries out a least-squares process until it is minimised between the observed powder diffraction pattern and a calculated structure pattern. The peak overlap problem ensures the structure cannot be refined without first a model structure that is used to calculate $|F_{hkl}|^2$ values and subsequently y_{ci}, calculated by summing over all the Bragg reflections. The peak profile intensity at any point 2θ can be represented as follows:

$$y_{ci} = c \sum_{hkl} LPA|F_{hkl}|^2 G(\Delta\theta_{i\ hkl}) P_K + y_{bi} \tag{3.7}$$

where $G\Delta\theta_{i\ hkl}$ is the profile function, $\Delta\theta_{i\ hkl} = 2\theta_i - 2\theta_{hkl}$, $2\theta_{hkl}$ is the calculated positions of the Bragg peak, P_K is the preferred orientation function and y_{bi} is the background intensity.

3.6.1 Least-Squares and Goodness of Fit

When data are collected, they are recorded as intensity, y_i for each step, i, and the power of the Rietveld process simultaneously seeks to fit all the intensities with a non-linear least-squares method. The quantity is minimised by an iterative method using this equation to give the residual S

$$S = \sum_i W_i (y_i - y_{ci})^2 \tag{3.8}$$

where $W_i = 1/y_i$; y_i and y_{ci} are the observed and calculated intensities for every step, i, respectively.

The power of the Rietveld process comes from fitting the entire pattern, rather than trying to extract the intensity of individual peaks. The quality of the fit of the calculated pattern with the observed data is typically defined using the metrics: R_{wp} (3.9a), R_{exp} (3.9b) and χ^2 (3.10):

$$R_{\text{wp}} = \left[\sum_i W_i (y_i - y_{ci})^2 / \sum_i W_i y_i^2 \right]^{\frac{1}{2}} \tag{3.9a}$$

$$R_{\text{exp}} = \left[(N - P + C) / \sum_i W_i y_i^2 \right]^{\frac{1}{2}} \tag{3.9b}$$

where N is the number of profile points, P is the number of refined parameters and C is the number of constraints. R_{wp} is a direct measure for the convergence of the refinement, but does not necessarily give an indication of the quality of the data which is given by R_{exp}. The ratio of these two R factors (3.9) is χ^2 (3.10),

$$\chi^2 = \sum_i W_i (y_i - y_{ci})^2 / (N - P + C) \tag{3.10}$$

which gives an overall quality of fit. A value less than 1 strongly suggests over-weighting of the background with respect to the profile.

3.6.2 Preferred Orientation

Preferred orientation may be of little significance or can pose a significant refinement problem in Rietveld refinement. It arises when crystallites align themselves with the surface of the sample holder, such effects can be enhanced due to crystal shape morphology. Its influences are typically small for neutron diffraction because of the large sample size needed, but can be important for X-ray powder diffraction where the sample size is smaller and the effects of the sample preparation are more significant.

In order to minimise this during powder X-ray diffraction, it is crucial to pack a sample holder by a process which seeks to minimise crystallite orientation. This can be done by back-filling the sample holder, using crystallites of similar size, and the use of transmission geometry over flat plate Bragg-Bretano. Transmission gives an extra axis of rotation over a spinning flat-plate setup, further improving the powder averaging of the reflections. Back filling in flat plate geometry involves filling an enlarged cavity between the sample holder and stroking a glass microscope slide over the surface to retrieve the excess sample. This method increases the sample holder's volume reducing the problems of confinement.

Mathematically, preferred orientation can be modelled using spherical harmonics. The mathematical implementation set out in GSAS can be found in the GSAS

manual [120]. The system chosen is cylindrical with the following values for the Eulerian angles, $\Omega = -90°, X = 0°, \Psi = 0°$, with up to 12 terms refined.

3.6.3 X-ray powder diffraction techniques

All iron jarosite X-ray diffraction data presented in this thesis were collected in Bragg-Bretano geometry using a Bruker D8 diffractometer with $CuK_{\alpha 1}$ radiation and a position sensitive detector (PSD). The PXRD patterns have a step size of $\Delta(2\theta) = 0.073°$ and were taken over the angular range 2θ range 5°-70°. The typical scan time was 65 minutes; sample rotation speed was 15 rpm. Samples were lightly ground and a small amount was added to the centre of a flat low-background silicon plate. Two drops of acetone were added to make a thin slurry which was left to dry.

The primary purpose of these studies was to check for phase purity and to catalogue any changes in lattice parameters (as expected from Vegard's law [121]) with synthesis conditions. Lattice parameters were refined using the Rietveld method from a previously known model for the hydronium jarosite [21]. Only lattice parameters were obtained from these data because of the high background due to the fluorescence of Fe under illumination by Cu K_α radiation. The Rietveld software used was GSAS [122, 123], implementing a constant wavelength pseudo-Voigt profile function modified by Finger, Cox and Jephcoat [124] which is implemented in GSAS as profile function 3.

Diffraction patterns for a small selection of samples were measured on a Panalytical X'pert Pro with a Co anode and a Ge <111> monochromator, producing X-rays with a wavelength of 1.7929 Å. The samples were back filled into a sample holder, which was then spun, and measured over the 2θ range 5° and 143° with a step size of 0.0167°. A Co source had to be used to detect any small amounts of unwanted Fe-hydroxy-sulphates present that would be undetectable using Cu K_α radiation.

3.6.4 Neutron powder diffraction techniques

The neutron diffraction presented in this thesis were obtained at a nuclear reactor source and diffraction experiments from these sources are usually at constant wavelength. Neutrons are produced in a nuclear fission reactor (60-100 MW). Most of the energy is dissipated as heat. The neutrons leave the reactor core via a moderator, with wavelengths typically in the range λ =1-2 Å for room temperature moderation.

Neutron powder diffraction experiments were performed on a double axis diffrac-

tometer. This consists of one axis which contains the monochromator that will define the wavelength of neutrons to be used in the diffraction experiment, and the second axis is where the sample is positioned. As neutron flux is relatively low, the intensity of scattered neutrons as a function of 2θ is often measured using a position sensitive detector which is radially integrated to give a 1 dimensional powder pattern.

Constant wavelength powder diffraction patterns for this thesis were measured using the medium resolution instrument, D20, at the Institut Laue-Langevin (ILL), a schematic of D20 is shown in Figure 3.5. The ILL hosted Rietveld software, Fullprof [125], was used for the Rietveld refinements.

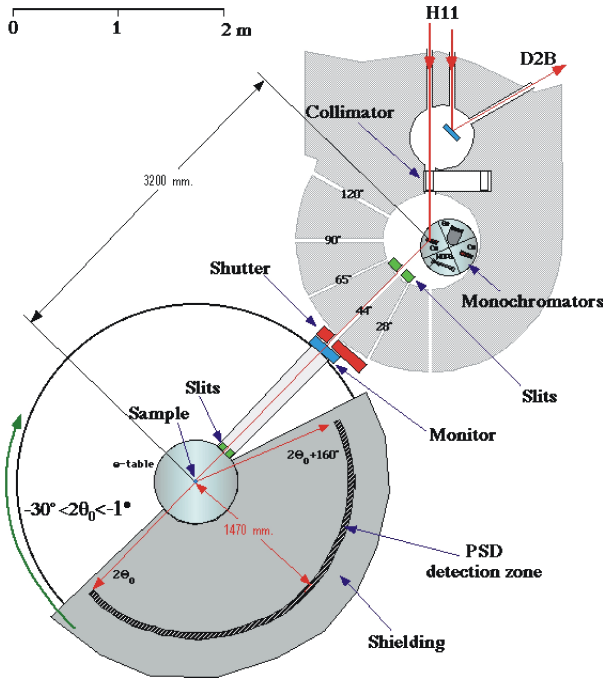

Figure 3.5: Schematic diagram of the medium resolution high flux diffractometer D20 at the ILL. The monochromator is a <111> single Ge crystal. The detector is a position sensitive detector, covering 160° 2θ, containing ^{3}He and propane comprising 1600 microstrip wires at 0.1° intervals. The schematic is taken from the D20 manual [126].

3.7 Single Crystal Diffraction

Single crystal diffraction provides a very large number of independent reflections with minimal overlap of reflections. This means space group determination and structure solution becomes almost trivial given current computing capabilities and the modern methods employed such as direct methods and Patterson searching,

which are explained in further detail in many texts published by the International Union of Crystallography [127].

3.7.1 Data collection techniques

Single crystal X-ray diffraction studies were carried out at the National Crystallographic Service based at Southampton University and at the UK synchrotron at Daresbury. Most data sets were collected at Southampton which has two identical single crystal diffractometers (Dell boy and Damien) side-by-side, though one is equipped with a focusing mirror to improve the brilliance of the X-rays.

Suitable crystals were selected using a light microscope fitted with two polarized filters. Crystal quality was tested by viewing the transmission of polarized light through the crystal based upon the extinction phenomenon. The result of the extinction phenomenon is that a single crystal (with the exception of cubic crystal classes) will transmit polarized light along at least one axis, and upon rotation of 90° the crystal should appear opaque if it is a true single crystal. The crystal size varied between 20-50 μm across a face. Each crystal was mounted upon a glass fibre and affixed using adhesive. The crystals were aligned using an automated process controlled by software. X-Rays (Mo K_α, $\lambda = 0.71073$ Å) were generated using a Bruker-Nonius FR591 rotating anode and collected on a four axes Bruker-Nonius 95 mm KappaCCD camera on a κ-goniostat. The sphere of diffraction from $2.91 < \theta/^\circ < 27.48$ was collected at room temperature and $\sim$80 K using an Oxford Cryosystems cryostream 700 series. The crystal-to-detector distance was 30.00 mm with a d-spacing resolution range of 7.00 -0.77 Å. Position and peak intensities were extracted from the raw data using DENZO SMN and scaled using SCALEPACK; SADABS V2.10 [128] was used for absorption correction.

Crystals too small for analysis at Southampton were sent to the Daresbury Synchrotron Radiation Source (SRS), station 9.8 [129]. The wavelength source for the majority of the samples was 0.6768 Å and the data were collected using a Bruker SMART APEX2 CCD diffractometer [130] with a Si <111> monochromator through a sphere of diffraction of $3.26 < \theta/^\circ < 29.36$ from 15 K up to room temperature. Low temperatures were achieved using a helium cryostat. Position and peak intensities were extracted using Bruker SAINT [131] and absorption corrections made using SADABS [128]. The wavelength selected (0.6768 Å) produced no anomalous dispersion with the Fe.

Absorption corrections are very important for single crystal diffraction data anal-

ysis in contrast to most powder diffraction. In single crystal diffraction, the size and shape of the crystal affect the path the X-rays travel through and thus the degree of adsorption. The jarosite crystals are pseudo-cubes and therefore absorption is near uniform in all directions throughout the crystal, and so the only consideration is size. The crystals themselves are fairly small (30-100 μm across a face) and thus extinction is minimal and adsorption is relatively low.

All data were collected assuming P1 symmetry rather than trigonal to ensure all equivalent reflections were collected and to confirm that there was no lower symmetry present. More importantly, it was determined that allowing SHELX-97 to merge the data rather than SCALEPACK produced more consistent results.

3.7.2 Structure solution and refinement

XPREP was used for space group determination, data merging and generator of a SHELX input data file. SHELX-97 [132], executed under WinGX V1.7 [133], was used for structure solution and refinement with the inbuilt scattering factors of SHELX-97 being used.

Refinement in SHELX-97 was undertaken using least-squares minimisation: the refinement is carried out against F^2 which ensures a more accurate result as better standard deviations can be obtained, $\sigma(F_0^2)$, however, this is computationally more extensive. This leads to an $R1$ factor (3.11) along with the corresponding Goodness-of-Fit (3.12),

$$R1 = \left(\frac{\sum [w(F_0^2 - F_c^2)]^2}{\sum w[F_0^2]^2} \right)^{\frac{1}{2}} \tag{3.11}$$

$$G_{off} = \left(\frac{\sum [w(F_0^2 - F_c^2)]^2}{n - p} \right)^{\frac{1}{2}} \tag{3.12}$$

where n is the number of reflections and p is number of parameters refined.

After the initial refinement which involved positional parameters and isotropic displacement for all atoms were concluded, the symmetry of the system was checked using PLATON V40M [134, 135]. The ADDSYM function of PLATON confirmed the presence of a mirror plane and the symmetry was increased to $R\bar{3}m$ for the final structure refinement which included anisotropic displacement for all atoms except the hydroxyl hydrogen. Other crystallographic works have confirmed the trigonal crystal system and $R\bar{3}m$ space group [1, 136] for jarosites.

Chapter 4

Synthesis of iron jarosites

Most of the jarosites are readily precipitated from acidic solutions of Fe^{3+} and the relevant A-site sulphate at or below 100 °C [7]. In order to prepare materials with a very good or near perfect stoichiometry, and with good crystallinity requires the application of higher temperatures ($T > 100$ °C), supercritical conditions, and the use of pressure vessels, a technique referred to as *forced hydrolysis*. The control and linking of this chemistry to the magnetic properties of the resultant jarosites forms a major part of this thesis.

It is notable that as well as being magnetically distinct from the other Fe-jarosites, the hydronium jarosite shows itself to be unlike the other jarosites in its chemistry: it is the only Fe-jarosite that can only be prepared under hydrothermal conditions [3]. We show in Chapters 5-7 by a combination of studies of the stoichiometry, crystal structure and magnetic properties that the differing chemistry of this hydronium jarosite plays an important role in its failure to condense into a conventional Néel ground state, and to instead form an exotic topological spin-glass state.

4.1 Background to syntheses

Jarosites are prone to nonstoichiometry and this has major implications for their magnetism [3, 12]. Vacancies or substitution with diamagnetic ions on the B-site will dilute the *kagomé* network, breaking down the geometric arrangement of antiferromagnetically coupled ions, that give rise to the magnetically frustrated properties [137]. The studies of the effects of such disorder in *kagomé* networks investigated by computational studies [81, 88, 138, 139] or experimental [21, 137] methods

have given very different conclusions, suggesting either a remarkable robustness to disorder or that minimal dilution will destroy the frustrated manifold. This uncertainity demonstrates that the need to produce near 100% Fe coverage is crucial for research [19–21].

Many methods are in use to produce jarosites synthetically in order to investigate and exploit their nonstoichiometric nature [1, 3, 7, 12]. Principally, research has focused on mining processes to either remove unwanted chemical elements or to ensure the desired elements are not absorbed by the jarosite structure [1–3, 7, 12] which forms during the hot acid leaching process used in mining.

The commercial technique to remove Fe^{3+} ions is to employ hydrothermal methods operating up to 200 °C [140], known as "forced hydrolysis". A typical reaction for jarosite formation during industrial leaching processes is;

$$3\,Fe_2(SO_4)_3 + 14\,H_2O \longrightarrow 2\,H_3OFe_3(SO_4)_2(OH)_6 + 5\,H_2SO_4 \tag{4.1}$$

The majority of jarosites are easily synthesised, with the notable exception of hydronium jarosite, which is only readily synthesised under hydrothermal conditions [3, 141]. Methods to increase Fe occupation and determine why hydronium jarosite is magnetically different have led to several new hydrothermal methods based upon super-critical water heated under pressure [18, 19].

4.2 Natural jarosite formation

Jarosites form in a pH range of 0.8 - 1.8 [3]: a higher pH will result in the formation of goethite, FeO(OH), and hematite, Fe_2O_3 [48]; a lower pH will result in the formation of unwanted iron oxyhydroxy sulphates [48]. In nature, jarosites occur through the weathering process of pyrite, FeS_2 [39, 142]. High concentrations of Fe^{2+} are released from the dissolution of FeS_2 and which decreases the pH of the local water area [3,143] and Fe^{2+} is oxidised to Fe^{3+} through either microbial action or the action of dissolved oxygen [16, 42]. Around these Fe^{3+} centres, chains of hydroxysulphates attach themselves to form the characteristic iron flocs [16, 42, 144]. Extremely low values of pH and the incorporation of a suitably sized cation will cause jarosite precipitation [140] with the following formula: $A_{1-x}(H_3O)_xFe_{3-y}(SO_4)_2(OH)_{6-3y}(H_2O)_{3y}$, where $A = K^+$, Na^+, Ag^+, Rb^+, NH_4^+, H_3O^+, Pb^{2+}, Tl^+ [2, 3, 7, 12].

The high water content and the low-temperature formation conditions in na-

ture can lead to a large deviation from the ideal stoichiometry [3, 7, 12]. Naturally occurring jarosites may be charged balanced by the incorporation of other cations in the B site which are not trivalent cations, such as Cu^{2+} in beaverite, $PbCu(FeAl)_2(SO_4)_2(OH)_6$ [145], or Zn^{2+} in beaverite-Zn, $PbZn(FeAl)_2(SO_4)_2(OH)_6$ [8, 11] and other combinations to form a multitude of similar mineral types [3, 13, 47, 146]. If there are Fe deficiencies, charge balance requires the replacement of an A-site cation with a neutral H_2O unit or protonation of the bridging OH groups. Likewise, increasing incorporation of water will be charged balanced by Fe vacancies [3, 12, 144]. Many naturally found pure A-site jarosites for instance, K^+, Na^+ or Ag^+, have a high Fe content with almost 100% Fe iron coverage though the necessary synthesis conditions remain unclear. For further details refer to the thesis by Smith A.M.L. [14].

4.3 Hydrothermal synthesis of Fe jarosites - forced hydrolysis

Jarosites can be readily synthesised in the laboratory using boiling water (98 °C) [3], but unfortunately this leaves little or no control over the stoichiometry and quality of the crystalline product [14, 137]. Another drawback of sub 100 °C reactions is the inability to make hydronium jarosite [1, 3].

Forced hydrolysis is one mechanism to enhance the quality of jarosite precipitation [19, 140, 147]. Jarosite formation is a hydrolysis reaction [16, 48, 141], where the pH continually drops as jarosite precipitation increases [16]. Hydrothermal techniques increase the hydrolysis potential of jarosite precipitation and allow stabilisation of the jarosite precursor during synthesis [144, 148]. Forced hydrolysis conditions use very high concentrations of $Fe_2(SO_4)_3$ and the appropriate A site - sulphate. Dutrizac [3] specified using 3:1 ratio of A-site sulphate to $Fe_2(SO_4)_3$, to minimise the competition from the $(H_3O)^+$ ion. Kubisz [12] instead suggested the use of A-site hydroxides instead as this improves the Fe^{3+}:SO_4^{2-} ratio (2:3) and improves the A-site stoichiometry [149], though both points have only been proved through repeated experimentation. Certainly for sodium jarosite preparation, the use of NaOH produces far better quality jarosite [2]. In some of the reactions the pH was adjusted using LiOH to be in the range 1.6 - 1.8; Li^+ ions are not incorporated into the jarosite structure [2, 5].

Typically the solution used for forced hydrolysis are at 100-150 °C in an PTFE

lined steel bomb [3,21] (usually a Parr design) or a titanium baffled autoclave [18,19] for 8-72 hours. The solution is decanted off to leave behind the jarosite which is washed with distilled water several times then dried in an oven at 110-120 °C for at least 4 hours. The yield increases with increasing temperature, longer reaction time and higher concentration.

4.3.1 Pyrex pressure tubes

Pyrex pressure tubes, described in Section 3.1, produce higher quality jarosite samples and greater yields than those synthesised using PTFE lined steel bombs, which is highlighted in this chapter. Before using the Pyrex tubes it was necessary to replace the original nitrile O-rings with Viton O-rings (Figure 4.1(c)). Viton can withstand sustained temperatures up to 250 °C, and has a far greater resistance to super-critical water and low pH conditions. Also, the screw threads on the front mounted O-ring PTFE screw tops (Figure 4.1) suffered from PTFE deformation as a consequence (Figure 4.1(b)) of the reaction conditions, therefore more PTFE screw tops were machined.

4.3.2 Forced hydrolysis - hydronium jarosites

All forced hydrolysis hydrothermal syntheses used Pyrex pressure tubes and the concentration of 0.55 M Fe^{3+}, that was used by Earle *et al.* [19]. Earle *et al.* used mixtures of MeOH and H_2O as a solvent and found that the ideal solvent mix to be a 50/50 ratio, respectively. They found that the best conditions for hydronium jarosite synthesis using a 50/50 MeOH:H_2O solvent mix were a 15 cm^3 solution of 0.275 M $Fe_2(SO_4)_3.5H_2O$ (0.55 M Fe^{3+}) heated at 120 °C for 3 days using a Parr autoclave with a PTFE liner. Earle *et al.* claimed that thermo-gravimetric analysis (TGA) data of the resultant jarosite indicated that the concentration of Fe^{3+} vacancies is less than 2%. Using Pyrex tubes and extending the Earle *et al.* [19] method allowed the synthesis of hydronium jarosites with a wide range of spin-glass freezing temperatures.

Hydronium jarosite samples were synthesised using a modification of Earle's method: 0.275 M $Fe_2(SO_4)_3.5H_2O$ (0.55 M Fe^{3+}) were made up to 15 cm^3 solutions with a solvent mix ranging from 100% H_2O to 90/10 MeOH:H_2O. The 23 cm^3 capacity Pyrex pressure tubes were used primarily for hydronium jarosite synthesis. Preceding trial reactions had revealed that the optimum reaction time was 21

(a) An Ace Glass Pyrex tube (size #15) with a front mounted O-ring seal positioned at the end of the PTFE screw top. Jarosite formation near to the PTFE screw top can be seen.

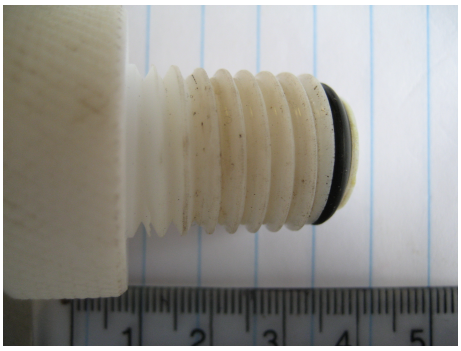

(b) Ace Glass #15 PTFE screw top showing the thread. This was the only size used, though the thread itself was prone to deformation and replacement PTFE screw tops had to be made.

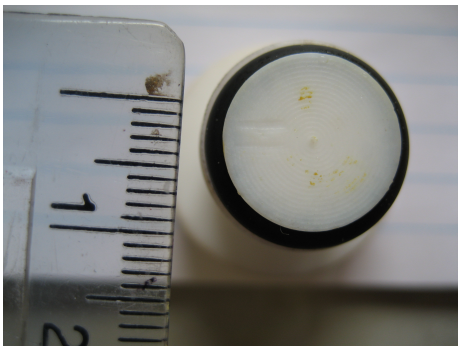

(c) Ace Glass #15 PTFE screw top showing the front mounted Viton O-ring at the end of the PTFE screw top.

Figure 4.1: The Pyrex tubes from Ace Glass Inc., provided an excellent reaction vessel for hydrothermal synthesis: they improve the temperature gradient, provide a better surface for jarosite crystal growth and allows visual inspection. Positioning the Pyrex tube at an angle away from vertical of approximately 35 ° was found to be optimum for crystal growth. The divisions on the ruler show millimetres.

hours and the temperature range for single-phase hydronium jarosite precipitation was 120 - 150 °C (Section 4.4.1). The full listing of yields, together with spin-glass freezing temperature are listed in Tables 4.1 and 4.2.

Increasing temperature or MeOH concentration was found to increase yields, though there is a working limit to these parameters. The maximum working temperature for synthesis using 100% H_2O or H_2O/MeOH mix as a solvent is 150 °C as above that temperature hematite forms. No jarosites can be formed in a MeOH concentration greater than 90% at any temperature, but this concentration limit is reduced with increasing temperatures leading to the formation of unwanted iron oxy-hydroxy sulphates below 150 °C, many of which are X-ray amorphous. The use

of Pyrex pressure tubes and MeOH/H_2O as the solvent heavily influenced the crystal growth of hydronium jarosites (Section 4.4).

Table 4.1: Synthesis conditions for hydronium jarosites using pure H_2O as solvent, showing temperature, time, initial starting pH, yield and spin glass freezing temperature, T_g.

Sample ID	Temp (°C)	Time (hrs)	pH (start)	yield (g)	T_g (K) ± 0.2K
H3OFe016	150	67	1.06	0.458	15.8
H3OFe021	150	4	1.10	0.310	15.5
H3OFe022	150	7	1.10	0.293	N/A
H3OFe022b	150	7	1.10	0.337	N/A
H3OFe023	150	15	1.10	0.470	N/A
H3OFe024	150	21	1.10	0.498	15.6
H3OFe024b†	150	21	1.22	0.5283	16.0
H3OFe025	150	28	1.10	0.422	N/A
H3OFe025b	150	28	1.10	0.433	N/A
H3OFe026	150	48	1.10	0.508	N/A
H3OFe027	150	> 80	1.10	0.530	15.7
H3OFe029	130	21	1.15	0.186	17.7
H3OFe030	140	21	1.15	0.340	16.3
H3OFe031	120	21	1.13	0.081	19.7
H3OFe032	120	21	1.15	0.057	N/A
H3OFe033	125	21	1.15	0.101	18.8
H3OFe034	110	21	1.15	0.022	~ 22
H3OFe035	100	21	1.15	nil	N/A
H3OFe040	120	72	1.13	0.122	~ 20
H3OFe041	120	48	1.13	0.178	N/A
H3OFe042	135	21	1.56	0.371	16.9
H3OFe043‡	145	21	1.44	0.536	14.7
H3OFe044	127	21	1.36	0.312	18.0
H3OFe045	138	21	0.97	0.292	17.5
H3OFe046	142	21	0.90	0.296	17.2
H3OFe047	142	21	N/A	N/A	16.8
H3OFe048	138	21	N/A	N/A	16.6
H3OFe049	145	21	N/A	N/A	15.8
H3OFe050	150	21	N/A	N/A	N/A

† The sample was synthesised in 25 cm^3 of solution.
‡ No given explanation for such a low T_g using 100% H_2O as solvent.
N/A indicates that no measurement was taken for that parameter

4.3.3 Forced hydrolysis - non-hydronium jarosites

Non-hydronium jarosites were synthesised using Pyrex pressure tubes and 0.55 M Fe^{3+} 15 cm^3 solutions (100% H_2O solvent) with a corresponding A-site sulphate or hydroxide dissolved in the 0.55 M Fe^{3+} solution. The concentration of the A-site sulphate was varied to allow competition between the A-site cation and H_3O^+ ion to see what influence over the magnetic transition temperature(s) this had. Synthesis conditions and yields for non-hydronium jarosites are shown in Table 4.3.

Table 4.2: Synthesis conditions for hydronium jarosites using H_2O/MeOH solvent mix. Showing temperature, initial starting pH, yield and spin glass freezing temperature, T_g. Reaction time was 21 hours.

Sample ID	Temp (°C)	H_2O (%)	pH (start)	yield (g)	T_g (K) ± 0.2K
H3OFeS1	150	90	1.22	0.514	15.7
H3OFeS2	150	80	1.17	0.571	15.4
H3OFeS17	150	75	1.06	0.584	14.6
H3OFeS3	150	70	1.12	0.655	14.8
H3OFeS18	150	65	1.00	0.683	14.5
H3OFeS4†	150	60	1.01	0.711	13.9
H3OFeS19	150	55	0.91	0.808	~ 100§
H3OFeS5†	150	50	0.90	0.843	N/A
H3OFeS6‡	150	40	0.88	0.851	~ 100§
H3OFeS7‡	150	30	0.80	1.104	N/A
H3OFeS8‡	150	30	0.72	1.146	N/A
H3OFeS30	140	90	1.42	0.573	14.2
H3OFeS31	140	80	1.13	0.415	15.1
H3OFeS32	140	70	1.06	0.543	14.4
H3OFeS33	140	60	1.00	0.631	13.7
H3OFeS34	140	50	0.85	0.747	13.9
H3OFeS35‡	140	40	0.82	0.852	12.3
H3OFeS36‡	140	30	0.79	1.022	11.5
H3OFeS37‡	140	20	0.73	1.134	10.9
H3OFeS38⋆	140	10	N/A	0.977	N/A
H3OFeS21	130	90	1.10	0.363	17.4
H3OFeS22	130	80	1.29	0.379	16.6
H3OFeS23	130	70	1.12	0.556	12.0
H3OFeS24	130	60	1.06	0.666	14.1
H3OFeS25	130	50	1.18	0.559	12.9
H3OFeS26	130	40	1.15	0.745	12.0
H3OFeS27†	130	40	1.00	0.903	11.6
H3OFeS28✠	130	30	0.88	0.765	10.9
H3OFeS29⋆	130	20	0.97	1.118	N/A
H3OFeS9	120	90	1.05	0.134	18.8
H3OFeS10	120	80	1.03	0.237	18.4
H3OFeS11	120	70	1.00	0.341	17.2
H3OFeS12	120	60	0.95	0.479	15.8
H3OFeS13	120	50	0.93	0.581	14.8
H3OFeS14	120	40	0.89	0.687	12.7
H3OFeS15✠	120	30	0.83	0.643	12.1
H3OFeS16✠	120	20	0.72	0.425	11.3
H3OFeS20⋆	120	10	0.73	0.249	~ 88§

N/A indicates that no measurement was taken for that parameter

† sample contains unwanted Fe hydroxy-sulphates

‡ predominantly unwanted Fe hydroxy-sulphates

§ separation in ZFC/FC.

✠ contains Schwertmannite (Figure 4.4(e))

⋆ Possible Mikasaite, crystalline $Fe_2(SO_4)_3$ (Figure 4.7(f))

Table 4.3: Syntheses conditions for non-hydronium jarosites using Pyrex tubes under hydrothermal conditions all solutions were made up to 15 cm^3 of H_2O. All reactions were at 130° C for 21 hours unless otherwise stated.

Sample ID	A-site SO_4/OH	A-site mass (g)	A^+ (M)	Fe^{3+} (M)	yield (g)	T_C (K)
KFe1†*	KOH	0.170	0.202	0.55	1.155	64.5, 45.0
KFe2◇	K_2SO_4	0.784	0.300	0.275	0.693	N/A
KFe3	KOH	0.285	0.339	0.55	1.334	64.2
KFe4	KOH	0.124	0.148	0.55	1.134	(64.2), 50.3
KFe5	K_2SO_4	0.526	0.200	0.55	1.309	63.55, 47.0
KFe6	K_2SO_4	0.121	0.046	0.55	0.905	47.3
NaFe1§	NaOH	0.201	0.330	0.55	1.186	(60.75), 43.9
NaFe2§	NaOH	0.073	0.120	0.55	0.926	(61.0), 43.0
NaFe3§	NaOH	0.054	0.900	0.55	0.724	(60.0), 39.5
AgFe1⋈	Ag_2SO_4	0.979	0.400	0.55	1.121	N/A
AgFe2‡	Ag_2SO_4	0.382	0.160	0.55	1.245	N/A
AgFe3	Ag_2SO_4	0.210	0.043	0.55	0.937	44.3
RbFe1	Rb_2SO_4	0.559	0.420	0.55	1.134	63.85, (50.0)
RbFe2	Rb_2SO_4	0.339	0.250	0.55	1.044	64.2, 50.65
RbFe3	Rb_2SO_4	0.156	0.039	0.55	0.783	45.0
NH4Fe1	$(NH_4)_2SO_4$	0.329	0.330	0.55	0.931	61.35, 52.05
NH4Fe2†	$(NH_4)_2SO_4$	0.105	0.330	0.55	1.113	43.5
NH4Fe3†	$(NH_4)_2SO_4$	0.324	0.110	0.55	1.029	61.25, 50.5
KFe natural⋆						63.3, 50.3

N/A indicates that no measurement was taken for that parameter

† pH adjusted with LiOH to bring the starting pH above 1.6.

* Reaction time of 68 hours at 110° C

◇ Reaction time of 48 hours at 110° C

§ Sodium jarosite could only be successfully synthesised using NaOH

⋈ Reaction temperature of 140° C

‡ Contains impurities, Ag_2SO_4 and Ag

⋆ BM, used as a reference.

Unfortunately, the jarosites formed following the conditions summarised in Table 4.3 were too small for single crystal X-ray diffraction studies and an alternative method had to be used to grow larger crystals.

4.4 SEM results for the hydronium jarosites

Scanning electron microscopy (SEM) using a JEOL JSM-6301F was extremely useful in examining sample quality and provided detailed images showing the diverse morphologies that hydronium jarosite can produce.

4.4.1 SEM results for 100% H_2O solvent hydronium jarosites

SEM images (Figure 4.2) confirmed previous observations with the naked eye that crystal size and quantity of single crystals increases with temperature.

Using 100% H_2O as the solvent for hydronium jarosites synthesis, the greatest yield and the largest number of pseudo cubes (with faces up to $\sim 150\ \mu m$) form at 150 °C (Figure 4.3), Greater temperatures result in the formation of hematite. Crystal quality reduced at temperatures below 145 °C [136]. The crystal growth appears to stall at the stage where the pseudo-cubes form interlinking sheets. Here, the individual pseudo cubes have not reached a sufficient size to fall away intact from the sheet. Instead, upon cooling, the sheets break apart and fracture many of the individual pseudo cubes in the process. Higher temperatures ensure the formation of larger individual crystals and produce a much darker brown/ochre colour, whereas poorer formed crystals are lighter in colour.

The angle of elevation of the Pyrex tubes also played an important role in crystal growth: in an upright position single crystal growth is limited because the crystal growth requires a surface to grow along and the relatively high density of jarosite means that when a certain size has been achieved the crystallites fall and collect at the bottom poorly formed. An explanation for this crystal growth is outlined in the following sections with reference to the SEM images.

4.4.2 Ostwald ripening and crystal growth

Jarosite crystal growth under hydrothermal synthesis conditions follows thermodynamic process of Ostwald ripening [16]. There is a balance between kinetic and thermodynamic processes in the reaction. From the start of the reaction there are many nucleation sites of jarosite precursors and unwanted phases of Fe oxy-hydroxy sulphates [16]. In Ostwald ripening the kinetically favoured unwanted Fe-oxy hydroxy sulphates phases form rapidly and produces more nucleation sites. These then dissolve over time and the thermodynamically favourable jarosite structure grows. These crystals continue to dissolve fuelling continued growth of the remaining crystals and increased crystal size.

Insufficient reaction time leads to few and only poorly formed jarosite crystals amongst a multitude of precursor nucleation sites as shown in Figure 4.3. After 15 hours, regular-sized pseudo cubes of jarosite are produced, though plenty of precursor debris still remains. Increasing reaction time produces larger crystals and less

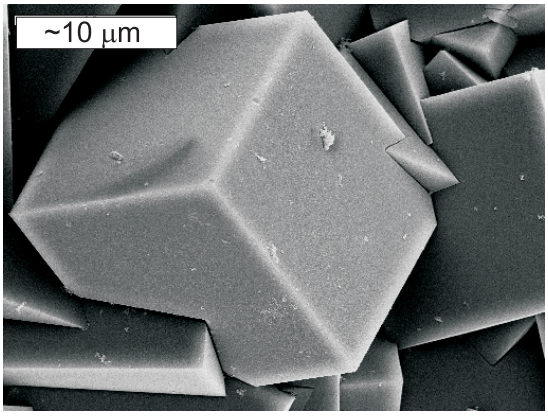

(a) 100% H_2O 120 °C 21 hours

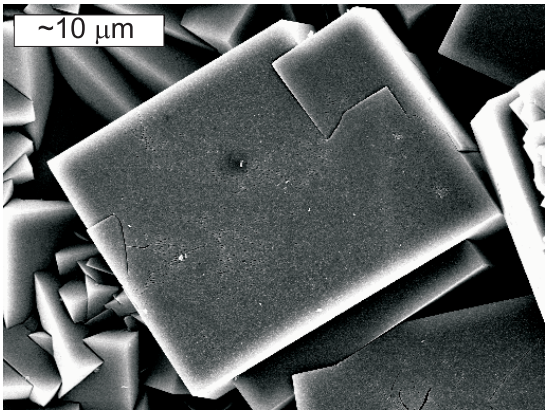

(b) 100% H_2O 125 °C 21 hours

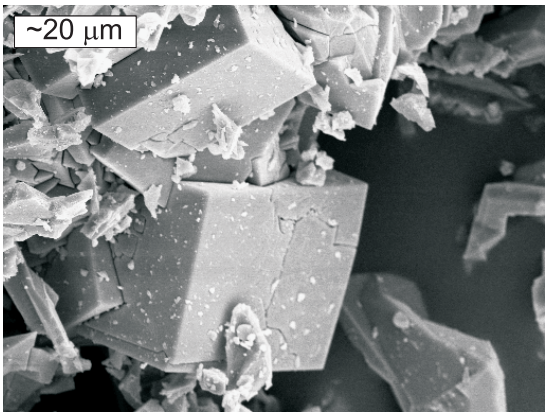

(c) 100% H_2O 130 °C 21 hours

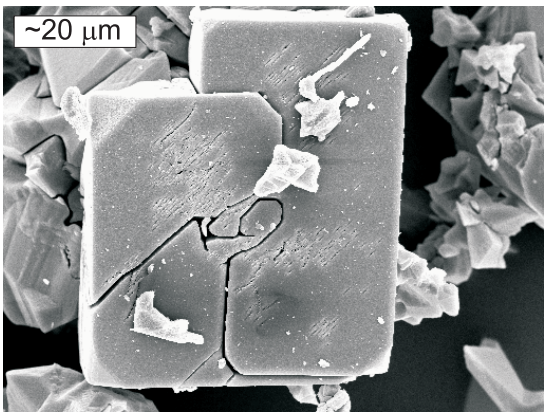

(d) 100% H_2O 140 °C 21 hours

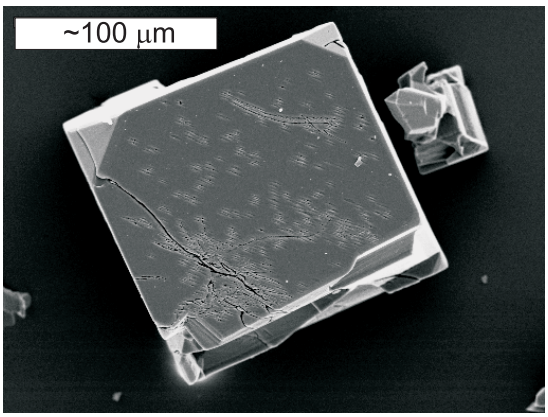

(e) 100% H_2O 150 °C 21 hours

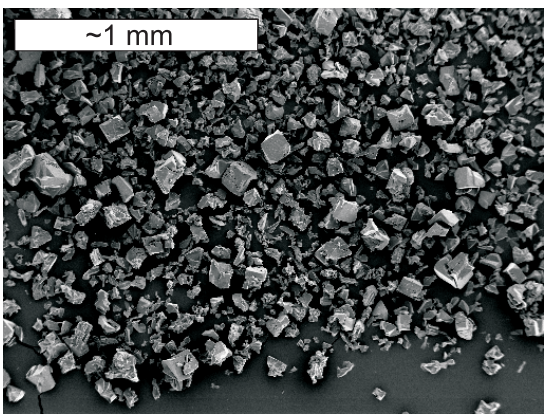

(f) 100% H_2O 150 °C 21 hours

Figure 4.2: Jarosites synthesised in 100% H_2O for 21 hrs; the only variable is temperature and increasing temperature improves the size, quality and quantity of hydronium jarosite crystals when synthesised in 100% H_2O as a solvent.

jarosite debris. After a longer time period, most debris comes from broken jarosite crystals rather than remnant nucleations sites. The beginning of pitting can be seen on the face of the pseudo cubes at 15 hours (Figure 4.3(b)) and this becomes more pronounced with striations appearing regularly across the faces and even crystal deformation with increasing time (Figures 4.3(c), 4.3(d), 4.3(e) and 4.3(f)). The pitting and striations result from the ever decreasing pH levels, that etch at the surface, firstly stripping out the A-site $(H_3O)^+$ [17]. Continued etching leaves triangular shaped holes consistent with the trigonal crystal class of jarosites underneath the pseudo cube veneer (Figure 4.3(e)).

A reaction time of 21 hours was found to be a good balance between crystal growth, ensuring phase pure samples, and efficiency of synthesis. Magnetic sample measurements later confirmed that reaction times greater than 15 hours did not affect the magnetic susceptibility of jarosites formed under identical temperatures using 100% H_2O as the solvent. This reaction time was then applied to all further jarosite production to ensure consistency.

4.4.3 SEM results for MeOH/H_2O solvent mix hydronium jarosites

Introduction of MeOH as a solvent increases the effective reaction temperature and can radically change the nucleation and subsequent jarosite crystal growth; and for a given reaction temperature greater yields are achieved with increasing MeOH concentration. There is a limit to MeOH concentration: no jarosite can be made with a MeOH concentration of 90% or greater under hydrothermal conditions. High MeOH concentrations produce unwanted iron oxy-hydroxy sulphates at elevated temperatures, at lower temperatures high MeOH concentrations drive the system to form Schwertmannite ($Fe_8O_8(OH)_{8-2x}(SO_4)_x \cdot nH_2O$ - $Fe_{16}O_{16}(OH)_{16-2z}(SO_4)_z$ [150]) Figures 4.4(e) and 4.4(f). At intermediate temperatures of $\sim$130 °C, the morphology of jarosite changes again to form interpenetrating triangular prisms, leading to the formation of Schwertmannite at higher MeOH concentrations shown in Figure 4.5 and later Figures. Continued increase in temperature causes a mottling of the pseudo-cubes of jarosite and produces unwanted Fe oxy-hydoxy sulphates.

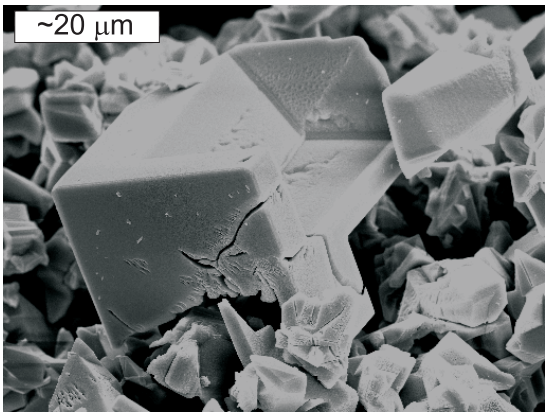

(a) 100% H_2O 150 °C 4 hours

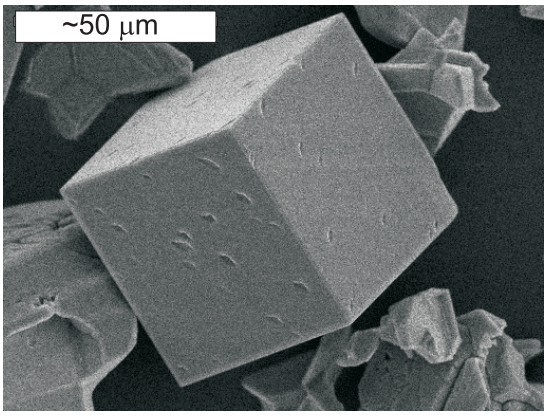

(b) 100% H_2O 150 °C 15 hours

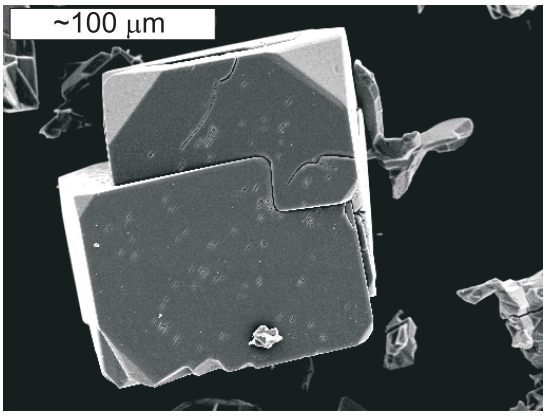

(c) 100% H_2O 150 °C 21 hours

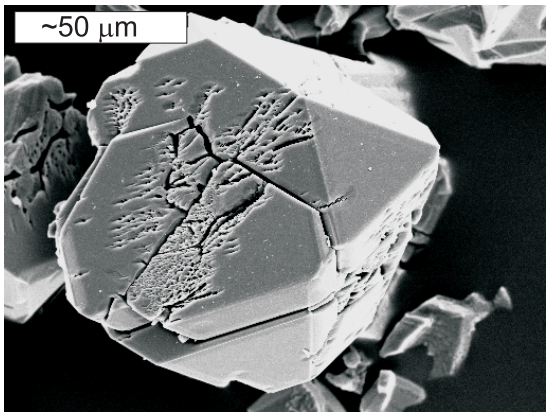

(d) 100% H_2O 150 °C 67 hours

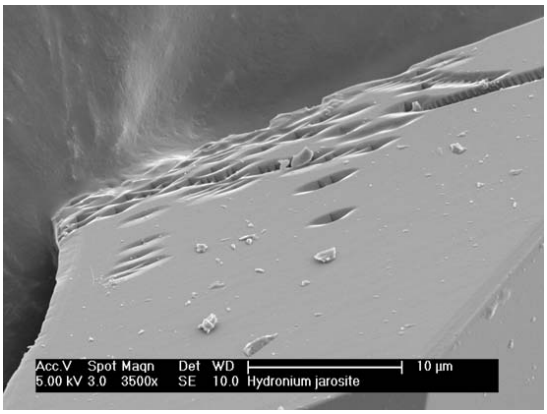

(e) 100% H_2O 150 °C 67 hours

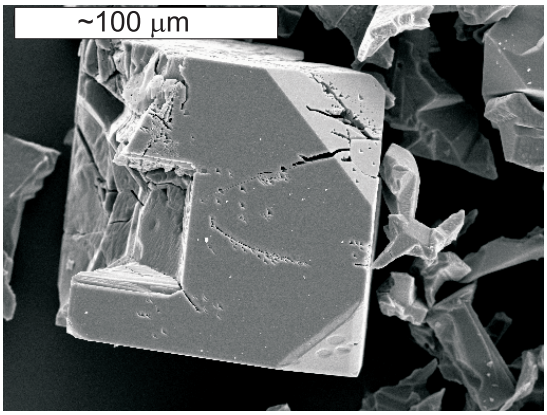

(f) 100% H_2O 150 °C 80+ hours

Figure 4.3: Jarosites synthesised at 150 °C in 100% H_2O solvent with varying time. Increasing reaction time improves the size of the jarosite crystals and reduction in precursor debris, though this results in pitting of the surface eventually creating triangular holes. The reaction time, determined to be 21 hours, is a balance to ensure no remaining unknown precursor material is left and that there are good well-sized formed crystals.

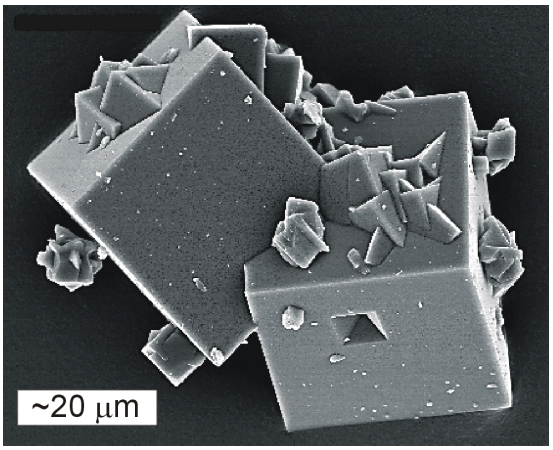

(a) 20:80 MeOH:H_2O 120 °C 21 hours

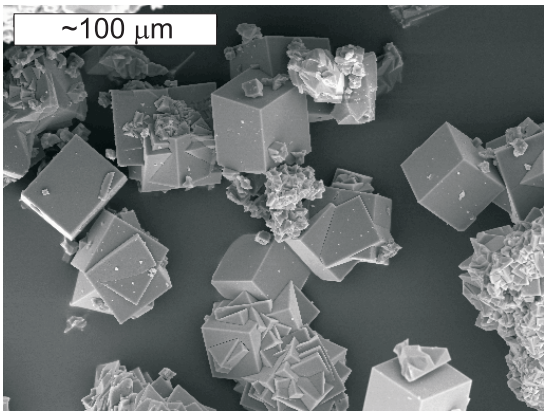

(b) 20:80 MeOH:H_2O 120 °C 21 hours

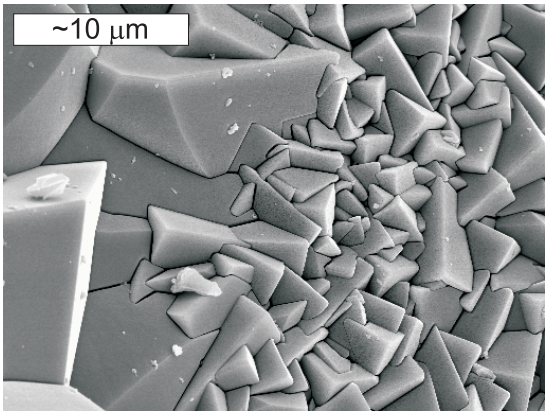

(c) 60:20 MeOH:H_2O 120 °C 21 hours

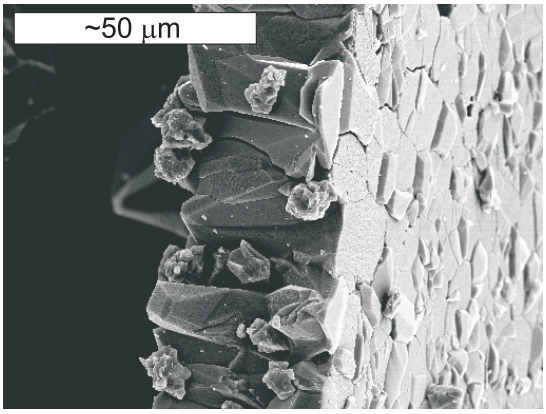

(d) 60:20 MeOH:H_2O 120 °C 21 hours

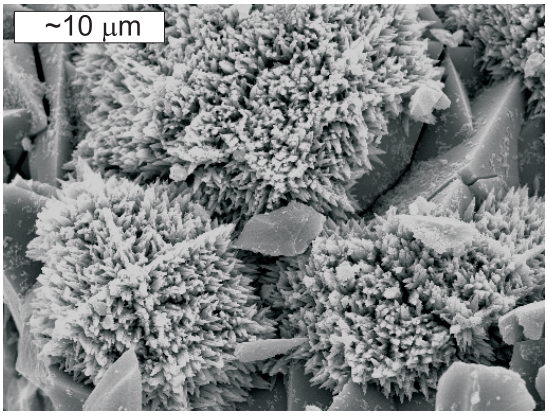

(e) 80:20 MeOH:H_2O 120 °C 21 hours

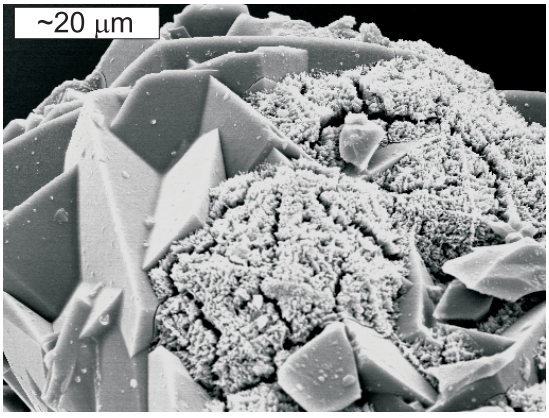

(f) 80:20 MeOH:H_2O 120 °C 21 hours

Figure 4.4: SEM images of the products of various H_2O/MeOH mixes at 120 °C. Low concentrations of MeOH produce large single crystals - though with an increase in twining, interpenetrating crystals and stacking faults due to rapid crystal growth possibly centred on the inversion centre. Crystal size is similar compared to 100% H_2O preparations at 150 °C suggesting low MeOH concentrations lower the effective temperature. High MeOH concentrations eventually leads to unwanted Fe oxy-hydroxy sulphates as shown by the occurrence of Schwertmannite (coral-like appearance).

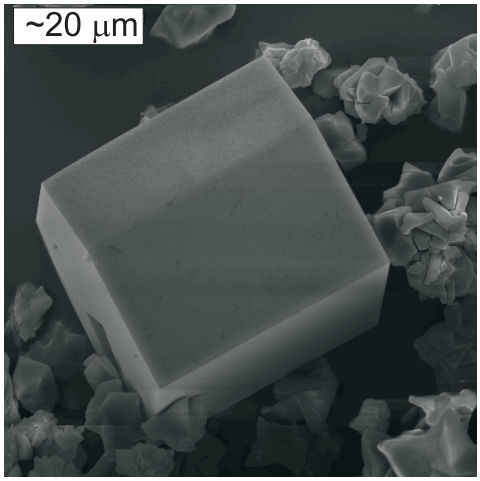

(a) 30:70 MeOH:H_2O 130 °C 21 hours

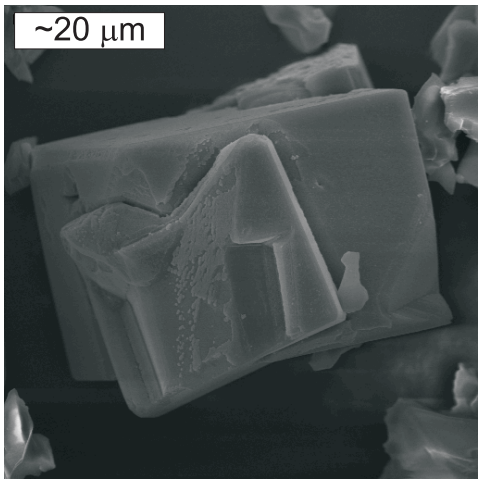

(b) 30:70 MeOH:H_2O 140 °C 21 hours

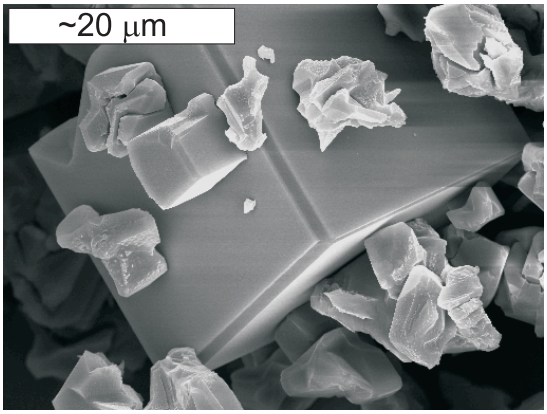

(c) 30:70 MeOH:H_2O 150 °C 21 hours

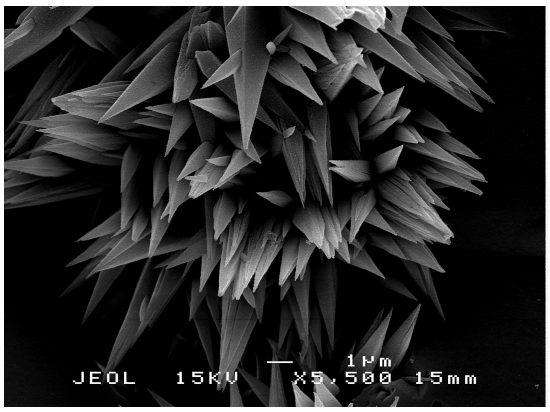

(d) 70:30 MeOH:H_2O 130 °C 21 hours

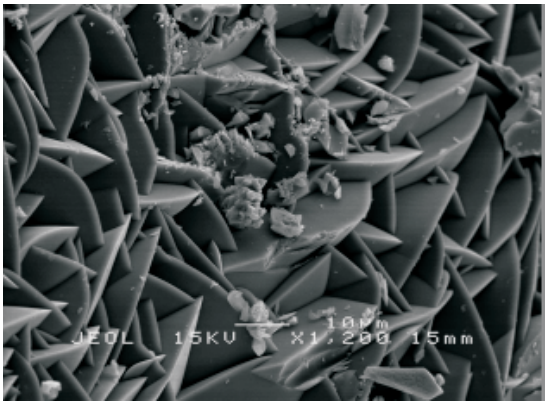

(e) 80:20 MeOH:H_2O 130 °C 21 hours

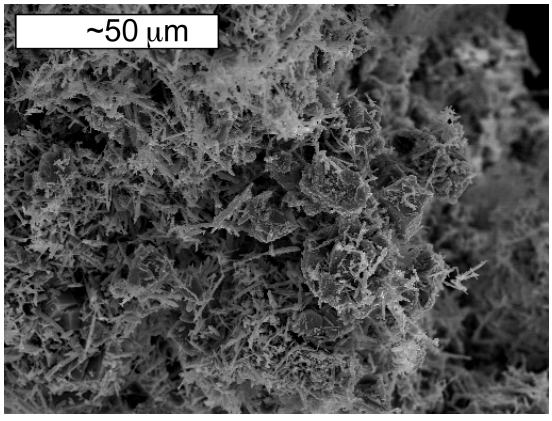

(f) 45:55 MeOH:H_2O 150 °C 21 hours

Figure 4.5: SEM images of the products of various H_2O/MeOH mixes between 130-150 °C show how higher concentrations coupled with an increase in temperature causes changes to the crystal growth. At high temperatures with high concentrations of MeOH, mottling of the pseudo cubes occurs to the formation of unwanted Fe oxy-hydroxy sulphates as shown by the occurrence of needle like structures 4.5(f). At lower temperatures, high concentrations of MeOH produce interpenetrating triangular prisms 4.5(e), though moderate concentrations of MeOH still allow for pseudo cubic crystal formation at high temperatures 4.5(c).

4.5 Hydrothermal synthesis of Fe jarosites - Oxidative method

A new hydrothermal oxidative process, similar to that used for zeolite synthesis [151], claimed to achieve 100% Fe coverage [20,63] and greater crystal size (<50 μm across a face). The technique relies on bulk dissolution of the starting materials over many days under hydrothermal synthesis conditions. For jarosites this oxidation method uses Fe wire as the bulk material [20,63]. Synthesis is under hydrothermal conditions at $\sim$ 200 °C using a saturated solution of the relevant A-site sulphate with H_2SO_4 to initiate the oxidation. This oxidation method for bulk dissolution to form jarosites [20,63] achieves crystal size of up to 0.2 mm across a face [63]. This improvement to crystal quality has enabled greater insight into the crystal structure and magnetic characteristics. The drawback is that hydronium jarosite, arguably the most important jarosite for magnetism studies, cannot be synthesised via this method [20]. This suggests that there are at least two different reaction mechanisms for jarosite formation.

Syntheses of potassium jarosite were undertaken by implementing a modified version of the literature method by Grohol *et al.* [20]. The method used 38 cm^3 capacity Pyrex pressure tubes (Ace Glass Inc) with PTFE screw tops with a Viton O-ring seated inside the tube. 0.33 g ($\pm$0.05 g) of Fe wire (2mm diameter, 99.9% purity) cut into 4-6 pieces using wire cutters were placed into each Pyrex tube. 2.44 g of K_2SO_4 were added to 25 ml of H_2O (0.56 M solution) and 1.1 ml of H_2SO_4 were added, giving a filling of $\sim$66%. The reaction was heated at 170 °C for 48 hours. The addition of the H_2SO_4 reduced the pH to < 1. A very acidic environment is needed as usual in jarosite formation but exceptionally low pHs are required for the oxidative method to oxidise the Fe wire. The remains of the iron wire were removed using a magnetic stirrer flea before washing with distilled H_2O.

This method was then extended for other iron jarosites, including: sodium jarosite, silver jarosite, ammonium jarosite and rubidium jarosite. Non-potassium jarosites are harder to synthesize and therefore the reaction has a greater sensitivity to the reaction conditions, often producing hematite. A summary of reaction conditions for the above listed jarosites synthesised using the hydrothermal oxidative method are shown in Table 4.4 below.

In comparison with K-Jarosite, formation of the other A-site jarosites was more problematic. Phase pure rubidium jarosite was not achieved; hematite, which was

Table 4.4: Syntheses conditions for non-hydronium jarosites using the oxidative technique; all reactions were carried at 170 °C for 48 hours

A-site sulphate	mass per 25cm^3 of H_2O	M	yield (g)	T_C (K) ref only
K	2.44g	0.56	0.100	63, 52
Na	0.85g	0.24	0.066	N/A
Rb	3.75g	0.56	0.049	64
NH_4	1.85g	0.56	0.697	60, (50)
Ag†	4.38g	0.56	1.67	59

† reaction preparation was carried out in the dark

always present, was decanted away during washing, its density being significantly less than that of rubidium jarosite. Silver sulphate – which is very insoluble – created a problem when retrieving the product as a large amount of reactant still remained undissolved or precipitated back out upon cooling. This could be removed by dissolving the residue silver sulphate with a large quantity of water, added to with 2-3 drops of HNO_3 acid stirred on stirrer plate. Any hematite present was decanted off during successive washes and the solid silver residue was removed with tweezers.

4.6 Synthesis of deuterated Fe jarosite samples for neutron diffraction

Large quantities of homogenous samples are required for neutron scattering experiments and two methods were employed - forced hydrolysis and oxidative which are outlined in the following sections.

4.6.1 Forced hydrolysis of deuterated jarosites - Mikasaite

Considering that ($Fe_2(SO_4)_3$) [24] (4.6) is the starting reagent for the hydrothermal forced hydrolysis reactions of hydronium jarosite and the requirement for a very high percentage of D, it was best to proceed with a high concentration of $Fe_2(SO_4)_3$ (Mikasaite). The reaction conditions for the Mikasaite based preparations were in keeping with the modified method of Earle *et al* [19], using 2 g of $Fe_2(SO_4)_3$ (Mikasaite) per 15ml of solution. The molar concentration of Fe^{3+} was increased to

0.67 M because Mikasaite is anhydrous. A summary of the reaction conditions are laid out in Table 4.5.

Mikasaite was made by the complete dehydration of $Fe_2(SO_4)_3 \cdot 5\,H_2O$. A stock of $Fe_2(SO_4)_3 \cdot n\,H_2O$ was washed with D_2O and the H_2O was removed using a rotary evaporator, the process was repeated twice more to ensure removal of H_2O in subsequent washes. Towards the end of the evaporation, a thick syrupy liquid remained, which was poured onto a large watch glass and dried in an oven (120-150 °C) to become anhydrous until a white/pink solid remains.

4.6.2 Oxidative method synthesis of deuterated jarosites

Deuterated sample preparation using the oxidative method were followed as before, but with the substitution of D_2O for H_2O and the relevant concentration of D_2SO_4 (1.1 cm^3 added per 25 cm^3 solution) was added instead of H_2SO_4.

The quantities required meant that many samples were made in a batch process and amalgamated together (Table 4.5). All the solutions were made up for the required volume for the combined number of Pyrex tubes needed in each batch. Each batch was processed together throughout the whole reaction.

Table 4.5: Synthesis conditions for deuterated jarosites using either the oxidative technique (Fe wire) or forced hydrolysis (Mikasaite). The mass shown for the Fe wire is the amount averaged between each Pyrex tube.

jarosite ID	A^+M	Fe wire (g)	Mikasaite $Fe^{3+}M$	Batch (°C)	Temp. (hrs)	time (g)	yield
D_3O_{FD}			0.675	4x25 ml	150	21	1.99
K_{FD}	0.244		0.675	2x25 ml	150	21	4.05
K_{MD}	0.56	0.333		4x25 ml	170	24	0.4
K_{MD}	0.56	0.28		7x25 ml	170	24	0.622
K_{MD}	0.56	0.333		7x25 ml	170	24	0.562
$(ND_4)_{FD}$	0.65	0.165		5x15 ml	170	24	0.079
$(ND_4)_{FD}$	0.56		0.675	3x15 ml	150	21	3.797

FD - forced hydrolysis, MD - oxidative

The yields from Mikasaite reactant show an interesting pattern: deuterium oxonium jarosite is less preferred than hydronium jarosite, yet for the non-hydronium jarosites the yield of deuterated material is greater than for the protonated analogues.

4.7 Mechanism for jarosite formation

The synthesis of jarosite by forced hydrolysis and hydrothermal oxidative synthesis are discussed below in the following subsections.

4.7.1 Hydrolysis and forced hydrolysis

In nature, jarosite formation usually starts from the dissolution of Pyrite (FeS_2) to provide a source of Fe^{2+} and SO_4^{2+} ions [38]. In low temperature regimes such as rivers and streams then the process of oxidizing Fe^{2+} to Fe^{3+} and subsequent jarosite formation happens via microbial action [16] and the action of dissolved oxygen. Chains of hydroxysulphates form around the Fe^{3+} centres producing characteristic iron flocs [42]. Jarosite precipitation occurs when the pH falls below <2 and a suitably sized cation is present [16, 140]. The chemical reactions which describe this are shown below.

$$\underset{\text{pyrite}}{FeS_2} + 3\,O_2 + 2\,H_2O \xrightarrow{\text{dissolution}} Fe^{2+} + 2\,SO_4^{2-} + 4\,H^+ \tag{4.2}$$

$$Fe^{2+} + H_2SO_4 + \tfrac{1}{2}O_2 \xrightarrow{\text{oxidation}} Fe^{3+} + SO_4^{2-} + H_2O \tag{4.3}$$

$$Fe^{3+} + 5\,H_2O + SO_4^{2-} \longrightarrow \underset{\text{jarosite precursor}}{[Fe(H_2O)_5(SO_4)]^+} \tag{4.4}$$

$$3\,[Fe(H_2O)_5(SO_4)]^+ + \tfrac{1}{2}K_2SO_4 + \tfrac{1}{2}H_2SO_4 \longrightarrow \underset{\text{jarosite}}{KFe_3(SO_4)_2(OH)_6} + 35\,H^+ + 2\,SO_4^{2-} \tag{4.5}$$

The reaction is self-generating, with continued hydrolysis reducing the pH, which in turn stabilises jarosite precursor material and further promoting jarosite precipitation.

4.7.2 Influence of pH

Control of the pH is crucial in all jarosite reactions as it determines the reaction pathway, and nucleation and subsequent crystal growth. There are two Fe^{3+} precursor species, $[Fe(H_2O)_5(OH)]^{2+}$ and $[Fe(H_2O)_5(SO_4)]^+$, the latter is the jarosite precursor [16]. A higher pH favours the former species [16, 147], whereas a lower pH, which continues to drop as further jarosite precipitation occurs, favours the latter species.

As already introduced jarosite formation proceeds via Ostwald ripening driven

by the greater thermodynamic stability of jarosites, with respect to the other iron oxy-hydroxy sulphates. This is why time is necessary to form high quality jarosite crystals. Though this only appears to work for hydronium jarosites under hydrothermal conditions as non-hydronium jarosites appear to form much more rapidly.

Non-hydronium jarosite crystals do not grow as well as hydronium jarosite crystals using the hydrothermal methods outlined in this experimental chapter, because the absorption of a counter ion, such as potassium, probably reduces the surface energy of the growing crystal by fitting into the 12 coordinate site between the T-A-T layers of the jarosite structure (Figure 4.6). This conclusion is deduced from dissolution studies where K^+ jarosites are more resistant to dissolution than H_3O^+ [15,17].

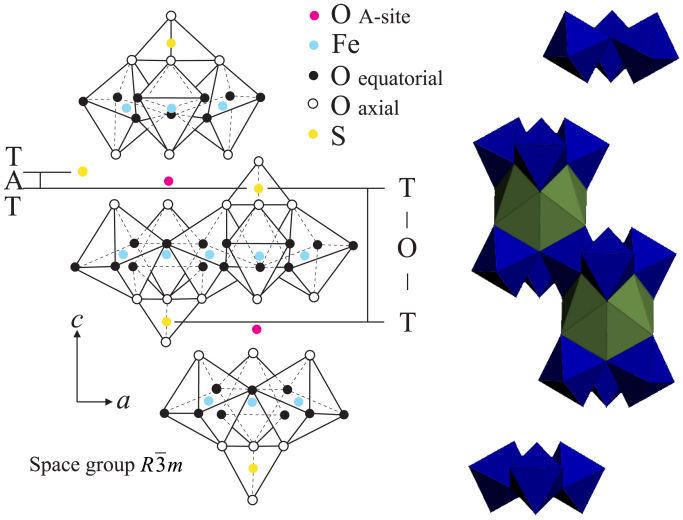

Figure 4.6: Polyhedra representation of the jarosite structure with a c axis unit cell of ~17 Å, showing the two sheets that make up of the jarosite structure. The distance between the sulphate groups across the *kagomé* plane is the T-O-T sheet. The T-A-T sheet is represented by blue (SO_4) and green (A-site) polyhedra.

4.7.3 The influence of MeOH

The introduction of methanol as a solvent appears to change the balance between kinetic and thermodynamic processes in jarosite formation. Greater concentration of MeOH initially reduces the pH of the starting reaction, however it allows for more rapid nucleation and greater quantity of nucleation sites. This means that not only will more jarosite precursor be present, but other unwanted iron oxy-hydroxy sulphates will be as well. The speed of crystal growth, increased twining (Figures 4.4(a) 4.4(b)) and greater yields all highlight the raised kinetic energies of

the reaction. Figure 4.7 shows the that high concentrations of MeOH coupled with high temperatures produce unwanted iron oxy-hydroxy phases.

Jarosite precipitation is a hydrolysis reaction, as the $[Fe(H_2O)_5(SO_4)]^+$ reacts with an appropriate A-site so more H^+ ions are released. High concentrations of MeOH appear to favour the other precursor, $[Fe(H_2O)_5(OH)]^{2+}$, which leads to the formation of iron oxy-hydroxy phases which are usually favoured at a higher pH [16].

The mechanism of forced hydrolysis [19, 140, 147] prevents extensive polymerisation of the Fe^{3+} centres, which are bridged by OH^- or H_2O units separating out the Fe^{3+} units [16]. Under low pH and forced hydrolysis conditions, the Fe^{3+} complex centres are more stable and can polymerise together to form tighter Fe^{3+} centres capped by SO_4^{2-} and bridged OH^- ions [144, 148]. This is achieved by the stability of the $[FeSO_4]^+$ complex in low pH solutions [144]. The introduction (typically) of a monovalent cation (K^+, Na^+, Ag^+ or NH_4^+) will hasten the formation of tight Fe^{3+} centres [16, 144, 148]. At higher pH levels, the Fe^{3+} centres polymerise with hydroxo-bridges [16] to form various unwanted Fe-oxy-hydroxy sulphates or Fe-oxy-hydroxides. Figure 4.8 shows how upon the addition of SO_4^{2-} and a monovalent cation, the progressive polymerisation is reduced and a jarosite precursor is produced as shown in Figure 4.8(a), before precipitation of jarosite proper (Figure 4.8(b)). During the formation of jarosite, the Fe-OH network becomes buckled with the OH^- residing slightly above and below the plane made up of the Fe^{3+} ions. This buckling is caused by the sulphate groups which are above and below the plane of Fe^{3+} ions binding to the Fe centres. This slight distortion of Fe-coordination octahedra is paramount to the magnetic properties of jarosites and thus it is very important to know how the chemistry affects the jarosite crystal structure, which is discussed in Chapter 8.

The reason for the lack of jarosite precipitation (Figure 4.7(c)) and the occurrence of unwanted phases (Figures 4.4(e) 4.4(f) 4.5(d)) at high MeOH concentrations, is the poor solvation of the H_3O^+ ion at low pH ranges of these reactions (Section 4.8.1). The absence of solvated H_3O^+ in turn reduces the ability to form a monovalent cation from which to precipitate jarosite. When the MeOH concentration reaches 90% MeOH the only product formed is a small yield of crystalline $Fe_2(SO_4)_3$, Mikasaite, which is presumed to be a reaction precursor. In the SEM images Mikasaite appears as a structure that resembles Artex (Figure 4.7(f)).

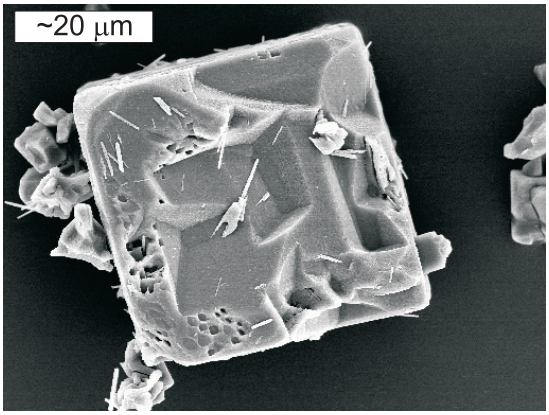

(a) 35:65 MeOH:H_2O 150 °C 21 hours

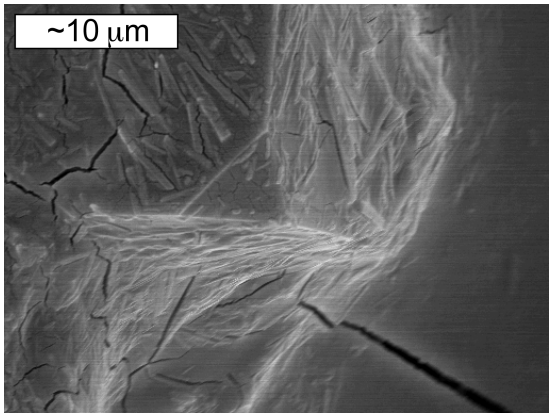

(b) 55:45 MeOH:H_2O 150 °C 21 hours

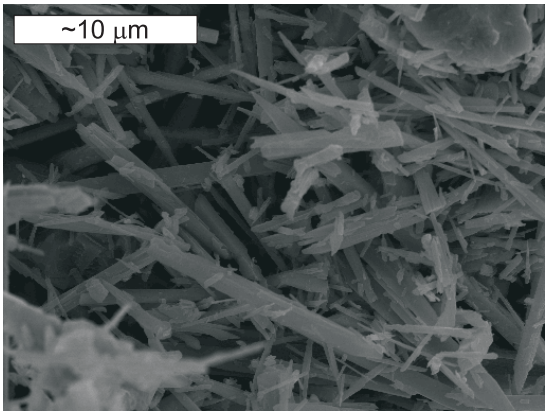

(c) 60:40 MeOH:H_2O 150 °C 21 hours

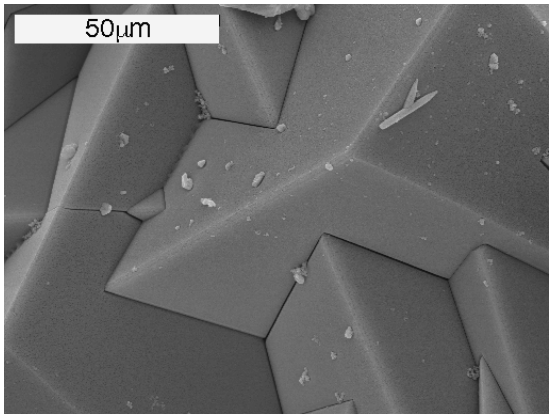

(d) 60:40 MeOH:H_2O 120 °C 21 hours

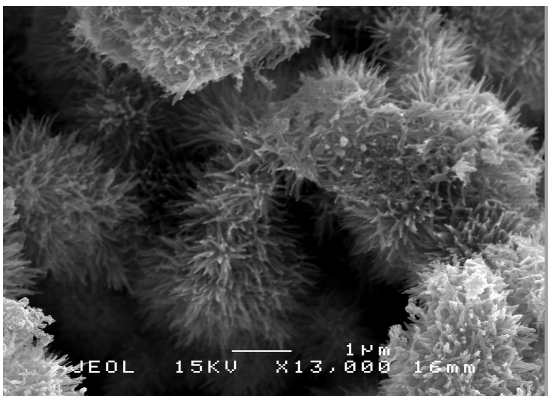

(e) Schwertmannite

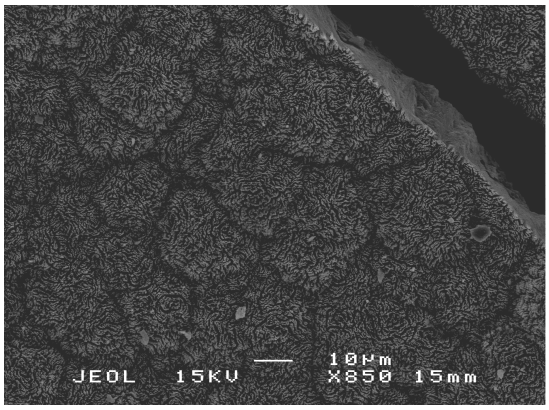

(f) 90:10 MeOH:H_2O 120 °C 21 hours

Figure 4.7: High MeOH concentrations combined with high temperatures favour the growth of other X-ray amorphous iron oxy-hydroxy sulphate phases. Figure (a) shows slight mottling and the appearance of needle-like unwanted phases. Figure (b) shows a closer view of the mottled jarosite surface and Figure (c) is an example of X-ray amorphous (1-3 broad reflections) iron oxy-hydroxy sulphates that are produced. At lower - moderate temperatures, significant interpenetration of triangular prisms are evident, leading to possible Schwertmannite formation, Figure 4.4(f). Figure (e) is an example of Schwertmannite proper. At 90% MeOH concentration the reaction fails, regardless of temperature, to produce any Fe oxyhydroxy sulphate, instead the appearance of crystalline $Fe_2(SO_4)_3$ - Mikasaite - Figure (f).

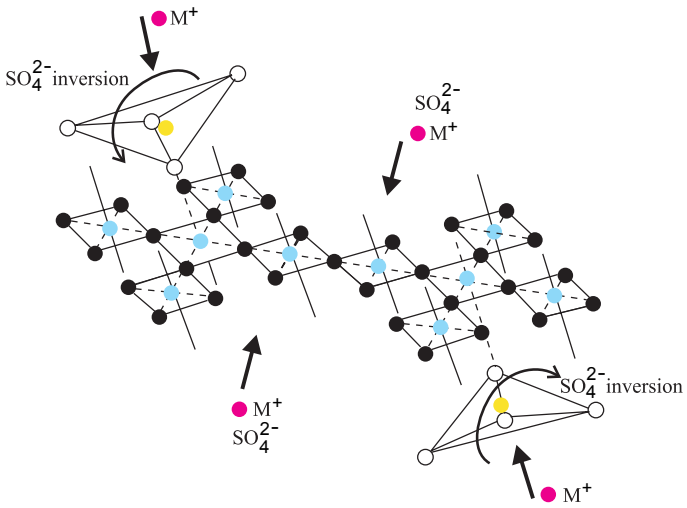

(a) Jarosite precursor

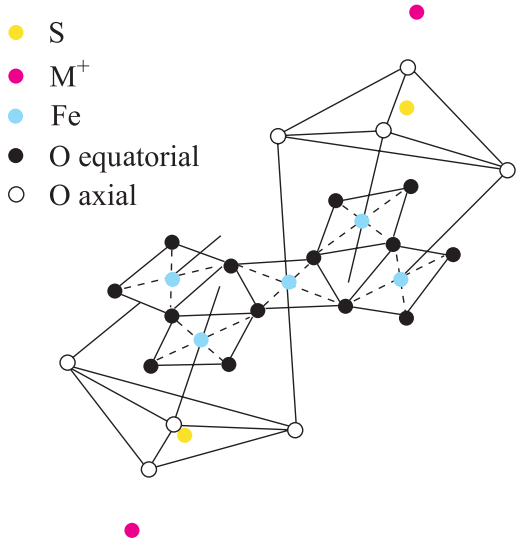

(b) Jarosite precipitation

Figure 4.8: (a) Shows the jarosite precursor and the beginning of jarosite formation with the rotation of the SO_4^{2-} unit, and with further addition of SO_4^{2-} units and A^+ cations to form jarosite (Figure (b)). The plane of the Fe-OH units becomes buckled upon jarosite formation due to the introduction of more sulphate units to complete the octahedral coordination of the central Fe^{3+}. This distortion of bond angles changes the exchange pathway between the Fe^{3+} centres, and in turn affects the resultant magnetic behaviour.

4.7.4 Oxidative formation mechanism - a potential metastable intermediate

There are several indicators as to the mechanism for jarosite formation via oxidative hydrothermal synthesis. Firstly, the residue of Fe wire that was recovered was consistently between $0.008\,\mathrm{g} - 0.02\,\mathrm{g}$ where a product formed, whether it was hematite

or jarosite. This suggests that oxidation and dissolution of the Fe wire is a separate step prior to the formation of jarosite. Further evidence of another reaction pathway was the appearance of a white solid appearing on the surface of the Fe wire. The white product could clearly be seen enveloped by jarosite precipitate that had collected at the bottom of the Pyrex tube. The visual evidence, shown in Figure 4.9, suggests that the white solid may be an intermediate involved after the oxidation of the Fe wire and prior to the jarosite formation.

Figure 4.9: Potassium jarosite formation (orange) and Szomolnokite formation (white possible intermediate phase), covering the Fe wire and dispersed among the jarosite precipitate. Use of Pyrex tubes not only allows better temperature gradients, but also allows visual inspection of the reaction. The divisions on the ruler are in millimetres

The white solid (Figure 4.9) was found to disappear upon cooling the sample to room temperature which suggests it is meta-stable. It was successfully retrieved by quenching the reaction tube from 170 °C to room temperature with cold water. The white solid was delicately scraped from the surface of the Fe wire, dried and placed on to a low background silicon plate for powder diffraction using an acetone slurry. X-ray powder diffraction data were collected from a Bruker D8 diffractometer in Bragg-Bretano geometry using Cu Kα_1 radiation, data collected using a PSD detector. The step size was $\Delta(2\theta) = 0.073°$ with a counting time of 0.6 s per $\Delta(2\theta)$ and the plate was spun at 15 rpm. The data were only good enough for pattern matching due to the high fluorescence from Fe giving rise to a raised background (Figure 4.10). The phase was identified as Szomolnokite [152], $FeSO_4 \cdot H_2O$ using the software EVA.

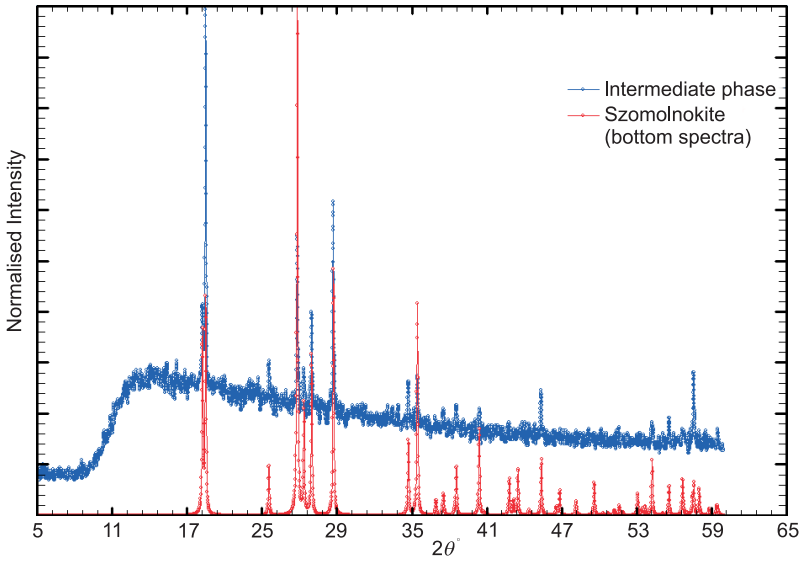

Figure 4.10: The powder data from the white potential intermediate (blue pattern) matches the powder data taken by Wildner and Giester [152] of synthetic Szomolnokite (red pattern) – $FeSO_4.H_2O$. The latter powder diffraction data, displayed in Table 4.6, were calculated using Fullprof [153] and both spectra were plotted in WinPLOTR [154].

Table 4.6: The crystallographic details for Szomolnokite. Space group is $C2/c$; lattice parameters are, $a = 7.078$ Å, $b = 7.549$ Å, $c = 7.773$ Å, $\alpha = 90°$, $\beta = 118.65°$, $\gamma = 90°$ [152].

Atom	Wykoff site	x	y	z
Fe	$4b$	0	$\frac{1}{2}$	0
S	$4e$	0	0.15307	$\frac{1}{4}$
O1	$4e$	0	0.6444	$\frac{1}{4}$
O2	$6f$	0.1697	0.0429	0.3985
O3	$6f$	0.0956	0.2683	0.1560
H	$6f$	0.108	0.709	0.315

4.8 Analysis of the synthesis methods and comparison with natural samples

This section briefly discusses the merits of forced hydrolysis and oxidative synthesis and finally makes a comparison with naturally occurring samples.

4.8.1 Forced hydrolysis versus oxidative

The presence of Szomolnokite, $Fe(SO_4).H_2O$, as a likely intermediate indicates that the reaction mechanism for the oxidative method can be pieced together and compared with jarosite formation under forced hydrolysis conditions. Another key component to the oxidative reaction is that jarosite does not precipitate from Szomolnokite without the presence of a non-hydronium A-site cation. It was noted that, during the oxidative reactions hydrogen gas was liberated and detected by the ignition of the gas produced. Using this information together with the observation of Szomolnokite as a likely intermediate and the failure of the method for hydronium jarosite allows us to propose the following,

$$\mathrm{Fe} + \mathrm{H_2SO_4} + \tfrac{1}{2}\mathrm{O_2} + \mathrm{H_2O} \longrightarrow \mathrm{Fe(SO_4)} \cdot \mathrm{H_2O} + \mathrm{H_2O} \tag{4.6}$$

$$6\,\mathrm{Fe(SO_4)} \cdot \mathrm{H_2O} + \mathrm{K_2SO_4} + 6\,\mathrm{H_2O} \longrightarrow 2\,\mathrm{KFe_3(SO_4)_2(OH)_6} + 3\,\mathrm{H_2} + 3\,\mathrm{H_2SO_4} \tag{4.7}$$

Thus, it appears there is a completely different reaction pathway, one that does not allow for the formation of hydronium jarosite. Hydronium jarosite is instead believed to progress via a solvated $[FeSO_4]^+$ complex [144]. It is the absence of this species in the above mechanism that prevents hydronium jarosite from being formed.

The role of Szomolnokite as an intermediate can be understood from the similarity in crystal structures of the two iron sulphate derivatives (Figure 4.11). The Fe-O(S) distance within potassium jarosite is 2.076 Å, only slightly longer than in Szomolnokite, at 2.053 Å. The Fe-O(H) distance, bridging the Fe centres in jarosite, is about 1.9806 Å, in Szomolnokite the Fe-O(H_2) distance is much longer at 2.228 Å. Oxidation of the Fe^{2+} to Fe^{3+} hydrolyses the H_2O molecules and draws the OH units closer to the Fe^{3+} centres to allow bridging and subsequent formation of the Fe^{3+} octahedrons that make up the *kagomé* plane.

Further minimal Fe vacancies are expected from the oxidative synthesis method because the charge neutrality of the Szomolnokite intermediate reduces the need for

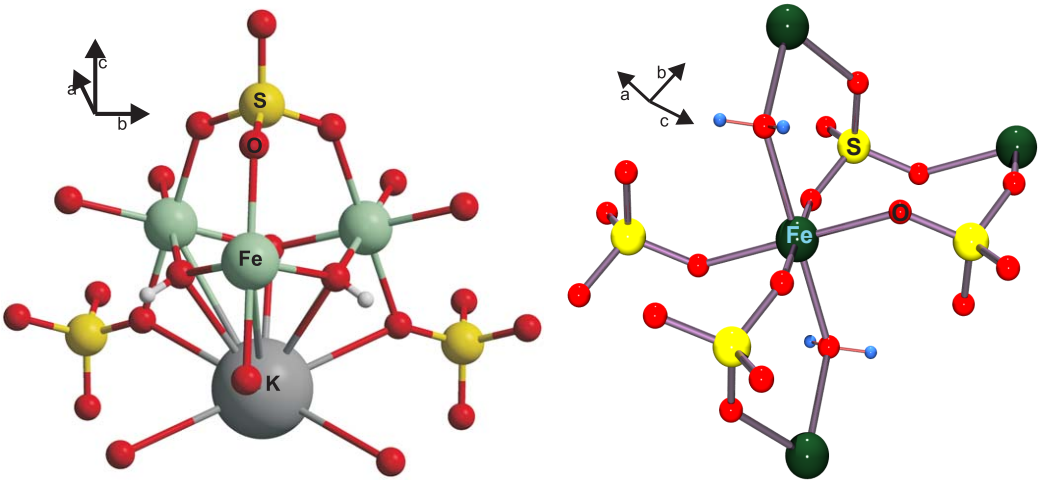

(a) K jarosite crystal structure (b) Crystal structure of Szomolnokite

Figure 4.11: Structural representation of the jarosite structure. The sulphate groups cap above and below the Fe octahedra sitting along the 3-fold axis. Each of these subunits is separated by the A-site, K^+, in the diagram. (b) Szomolnokite has a more open structure; the distortion from rhombohedral is only slight: $\beta \sim 120°$ and the a and b lattice parameters are similar to the a parameter in jarosite. Refer to Table 4.6 for Szomolnokite crystallographic details.

charge compensation and any associated Fe vacancies or H_2O inclusion. Formation of the jarosite can only be completed when the appropriate A-site sulphate reacts. It is therefore the high Fe^{2+} occupation of Szomolnokite that keeps to a minimum the nonstoichiometry of the resultant phase. Oxidation from Fe^{2+} to Fe^{3+} is very rapid and the associated incorporation of the A-site cation will almost be simultaneous ensuring an almost ideal stoichiometry.

The addition of MeOH as a solvent highlighted many factors underlying forced hydrolysis conditions. It was found to speed up the rate of formation of jarosite and increase yields beyond those obtainable for any reaction using 100% H_2O as the solvent. The lower yields for hydronium jarosite, when compared to other A-site ions, is then related to the hydration number for A-site cations. The hydration number, h, for K^+, Na^+, Rb^+ and NH_4^+ in solution are; $h = 1.8 \pm 0.5$, 3.9 ± 0.5, 1.8 ± 0.3 and 1.8 ± 0.5 respectively [155], is significantly lower than H_3O^+, $h = 6.7 \pm 0.7$ (H^+) [155]. MeOH for comparison has $h = 1 \pm 0.3$ [155] and therefore acts to lower the hydration of the H_3O^+ ions in solution.

The dependence of hydronium jarosite precipitation on solvated H_3O^+ is shown below [155]:

$$3\,Fe_2(SO_4)_3 + \underbrace{2\,[\,H_3O(H_2O)_6]^+}_{\text{solvated } (H_3O)^+ \text{ complex}} \longrightarrow 2\,[\,(H_3O)Fe_3(SO_4)_2(OH)_6] + 5\,H_2SO_4 + 2\,H^+ \tag{4.8}$$

4.8.2 Natural jarosites

Jarosites were synthesised in the belief that better quality jarosites could be produced in the laboratory compared to those found in nature [3,7,18] and to understand the formation process so that it can be improved upon [2]. The problems of natural jarosite formation are the inclusion of other elements, to produce similar jarosite related minerals (eg beaverite and dorallcharite) containing a mixture of B-site metal ions (Cu^{2+}, Pb^{2+}, Al^{3+} or Tl^{+}) [3, 13] and substitution of the sulphate group for arsenate or chromate groups [4,6,7]. Naturally occurring hydronium jarosite is very rare [3] because jarosites are commonly a product of weathering and low temperature process ($< 100°C$) whereas hydronium jarosite formation requires forced hydrolysis conditions because of the high solvation number, h.

Without readily accessible stoichiometric pure single A-site natural jarosites, especially hydronium jarosite, the understanding of the chemistry and the related magnetism requires the synthesis of jarosites. Tables 4.1, 4.2 and 4.3 show that differing synthesis conditions have a profound effect on the magnetism. There is a tolerance between cation and H_3O^+ ion competing for the A-site before this has an effect on the magnetic transition temperatures for the non-hydronium jarosites. Therefore to investigate the role of the A-site within the non-hydronium jarosites, it is not critical to have an A-site with a stoichiometric pure cation. Similarly is it only through synthesising hydronium jarosites that it is possible to achieve the range of values for T_g.

What is clear, certainly considering the non-hydronium jarosites, is that 100% Fe coverage is not critical either, because the transition temperatures are similar for a given high occupation of an A-site, immaterial of synthesis method and the natural sample. The effect of Fe percentage coverage within the hydronium jarosites is unknown from these results as it is assumed 100% H_3O^+ inclusion in the A-site, yet there is a wide variation in T_g.

Chapter 5

Magnetic Measurements

The magnetic properties for all the samples made were characterised using the two SQUIDs as outlined in Chapter 3. The important magnetic characteristics were determined from susceptibility zero-field cooled and field cooled temperature sweeps from $\sim 2\,\mathrm{K}$ up to 310 K, usually in a measuring field of 100 Oe. Measurements were taken at temperature steps of 0.5 K or 0.25 K through the transition region, a range of 10 - 20 K. Larger steps, 10 - 20 K, are sufficient for Curie-Weiss determination in the paramagnetic temperature region. The sample temperature was increased to the point before the straw became soft (usually 310 K) to obtain the best possible Curie-Weiss fit to the data. After the final measurement the sample was cooled back down to the base temperature with the same applied field. The sequence of measurements was repeated after thermal equilibrium had been reached.

These measurements provide the Néel temperature, T_{N}, or spin-glass freezing temperature, T_{g} and the Curie-Weiss temperature, θ_{W}. Data were collected from the majority of Fe jarosite samples synthesised and all the relevant samples with their transition temperature(s) and θ_{W} are displayed in Table 5.1. Other values such as J, the exchange interaction, C, the Curie constant, and μ_{eff}, the effective moment, are not listed and this is discussed later in the chapter.

5.1 Susceptibility measurements

The Néel temperatures given in Table 5.1 are taken from the maximum in the susceptibility, χ, which marks the onset of Néel ordering. The temperature dependence of the susceptibility for KFe D2O in Figure 5.1(a) shows two clear transitions, T_{N_1} and T_{N_2}, and their values were determined from the maxima using the derivative

Table 5.1: Table of spin glass (T_g), ordering (T_C) temperatures and Cuire-Weiss temperatures for the Fe jarosite samples detailed in Chapter 4.

Sample	T_g (K) (±0.2 K)	θ_W (K) (±100 K)
H3OFeS1	15.7	−1490
H3OFeS2	15.4	−1505
H3OFeS3	14.8	−1415
H3OFeS4	13.9	−1400
H3OFeS9	18.8	−1565
H3OFeS10	18.4	−1530
H3OFeS11	17.2	−1360
H3OFeS12	15.8	−1420
H3OFeS13	14.8	−1580
H3OFeS14	12.7	−1315
H3OFeS15	12.1	−1310
H3OFeS16	11.3	−1195
H3OFeS17	14.8	−1415
H3OFeS18	14.5	−1460
H3OFeS21	17.4	−1490
H3OFeS22	16.6	−1595
H3OFeS23_b	16.2	−1635
H3OFeS24	14.1	−1480
H3OFeS25	13.1	−1520
H3OFeS26	12.0	−1355
H3OFeS27	11.6	−1285
H3OFeS28	10.9	−1305
H3OFeS30	14.2	−1670
H3OFeS31	15.1	−1560
H3OFeS32	14.4	−1680
H3OFeS33	13.7	−1475
H3OFeS34	13.9	−1440
H3OFeS35	12.3	−1555
H3OFeS36	11.5	−1500
H3OFeS37	10.9	−1750

Sample	T_g (K) (±0.2 K)	θ_W (K) (±100 K)
H3OFe031	19.7	−1485
H3OFe033	18.7	−1330
H3OFe044	18.0	−1465
H3OFe029	17.7	−1420
H3OFe042	16.9	−1410
H3OFe048	16.6	−1470
H3OFe030	16.3	−1475
H3OFe047	16.8	−1725
H3OFe049	15.8	−1510
H3OFe024	15.6	−1400
H3OFe024b	16.0	−1600
H3OFe016	15.8	−1580
H3OFe027	15.7	−1530

Sample	T_C (K) (±0.2 K)	θ_W (K) (±100 K)
KFe1	64.5, 45.0	−1240
KFe3	64.2	−1360
KFe4	(64.2), 50.3	−1400
KFe5	63.6, 47.0	−1300
KFe6	47.3	−1340
KFe natural	63.3, 50.3	−1460
KFe D2O	64.4, 50.1	−1340
KFeMIT10	62.5, 53.8	−1640
NaFe1	(60.8), 43.9	−1460
NaFe2	(61.0), 43.0	−1600
NaFe3	(60.0), 39.5	−1750
AgFe3	44.3	(−4000)
AgMIT	59.4	(−4000)
RbFe1	63.9, (50.0)	−1640
RbFe2	64.2, 50.7	−1650
RbFe3	45.0	−1520
NH4Fe1	61.4, 50.1	−1660
NH4Fe2	43.1	−850
NH4Fe3	61.3, 50.5	−1560

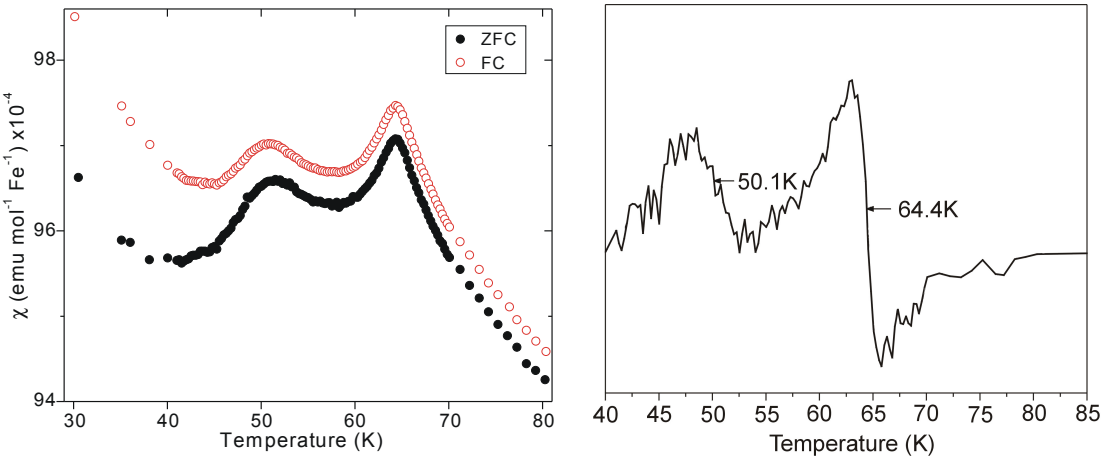

(a) Molar susceptibility plot for deuterated potassium jarosite (KFe D2O) shown between 30 to 85 K. Two clear transitions are visible at $T_{N_1} \sim 65\,\mathrm{K}$ and $T_{N_2} \sim 50\,\mathrm{K}$

(b) Derivative of the field cooled magnetic susceptibility of (KFe D2O) highlighting the two transitions, T_{N_1} and T_{N_2}.

Figure 5.1: Susceptibility measurement results for the deuterated KFe jarosite sample (KFe D2O). The two figures clearly show there are two transitions. The first transition $T_{N_1} \sim 64\,\mathrm{K}$ is sharp and strong with a broader second transition, $T_{N_2} \sim 50\,\mathrm{K}$.

$\mathrm{d}\chi_{FC}/\mathrm{d}T$, shown in Figures 5.1(a) and 5.1(b).

Table 5.1 lists magnetic data taken from many non-hydronium samples. Most display two transitions, though there is a change from two clearly visible transitions to a single broad transition at a lower temperature when the concentrations of the relevant A-site sulphate or hydroxide at the start of each synthesis are low. Under such conditions there will be a greater uptake of hydronium within the structure that causes only one broad transition to be observed, as exemplified in Figure 5.2.

Values of spin glass freezing temperature, T_g, were determined from gradient changes in the FC run at the separation of the ZFC/FC plots. This was further checked by referring to the derivative of $\mathrm{d}\chi_{FC}/\mathrm{d}T$. Five examples of the temperature dependence of χ and χ^{-1} for hydronium jarosites with a spread of values for T_g are shown in Figure 5.3 with an insert zooming in on the ZFC/FC separation.

Samples with higher values of T_g (Figure 5.3) show a greater separation between the ZFC/FC below T_g than samples with much lower values of T_g. All samples show a Curie tail, possibly indicative of superparamagnetism, and an increasing χ at very low temperatures, though it is more pronounced for samples with the lowest values of T_g. It is significant that T_g appears to become enhanced with increasing applied field (Figure 5.3(c)). This behaviour, predicted for a *kagomé* antiferromagnet with small XY anisotropy [84], contrasts with that expected for conventional spin glasses

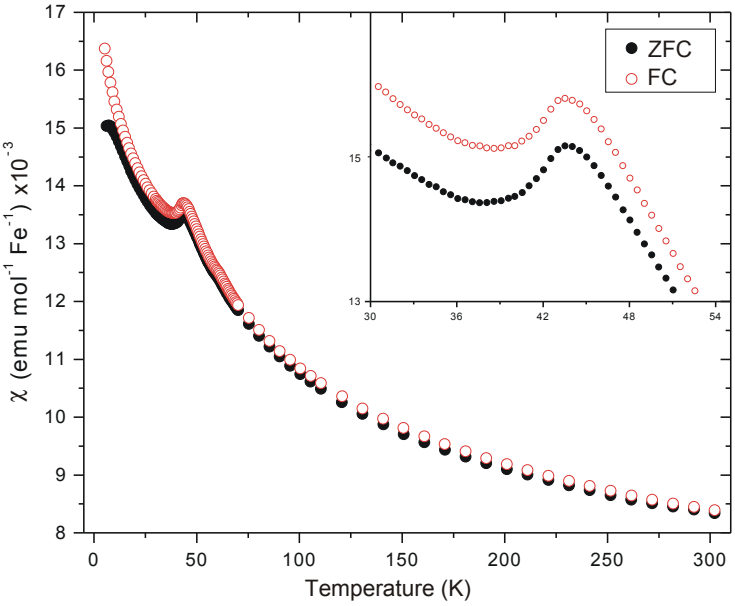

Figure 5.2: Temperature dependence of susceptibility for sample NH4Fe2 with an insert enlarged around the transition temperature. Like many syntheses where the A-site cation concentration is reduced, increase in hydronium uptake occurs. This has the effect of removing the noticeable double transition leaving one broader transition lower in temperature.

where it is suppressed [54, 75].

θ_W values were obtained from an extrapolated linear fit of the high temperature regime of the FC $\chi^{-1}(T)$ data to the intercept on the x axis, shown in Figure 5.4. The extrapolation involved high temperature data, typically in the range 150 K $< T <$ 310 K, as in this regime the inverse susceptibility is the most linear. There is, however, still curvature in this regime that evidences spin-spin correlations and makes the values of θ_W difficult to determine. This behaviour also explains the wide spread of values for θ_W and the Curie constant in the literature [18,20,21,36,37,156].

Similarly, it is difficult to determine the effective moment as the samples never reached saturation within the temperatures ranges of the SQUID measurements as shown in Figure 5.5: the calculated spin only value for a Fe^{3+} ions is 5.92 μ_B.

5.1.1 Discussion of susceptibility results

The results clearly show a relationship between synthesis conditions and their magnetic properties. The hydronium jarosites demonstrate this best of all the Fe jarosites as a larger range of samples could be synthesised with different transition temperatures. Increasing MeOH concentration produced samples with spin-glass

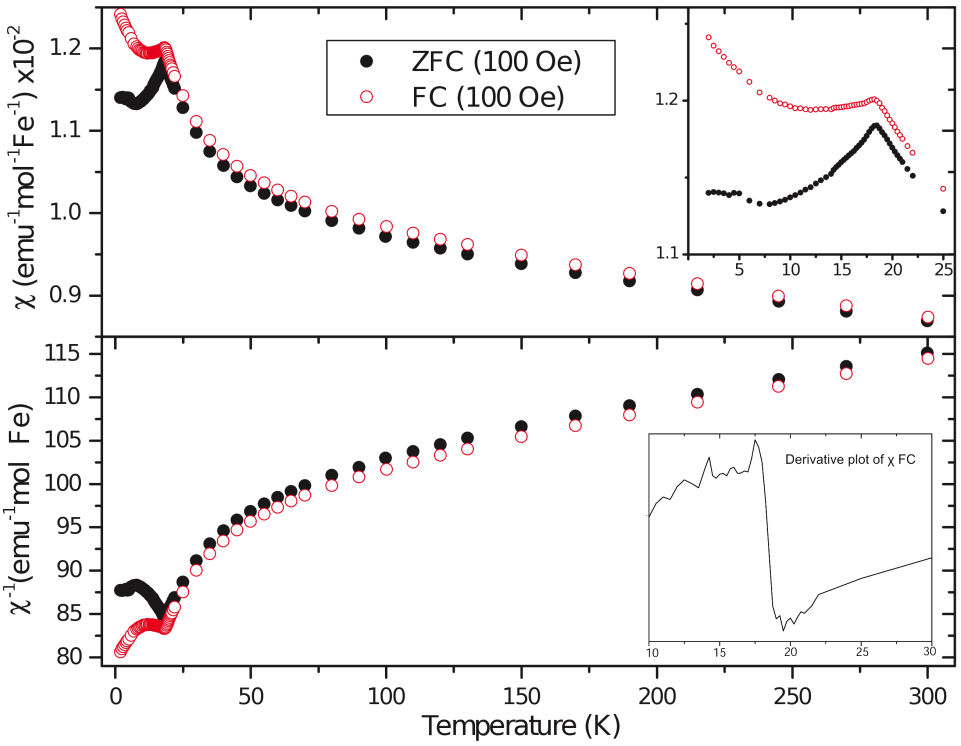

(a) Plots of $\chi(T)$ and $\chi^{-1}(T)$ taken under ZFC and FC conditions in measuring fields of 100 Oe for H3OFeS10. $T_g = 18.4\,\mathrm{K}$, $\theta_W = -1530\,\mathrm{K}$

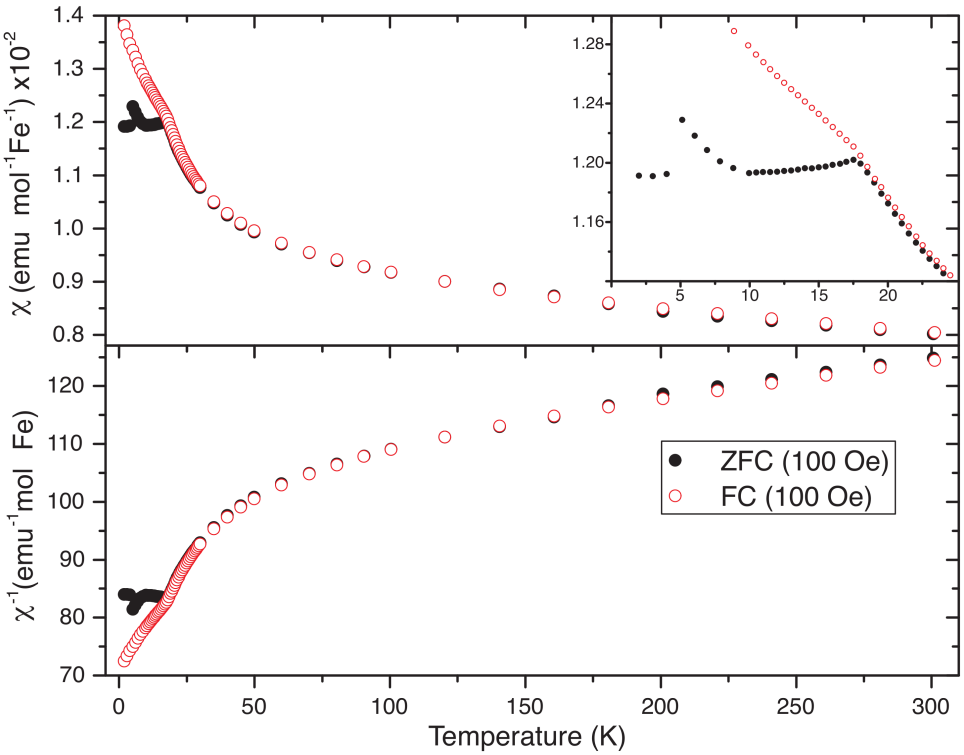

(b) Plots of $\chi(T)$ and $\chi^{-1}(T)$ taken under ZFC and FC conditions in measuring fields of 100 Oe for H3OFe029. $T_g = 17.7\,\mathrm{K}$, $\theta_W = -1420\,\mathrm{K}$

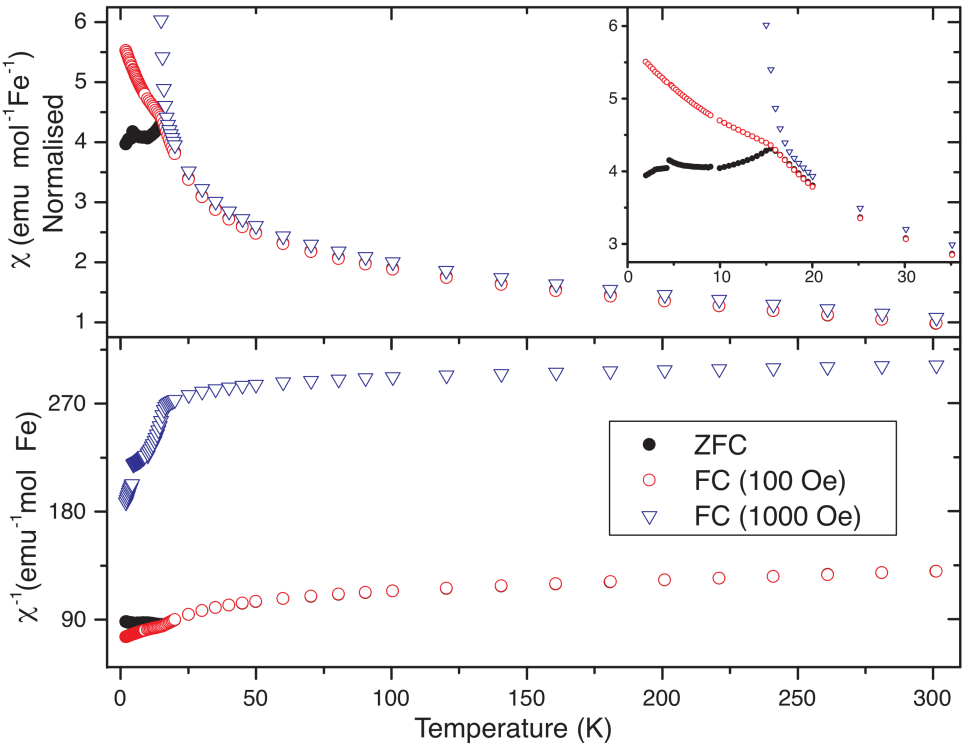

(c) Plots of $\chi(T)$ and $\chi^{-1}(T)$ taken under ZFC and FC conditions in measuring fields of 100 Oe and 1000 Oe ($\triangledown$) for H3OFe024. $T_g = 15.6\,\mathrm{K}$, $\theta_W = -1400\,\mathrm{K}$, $C = 13.0 \pm 1\,\mathrm{emu\,K\,mol^{-1}}$

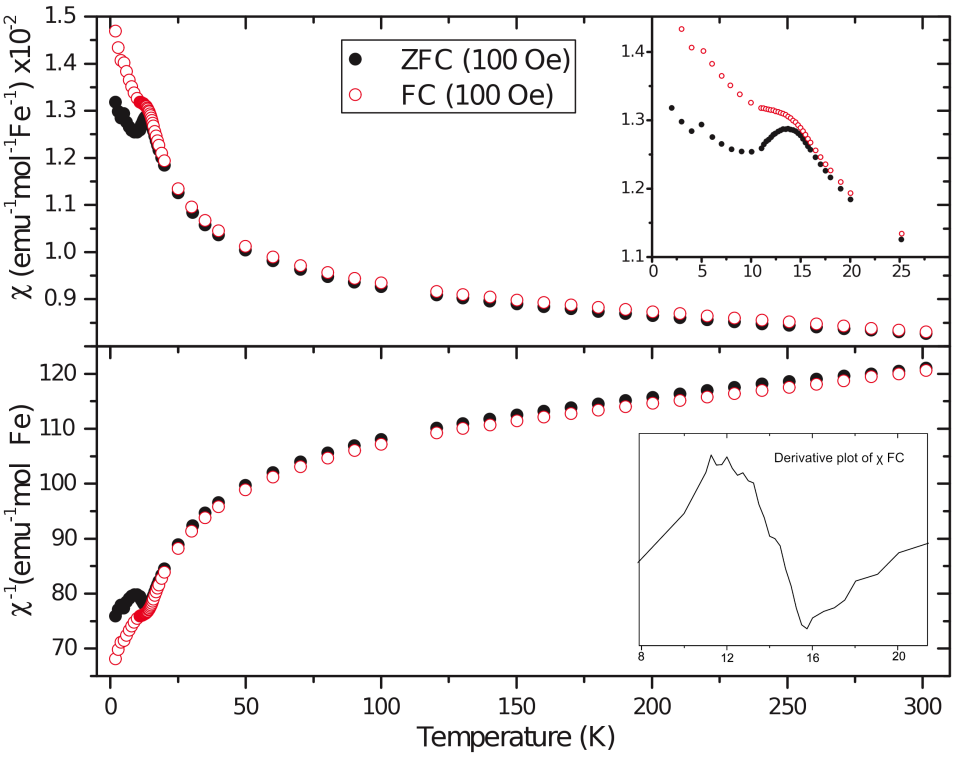

(d) Plots of $\chi(T)$ and $\chi^{-1}(T)$ taken under ZFC and FC conditions in measuring fields of 100 Oe for H3OFeS33. $T_g = 13.7\,\mathrm{K}$, $\theta_W = -1475\,\mathrm{K}$

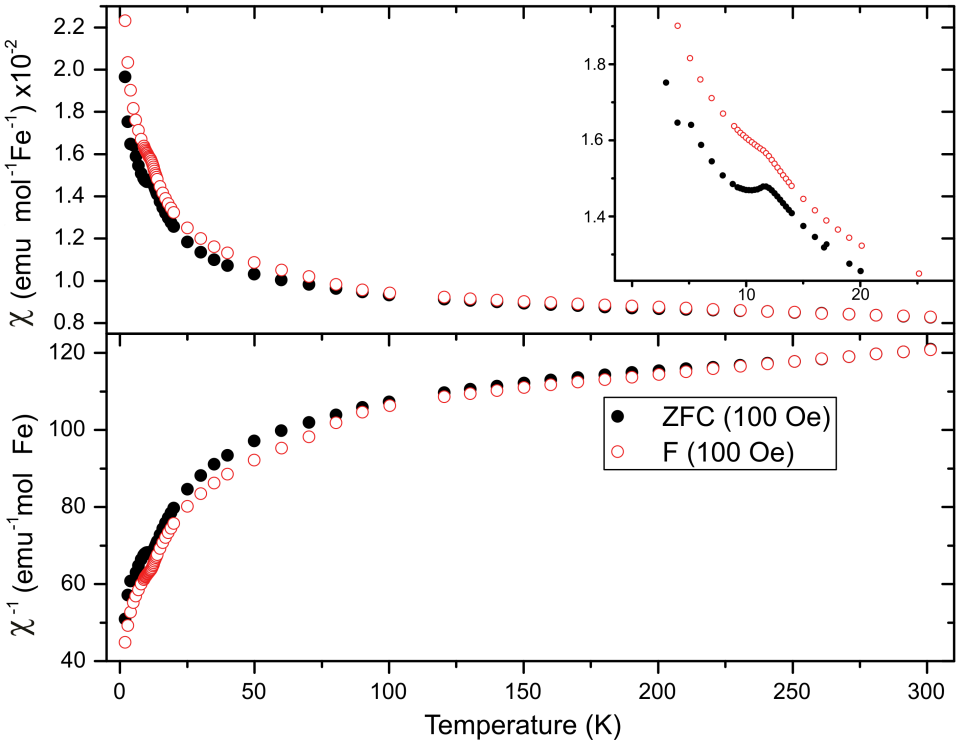

(e) Plots of $\chi(T)$ and $\chi^{-1}(T)$ taken under ZFC and FC conditions in measuring fields of 100 Oe for H3OFeS36. $T_g = 11.5\,\mathrm{K}$, $\theta_W = -1500\,\mathrm{K}$

Figure 5.3: The upper plots in the graphs are the molar susceptibility with an insert zooming on the separation in the ZFC (●) / FC (○) temperature sweeps. The lower plot of $\chi^{-1}(T)$ is used to obtain θ_W and plots for H3OFeS10 and H3OFeS33 contain inserts showing the derivative of the FC sweep zooming on the transition temperature. There was a FC temperature sweep undertaken at 1000 Oe for H3OFe24, which shows the separation for the FC at 1000 Oe beginning at a higher temperature.

freezing temperatures below the lowest temperatures achieved using only 100% H_2O as a solvent.

Hydronium jarosites do not display a plateau in the FC data below T_g. Instead the FC magnetisation increases [36] at low temperatures; this is also apparent in the ZFC data below T_g. This increase is greatest for those samples with much lower values of T_gs (Figure 5.3(e)). It has been suggested that this could be due to superparamagnetism associated with the dilution of the magnetic sites [36,157], but it could be due to the presence of unwanted Fe hydroxy-sulphates as discussed in Section 4.4.

In contrast, many non-hydronium jarosite samples show two distinct transitions. The prominent transition, T_{N_1}, is the antiferromagnetic ordering transition of the moments into 120° order with the chirality $\kappa = +1$ [21]. The weaker transition,

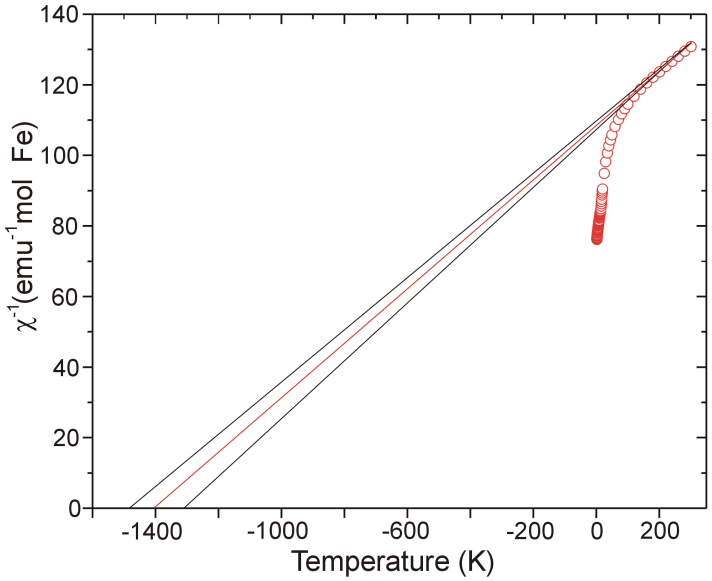

Figure 5.4: An extrapolated inverse susceptibility plot for hydronium jarosite sample H3OFe24, $C = 13.0 \pm 1.0\,\mathrm{emu\,K\,mol^{-1}}$. This plot gives a good representation of θ_W values for all Fe jarosites. The extrapolation was a linear regression fit (red line) from where the curvature of the plot was minimal. Either side show two extrapolations by eye to give an estimated error. The error is high; nonetheless, it shows how large the θ_W values are for Fe jarosites.

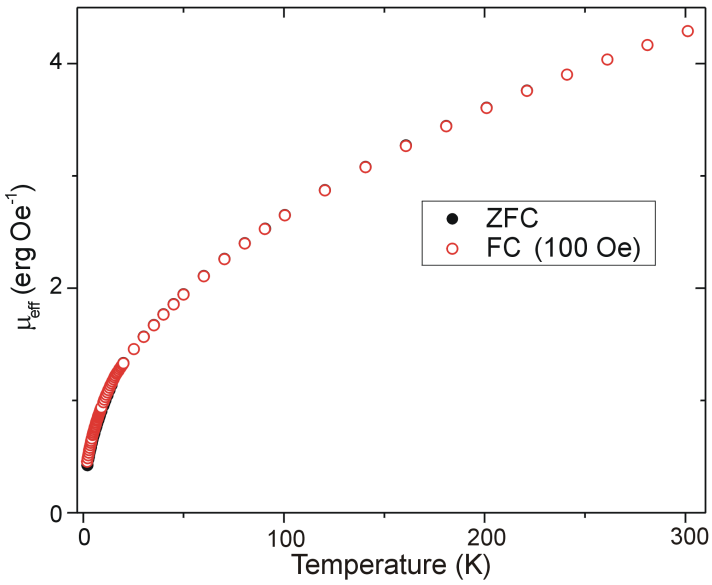

Figure 5.5: Plot of the effective magnetic moment against temperature for sample H3OFe24 ($T_g = 15.7\,\mathrm{K}$). Similar for all jarosites, the effective moment does not saturate within the temperature range accessible for the setup on the SQUIDs used. The sample is far from reaching saturation at 310 K and gives strong evidence that correlations within the magnetic system exist far and above the relevant transition temperature.

T_{N_2} is where the moments fall into the plane [21]. T_{N_2} is sometimes absent or T_{N_1} becomes broad with no visible second transition when the hydronium content of the A-site is increased as shown in Figure 5.2.

Harris *et al.* [91] determined the mean field theory equation for θ_W (5.1) from which J can be determined:

$$\theta_W = \frac{3}{2}\left[\frac{zJS(S+1)}{3k_B}\right] \tag{5.1}$$

where z is the number of neighbouring spins; $z = 4$ for the *kagomé* lattice.

Taking sample H3OFe24 as an example, with $\theta_W = -1400\,K$ a value for the exchange integral of $J \sim 55\,cm^{-1}$ can be determined. This value is high when compared to literature results [65] suggesting that the spin-spin correlations at high temperature make estimation of J difficult.

The values for θ_W give a reasonable value for T_g for a *kagomé* antiferromagnet in the XY limit, predicted by a reduced T_{KT}, Kosterlitz-Thouless transition temperature, $T_{KT} \approx \theta_W/48$ [84]. A θ_W value of $-1400\,K$ gives a reduced $T_{KT} = 29.2\,K$, in fair agreement with the values for T_g obtained in this project. In this theoretical work the transition corresponds to a binding of vortices that is raised to higher temperature by increased XY anisotropy or applied field [84]. This possibility is shown in Figure 5.3(c).

5.2 Hysteresis measurements

Hysteresis measurements are used to observe the presence of remanent magnetisation. The remanent magnetisation for a spin-glass is the result of spins becoming pinned in a certain direction due to local anisotropy, and an energy cost to reorient these spins in a changing field direction [75]. The spin orientation within a traditional spin glass below T_g is expected to be isotropic and separate from the crystal lattice as the spin direction on a macroscopic level is essentially disordered [75].

Different anisotropies are possible and these will have a different effect on the hysteresis loops explained in Section 3.4. The Dzyaloshinskii-Moriya interaction ("DMI") will favour a unidirectional alignment of spins and therefore a $\theta = \pi$ rotation of spins will result in a displacement hysteresis – a shift along the x-axis – after cooling in a large field [75].

The other anisotropy considered is uniaxial anisotropy, caused by crystal field effects [75]. An uniaxial anisotropy will induce a loop in the hysteresis and the width

is determined by the strength of the anisotropy [75]. A traditional spin glass will show a mixture of both uniaxial and unidirectional anisotropies.

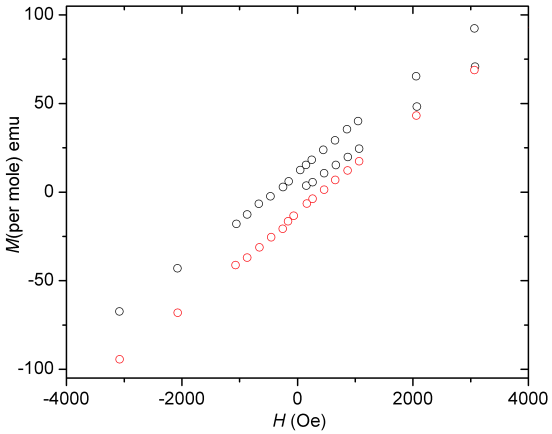

(a) Standard hysteresis measurement in high field (±7 T) taken at 10 K for sample H3OFeS10, displaying the small presence of coercivity.

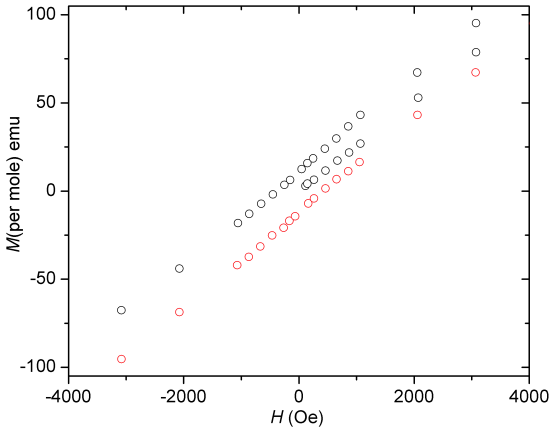

(b) Displacement hysteresis measurement in high field (±7 T) taken at 10 K for sample H3OFeS10, displaying the small presence of coercivity. The sample was first field cooled in high field from 100 K.

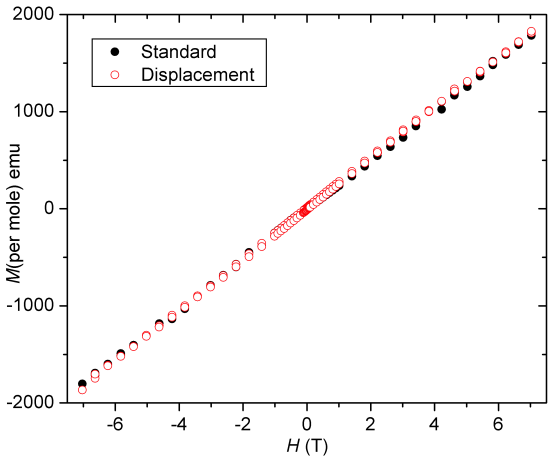

(c) Both hysteresis measurements overlaid showing they both trace the same path with no displacement along the y axis.

Figure 5.6: Hysteresis plots (a), (b) and (c) for sample H3OFeS10 in high field (±7 T) taken at 10 K. Plots (a) shows a standard hysteresis measurement focusing between small fields highlighting the slightest coercivity and similarly again in plot (b), where the sample was first field cooled from 100 K in high field. The black circles represent the initial sweep, the red circles show the return sweep. The circle diameters are a good approximation for the error bars. Plots (a) and (b) are overlaid in (c) showing that there was no displacement in magnetisation as a result of field cooling. The coercivity displayed though slight, is centred around the origin with no displacement along the x axis demonstrating minimal unidirectional anisotropy (DMI), suggesting only unidirectional anisotropy is present.

The standard hysteresis data of a typical sample of hydronium jarosite (H3OFeS10) are shown in Figure 5.6(a). Taken between fields of ±7 T, they show coercivity. Cooling in a field of T before taking the hysteresis data is found to have no effect (Figures 5.6(b) and 5.6(c)). The absence of displacement of the curve along the x-axis indicates that the DMI, if present, is small and that anisotropy from crystal field effects are more likely.

Another hysteresis measurement method involved generating positive sub-loops on a virgin curve as described in Figure 5.7. Data were taken from samples H3OFe024, H3OFe024b, H3OFeS10, H3OFeS30 and H3OFeS27.

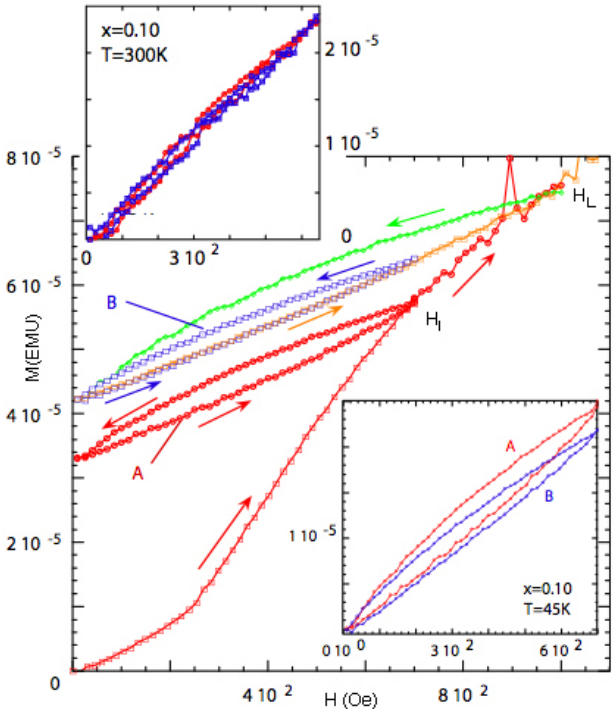

Figure 5.7: Subloops data are taken when the field is reduced to zero and then back to the virgin curve, which can be used to explore the build up of spin-spin correlations. The method was developed to study the correlations in the high temperature superconductor $La_{2-x}Sr_xCuO_4$ [113] and example data are presented above. The subloops are expected to be congruent and to have the form in the absence of correlations. Ideally, the data for a given subloop should be repeated before the field is increased to another point on the virgin curve.

No change in the form of the loops was observed in low fields, changes could, however, be observed in larger fields. Examples of data taken for H3OFe24b taken at 5 K are given in Figure 5.8. Data were taken as quickly as possible to minimise relaxation effects. There are several interesting features from the plots. Figure 5.8(b) shows there is a jump in the magnetisation for loop ● near ∼ 1.5 T, which is not

repeated in loop ○. Jumps in magnetisation suggest the system is able to both change ground states and overcome anisotropic energy barriers.

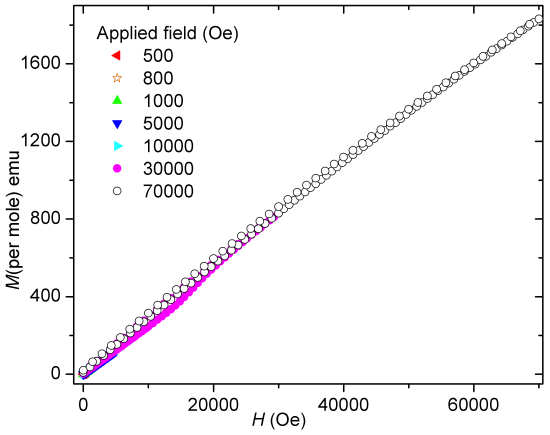

(a) Positive hysteresis loops up to high field (±7 T) taken at 5 K for sample H3OFe024b.

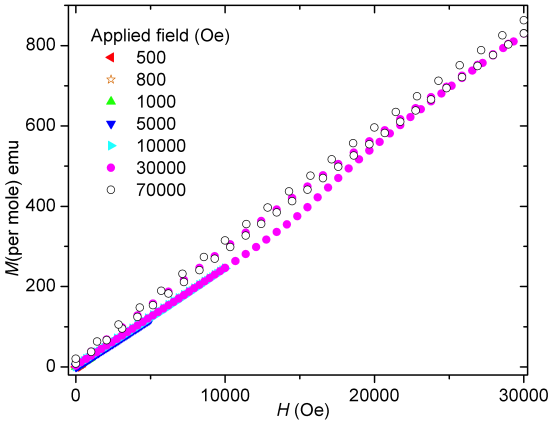

(b) Positive hysteresis loops focusing between 0 and 3 T H. Separation between the loops becomes apparent.

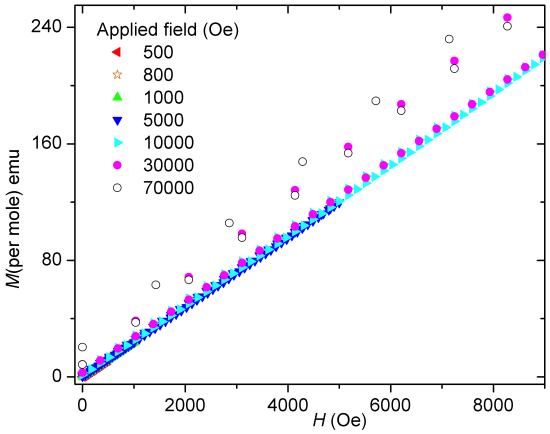

(c) Positive hysteresis loops focusing between 0 and 9000 Oe H. Displacement along the y axis occurs with increasing applied field of the loops.

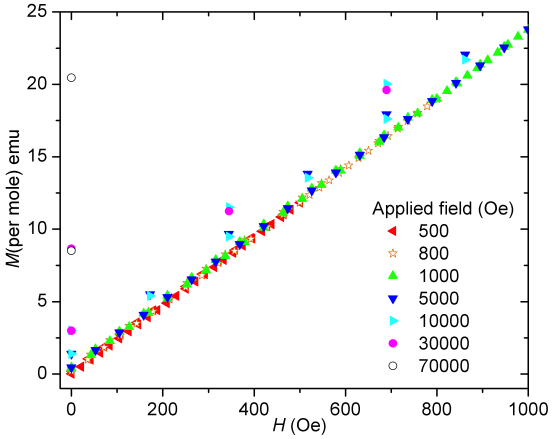

(d) Positive hysteresis loops focusing between 0 and 1000 Oe H. There is evidence of a time dependent nature of the magnetisation as the emergence of ageing between the loops taken in high fields.

Figure 5.8: Positive hysteresis loops up to high field (±7 T) taken at 5 K for sample H3OFe024b. (a) shows the full field sweep with loops performed from starting fields of 500 Oe, 800 Oe, 0.1 T, 0.5 T, 1 T, 3 T and 7 T. (b) shows that at ∼ 1.5 T there appears to be a slight jump in magnetisation for loop ● that is not reproduced for loop ○. (c) shows an increase in magnetisation at 0 H for each loop increasing in applied field, giving a displacement along the y axis. (d) indicates that the displacement along y is greatest for the highest starting fields.

5.3 Conclusions

The susceptibility and hysteresis measurements presented here indicate that the main anisotropy present in hydronium jarosite is due to to the crystal electric field. Further, the synthesis of hydronium jarosite samples that show a wide range of values of T_g provides the opportunity to understand what drives its spin glass transition and sets it apart from the jarosites that display Néel order. These points will be discussed again in the following chapters.

Chapter 6

Elemental analysis results of iron jarosites

Elemental analysis is crucial to determine how effective the synthesis methods, and in particular the Fe coverage, relate to the magnetic transitions. There were several methods used to try and determine elemental composition, ICP-AES, SEM EDAX, and combustion analysis. These techniques were introduced in Sections 3.2 and 3.3.

6.1 EDAX SEM Elemental analysis

EDAX appears to be the simplest technique to study the composition of the jarosites. Unfortunately the electron beams used are strong enough to cause extensive damage to the surface of the jarosite crystallites and vaporises the water contained within the structure. This leads to very erroneous Fe:S ratios. Therefore no meaningful elemental analysis using EDAX can be undertaken using the synthetic jarosites made in this project, in particular hydronium jarosites with their high water content. Figure 6.1 shows two examples how the electron beam burns the jarosite surface.

6.2 ICP-AES Analysis

Inductively coupled plasma - atomic emission spectroscopy is a very sensitive elemental analysis technique [158]. The machine used was a Perkin-Elmer Optima 3300RL ICP-OES of the NERC facility at Royal Holloway University operating at 1.5 cm^3 of Ar per minute. The samples were mounted on a AS91 autosampler (carousel) and the solution was drawn up through each position on the carousel using a peristaltic

(a) SEM image of electron beam damage upon natural Pb jarosite

(b) SEM image of electron beam damage upon natural Pb jarosite

Figure 6.1: SEM images of natural Pb jarosite from the Natural History Museum [BM 1966,403] showing electron beam damage. These images have been gratefully received from Adrian Smith [14].

pump into the cross-flow type nebulizer and from there the sample was sprayed into a Ar plasma torch. The resultant spectral emission lines are separated by an Echelle grating polychromator and detected with a segmented-array charge-coupled-device detector. The operating settings were: frequency 40 Hz; power 1.3 kW and observation height of 15 mm. Samples typically weighing $0.1000\,\mathrm{g} \pm 0.0002\,\mathrm{g}$ were dissolved in $2\,\mathrm{cm}^3$ of HCl/HNO_3 by gently warming on a hot plate. The solution was made up to $20\,\mathrm{cm}^3$ with distilled water. Results are tabulated in Tables 6.1 – 6.4.

The tables show: the sample label, synthesis conditions, and stoichiometric formula for each sample. Some samples were remeasured after the optics of the system had been fixed, as previously reported sulphur intensities had been low; nonetheless the data from these "poor" sulphur intensities appear good. Sample purity was confirmed using both X-ray powder diffraction and SEM (Section 4.4).

The data were analysed by initially calculating which spectral wavelength (channel) for each element produced the smallest σ in intensities with reference to the periodic arrangement of blanks on the sample carousel. The intensities of a chosen channel from each sample had to be corrected for drift. This was done by a linear interpolation of the drift of each of the sample intensities between the periodic arrangement of the blanks. A calibration curve was set up by obtaining the gradient of the chosen channel from the intensities of known standard ppm element solutions also arranged upon the sample carousel. For sulphur, 10 ppm and 1000 pm standard solutions were used and for Fe 10 ppm, 500 ppm and 1000 ppm standard solutions were used. There are two points which may limit the data collected, but are easily resolved. First, the intensities produced from the samples were above the range defined by the standard elemental ppm Fe solutions on the calibration curve and thus the gradient used is an extrapolation for the Fe data. The intensities from the samples were approximately two times greater than Fe 1000 ppm and maximum counts for Fe never rose above 1500. With the chamber approaching saturation, towards 3 million counts, a linear extrapolation is acceptable.

The second issue is the low counts for the sulphur due to oxygen present in the chamber which absorbs the spectral emission of sulphur. The Perkin-Elmer Optima 3300RL instrument is stated to have an uncertainty of 0.13 % for Fe but no data are available for S. With sulphur counts as low as 600, precision for the sulphur is potentially a problem. This was resolved by generating actual experimental standard deviations as monitored by the drifts and by measuring 10 ppm sulphur standards placed at intervals no greater than 1 between every 10 samples on the carousel.

This generated a consistent experimental error for 10 ppm sulphur standards and this contributed towards overall experimental standard deviation error of ±0.93 % in the Fe:SO ratio. Once the calibration curve was known, then both the elemental ppm could be calculated and thus the corresponding relative molar quantities for each sample. Conversion to molar quantities is achieved by dividing the ppm value by the relative atomic mass for Fe or S. The relative formula amount of Fe is obtained by dividing the Fe mmol quantity through by the S mmol value and multiplying by 2. The rules for determining jarosite stoichiometric formula are laid out by Kubisz [12], and follows the assumption that the sulphate value is always 2.

The ICP-AES results set out below are kept generally in sequence order on the carrousel within the hydronium and non-hydronium types in an effort to make clear any systemic errors. Tables 6.1 and 6.2 are in order of sequence and that was the first batch to be processed. The last two remaining tables (6.3 and 6.4) show the second batch, with data taken on the same day. There was some difficulty in interpreting the Fe data as only Fe 10 ppm and 500 ppm standards were used and no repeat of the 1000 ppm standard was made for the last two batches. This makes it harder to determine whether any substantial shift had occurred and the extrapolation required is even greater. Results for the hydronium jarosites in Table 6.3 are for an average in calibration between Fe 500 ppm and 1000 ppm to make a reasonable comparison with the other hydronium jarosites. The formulae quoted in Table 6.4 are based upon the 500 ppm calibration curve used for sample KFeMIT. This was the only sample that fits within that calibration range and the oxidative method purports 100 % Fe coverage. Thus, for comparison between other non-hydronium samples this is considered the best compromise.

6.3 Discussion of ICP-AES results

The results indicate that the MeOH concentration has more effect on the Fe coverage than temperature, as low MeOH concentration coincides with high Fe coverage for all temperatures. The very high MeOH concentrations result in unwanted Fe oxy-hydroxy sulphates; at the modest temperature of 120 °C it promotes the growth of X-ray diffraction amorphous Schwertmannite and at higher temperatures gives rise to other unwanted Fe oxy-hydroxy sulphates, H3OS36 and H3OS37 (Table 6.2) which all give substantially lower values for Fe coverage.

It is notable that the Fe occupation is high or very high for all of the hydronium

Table 6.1: Elemental analysis results of MeOH solvent prepared hydronium jarosites using a Perkin-Elmer Optima 3300RL ICP-OES together with synthesis conditions (temperature and H_2O/MeOH solvent mix), Fe and SO_4 concentrations and ratio, and spin glass freezing temperature, T_g. The results are displayed in order of the experimental sequence.

Sample ID	Temp (°C)	%H_2O	Fe (mmol)	SO_4 (mmol)	Fe:SO_4	Formula	T_g (K) $\pm$ 0.2K
H3OFeS1	150	90	27.198	18.014	3.02	$H_3OFe_{3.00}(SO_4)_2(OH)_{6.00}(H_2O)_{0.00}$	15.7
H3OFeS2	150	80	27.153	18.209	2.98	$H_3OFe_{2.98}(SO_4)_2(OH)_{5.95}(H_2O)_{0.05}$	15.4
H3OFeS3	150	70	26.704	18.248	2.93	$H_3OFe_{2.93}(SO_4)_2(OH)_{5.78}(H_2O)_{0.22}$	14.8
H3OFeS4	150	60	28.090	19.040	2.95	$H_3OFe_{2.95}(SO_4)_2(OH)_{5.85}(H_2O)_{0.15}$	13.9
H3OFeS9	120	90	27.640	18.828	2.94	$H_3OFe_{2.94}(SO_4)_2(OH)_{5.81}(H_2O)_{0.19}$	18.8
H3OFeS10	120	80	28.389	18.879	3.01	$H_3OFe_{3.00}(SO_4)_2(OH)_{6.00}(H_2O)_{0.00}$	18.4
H3OFeS11	120	70	28.925	19.397	2.98	$H_3OFe_{2.98}(SO_4)_2(OH)_{5.95}(H_2O)_{0.05}$	17.2
H3OFeS13	120	50	28.220	19.559	2.89	$H_3OFe_{2.89}(SO_4)_2(OH)_{5.66}(H_2O)_{0.34}$	14.8
H3OFeS14	120	40	28.099	19.724	2.85	$H_3OFe_{2.85}(SO_4)_2(OH)_{5.55}(H_2O)_{0.45}$	12.7
H3OFeS15✠	120	30	27.100	19.655	2.76	$H_3OFe_{2.76}(SO_4)_2(OH)_{5.27}(H_2O)_{0.73}$	12.1
H3OFeS16§	120	20	26.676	21.311	2.50	$H_3OFe_{2.50}(SO_4)_2(OH)_{4.51}(H_2O)_{1.49}$	11.3
H3OFeS17	150	75	27.555	18.824	2.93	$H_3OFe_{2.93}(SO_4)_2(OH)_{5.78}(H_2O)_{0.22}$	14.6
H3OFeS18	150	65	27.993	19.172	2.92	$H_3OFe_{2.92}(SO_4)_2(OH)_{5.76}(H_2O)_{0.24}$	14.5
H3OFeS20†	120	10	23.908	24.697	1.94	$H_3OFe_{1.94}(SO_4)_2(OH)_{2.81}(H_2O)_{3.19}$	N/A

✠ It is unconfirmed whether this sample contains an impurity phase of Schwertmannite, though there is a probability, refer to sample H3OFeS16§ and Figure 6.2.

§ Numerous clusters of Schwertmannite as evidenced under SEM Figure 4.4(e).

† Possible Mikasaite - crystalline $Fe_2(SO_4)_3$ - evidenced from SEM Figure 4.7(f).

Table 6.2: Elemental analysis results of MeOH solvent prepared hydronium jarosites using Perkin-Elmer Optima 3300RL ICP-OES together with synthesis conditions (temperature and H_2O/MeOH solvent mix), Fe and SO_4 concentrations and ratio, and spin glass freezing temperature, T_g. The results are displayed in order of the experimental sequence.

Sample ID	Temp (°C)	%H_2O	Fe (mmol)	SO_4 (mmol)	Fe:SO_4	Formula	T_g (K) ± 0.2K
H3OFeS21	130	90	28.349	18.937	2.99	$H_3OFe_{2.99}(SO_4)_2(OH)_{5.98}(H_2O)_{0.02}$	17.4
H3OFeS22	130	80	28.396	19.354	2.93	$H_3OFe_{2.93}(SO_4)_2(OH)_{5.80}(H_2O)_{0.20}$	16.6
H3OFeS23	130	70	28.260	19.133	2.95	$H_3OFe_{2.95}(SO_4)_2(OH)_{5.86}(H_2O)_{0.14}$	12.0
H3OFeS24	130	60	27.453	18.778	2.92	$H_3OFe_{2.92}(SO_4)_2(OH)_{5.77}(H_2O)_{0.23}$	14.1
H3OFeS26	130	50	27.493	19.063	2.88	$H_3OFe_{2.88}(SO_4)_2(OH)_{5.65}(H_2O)_{0.35}$	12.0
H3OFeS27✠	130	40	27.066	19.501	2.78	$H_3OFe_{2.78}(SO_4)_2(OH)_{5.33}(H_2O)_{0.67}$	11.6
H3OFeS28§	130	30	26.713	19.826	2.69	$H_3OFe_{2.69}(SO_4)_2(OH)_{5.08}(H_2O)_{0.92}$	10.9
H3OFeS29†	130	20	22.844	24.153	1.89	$H_3OFe_{1.89}(SO_4)_2(OH)_{2.67}(H_2O)_{3.33}$	N/A
H3OFeS30	140	90	27.518	19.287	2.85	$H_3OFe_{2.85}(SO_4)_2(OH)_{5.56}(H_2O)_{0.44}$	14.2
H3OFeS31	140	80	27.892	19.680	2.83	$H_3OFe_{2.83}(SO_4)_2(OH)_{5.50}(H_2O)_{0.50}$	15.1
H3OFeS32	140	70	27.300	19.668	2.78	$H_3OFe_{2.78}(SO_4)_2(OH)_{5.33}(H_2O)_{0.67}$	14.4
H3OFeS33	140	60	27.672	19.577	2.83	$H_3OFe_{2.83}(SO_4)_2(OH)_{5.48}(H_2O)_{0.52}$	13.7
H3OFeS34	140	50	27.901	19.966	2.79	$H_3OFe_{2.79}(SO_4)_2(OH)_{5.38}(H_2O)_{0.62}$	13.9
H3OFeS35‡	140	40	27.756	20.345	2.73	$H_3OFe_{2.73}(SO_4)_2(OH)_{5.19}(H_2O)_{0.81}$	12.3
H3OFeS36‡	140	30	27.363	21.980	2.49	$H_3OFe_{2.49}(SO_4)_2(OH)_{4.47}(H_2O)_{1.53}$	11.5
H3OFeS37‡	140	20	26.515	24.139	2.20	$H_3OFe_{2.20}(SO_4)_2(OH)_{3.59}(H_2O)_{2.41}$	10.9
H3OFeS38†	140	10	26.044	27.209	1.91	$H_3OFe_{1.91}(SO_4)_2(OH)_{2.74}(H_2O)_{3.26}$	N/A

✠ The appearance of another X-ray amorphous Fe oxy-hydroxy sulphate similar in morphology to Schwertmannite.

§ The appearance of Schwertmannite as evidenced under SEM. Refer to Figure 4.4(e) as an example of Schwertmannite growth on the surface of jarosite.

† Possible Mikasaite - crystalline $Fe_2(SO_4)_3$ similar product produced as for sample H3OFeS20 refer to SEM Figure 4.7(f)

‡ Contains another phase of unwanted Fe oxy-hydroxy sulphates determined from powder XRD

Table 6.3: Elemental analysis results of 100% H_2O solvent prepared hydronium jarosites using a Perkin-Elmer Optima 3300RL ICP-OES together with synthesis conditions (temperature and time), Fe and SO_4 concentrations and ratio, and spin glass freezing temperature, T_g. The results are displayed in order of the experimental sequence. Unsubstantiated drift may have occurred to have given rise to almost perfect Fe coverage.

Sample ID	Temp (°C)	Time (hrs)	Fe (mmol)	SO_4 (mmol)	Fe:SO_4	Formula	T_g (K) ± 0.2K
H3OFe023	150	15	29.542	31.932	2.97	$H_3OFe_{2.97}(SO_4)_2(OH)_{5.90}(H_2O)_{0.10}$	N/A
H3OFe023	150	15	29.577	31.970	2.97	$H_3OFe_{2.97}(SO_4)_2(OH)_{5.90}(H_2O)_{0.10}$	N/A
H3OFe050	150	15	30.125	32.562	3.02	$H_3OFe_{3.00}(SO_4)_2(OH)_{6.00}$	N/A
H30Fe043	145	21	29.937	32.359	3.04	$H_3OFe_{3.00}(SO_4)_2(OH)_{6.00}$	14.7
H30Fe022b	150	7	29.104	31.458	3.00	$H_3OFe_{3.00}(SO_4)_2(OH)_{6.00}$	N/A
H3OFe025	150	28	28.698	31.019	3.01	$H_3OFe_{3.00}(SO_4)_2(OH)_{6.00}$	N/A
H3OFe025b	150	28	29.298	31.668	3.06	$H_3OFe_{3.00}(SO_4)_2(OH)_{6.00}$	N/A
H30Fe026	150	48	29.157	31.516	3.01	$H_3OFe_{3.00}(SO_4)_2(OH)_{6.00}$	N/A
H3OFe027	150	80	29.209	31.571	3.05	$H_3OFe_{3.00}(SO_4)_2(OH)_{6.00}$	15.7
H3OFe027	150	80	30.067	32.491	3.06	$H_3OFe_{3.00}(SO_4)_2(OH)_{6.00}$	15.7
H30Fe024	150	21	29.989	32.415	3.04	$H_3OFe_{3.00}(SO_4)_2(OH)_{6.00}$	15.6
H3OFe047	142	21	30.342	32.796	3.09	$H_3OFe_{3.00}(SO_4)_2(OH)_{6.00}$	16.8
H3OFe048	138	21	30.078	32.511	3.09	$H_3OFe_{3.00}(SO_4)_2(OH)_{6.00}$	16.6
H3OFe049	145	21	29.580	31.972	3.04	$H_3OFe_{3.00}(SO_4)_2(OH)_{6.00}$	15.8
H3OFe046	142	21	29.558	31.949	3.11	$H_3OFe_{3.00}(SO_4)_2(OH)_{6.00}$	17.2
H3OFe021	150	4	28.979	31.323	3.06	$H_3OFe_{3.00}(SO_4)_2(OH)_{6.00}$	15.5
H3OFe045	138	21	29.129	31.485	3.15	$H_3OFe_{3.00}(SO_4)_2(OH)_{6.00}$	17.5
H3OFe022	150	7	29.744	32.149	3.16	$H_3OFe_{3.00}(SO_4)_2(OH)_{6.00}$	N/A
H3OFe041	120	48	29.404	31.783	3.13	$H_3OFe_{3.00}(SO_4)_2(OH)_{6.00}$	N/A

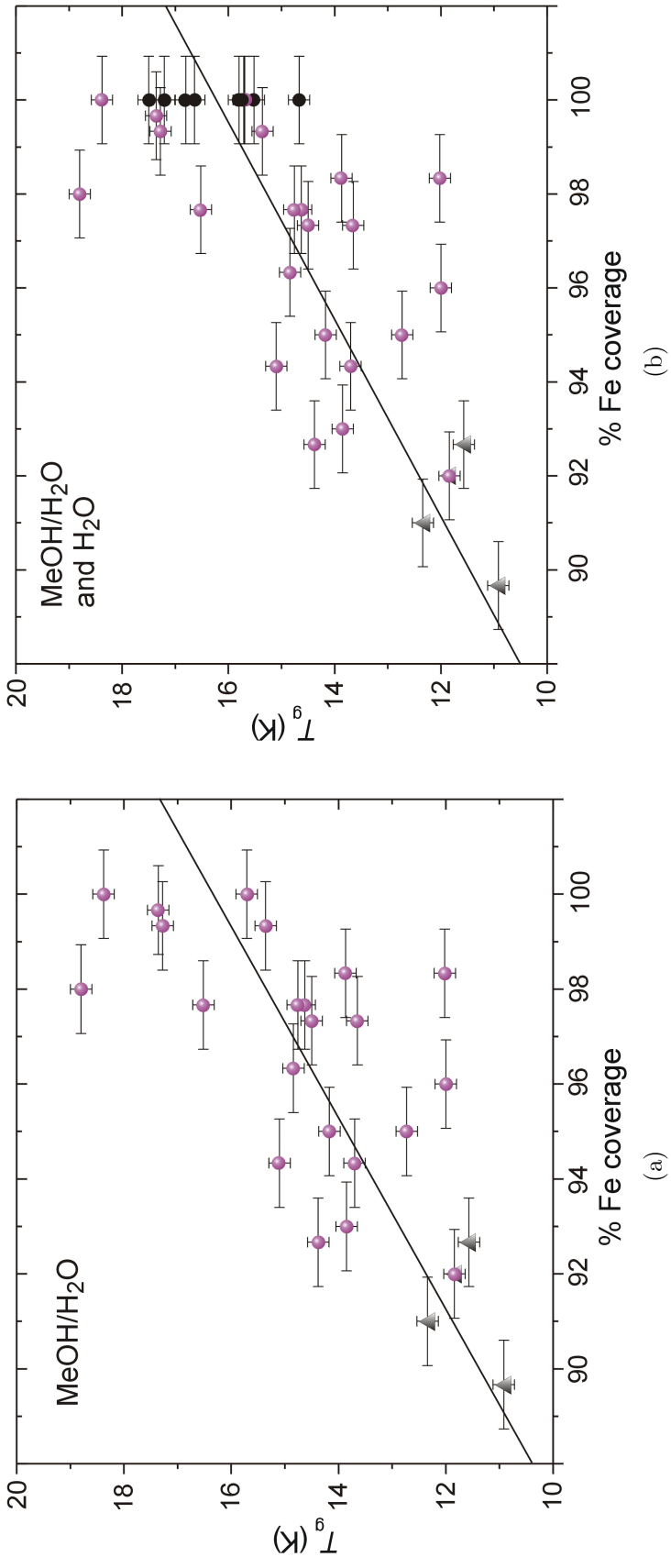

Figure 6.2: (a) is a plot of T_g against Fe coverage for hydronium samples prepared using MeOH (purple circles) as part of the solvent and (b) is a plot of T_g against Fe coverage for all hydronium samples used in the ICP-AES analysis. The graphs show that the lowest spin glass freezing temperatures are obtained with higher concentrations of the MeOH and corresponds to a slight decrease in Fe % coverage. The data in the graphs show no clear relation between Fe coverage and T_g. Consider those samples with the lowest values for T_g and % Fe coverage: they contain impurity phases of unwanted Fe oxy-hydroxy sulphates (shown in triangles) that give rise to an underestimation of the Fe occupation, this further confirms that there is no clear relation between Fe coverage and T_g. It is noted that the hydronium jarosites prepared in 100% H_2O solvent (black circles) appear to have near perfect 100% Fe coverage and still possess a significant variation in T_g. It is inconclusive whether the sample (H3OFeS15) shown with both a circle and triangle contains an unwanted Fe oxy-hydroxy sulphate phase. The probability is high as the synthesis conditions are very similar to the sample (H3OFeS16) with the lowest % Fe coverage.

jarosite samples, though unsubstantiated drift might be occurring towards the end of the measurements for the hydronium samples (Table 6.3) prepared using 100% H_2O as solvent. It appears that neither time nor temperature of synthesis make an impact upon Fe coverage. The range in T_g is smaller for hydronium jarosite samples prepared in water than using MeOH/H_2O mixes. Figures 6.2(b) and 6.2(a) show T_g plotted against Fe % coverage for all hydronium jarosite samples; it confirms that lower values of T_g can be achieved using high concentrations of MeOH and that there is a corresponding decrease in Fe coverage. Despite this, the Fe occupation remains high with only one sample having a Fe coverage of less than 90% and the lowest 4 Fe coverage samples, indicated with triangles, contain impurities. These results indicate that lower Fe coverage is not possible within the hydronium jarosites structure and instead unwanted Fe-oxy-hydroxy sulphates form. This can be seen in samples H3OFeS16, H3OFeS20, H3OFeS29, H3OFeS36-H3OFeS38 where unwanted Fe oxy-hydroxy sulphates appear (SEM Figures 4.4(e), 4.4(f), 4.7(f)).

High Fe coverage is therefore crucial for the formation of hydronium jarosite and is less likely the determinant for the nature and temperature of the spin glass transition. Another factor must provide an alternative energy scale for the varying spin-glass transition temperatures for hydronium jarosites. Likewise Table 6.4 shows that Fe coverage is unlikely to influence the nature and the temperature of the magnetic transitions for the non-hydronium jarosites.

The non-hydronium jarosites provide a very interesting contrast to hydronium jarosites. Firstly, a lower Fe coverage can be sustained within the jarosite structure. This is evident with the synthetic potassium jarosite formed under forced hydrolysis conditions, samples KFe1, KFe3-6. These all have low Fe coverage reaching as little as 81%. This was also noted in previous work [14] where potassium jarosites made in non-hydrothermal conditions ($\sim$ 98 °C) had a similar Fe coverage $\sim$82%. This Fe loss is incredible as it corresponds to a fifth of all Fe atoms[1], and yet long range magnetic order still persists with similar transition temperatures for KFeRedox which has a Fe coverage of $\sim$100%. This then proves that any disorder from Fe vacancy has minimal effect upon the magnetism which confers with recent reported work [159]. A recent review on SCGO [96], another structure containing a

[1]It has been calculated that the percolation limit for the *kagomé* network using nearest neighbour interactions (Potts model with q=1) is 0.524 [139] for bond disorder or 0.653 [138] for site disorder

Table 6.4: Elemental analysis results for non-H_3O^+ jarosites using a Perkin-Elmer Optima 3300RL ICP-OES together with A-site (some not obtainable), Fe and SO_4 concentrations and the Fe:SO_4 ratio. Non-hydronium jarosites generally show two transitions, labeled T_{N_1} and T_{N_2}: T_{N_1} occurs higher in temperature. The results are displayed in order of the experimental sequence within the same A-site. Increase in the uptake of hydronium in the A-site results in a decrease in temperature for the magnetic transitions.

Sample ID	A-site (mmol)	Fe (mmol)	SO_4 (mmol)	Fe:SO_4[§]	Formula[‡]	T_c (K) ± 0.2K
RbFe1		23.451	16.675	2.81	$RbFe_{2.81}(SO_4)_2(OH)_{5.44}(H_2O)_{0.56}$	63.9, (50.00)
RbFe2		23.736	16.344	2.91	$RbFe_{2.91}(SO_4)_2(OH)_{5.71}(H_2O)_{0.29}$	64.2, 50.7
RbFe3		23.413	16.871	2.78	$RbFe_{2.78}(SO_4)_2(OH)_{5.33}(H_2O)_{0.67}$	45.00
NaFe1	7.227	25.281	18.395	2.75	$Na_{0.79}(H_3O)_{0.21}Fe_{2.75}(SO_4)_2(OH)_{5.25}(H_2O)_{0.75}$	(60.8), 43.9
NaFe2	5.295	26.972	18.980	2.84	$Na_{0.56}(H_3O)_{0.44}Fe_{2.84}(SO_4)_2(OH)_{5.53}(H_2O)_{0.47}$	(61.0), 43.0
NaFe3	3.882	26.766	19.091	2.80	$Na_{0.41}(H_3O)_{0.59}Fe_{2.80}(SO_4)_2(OH)_{5.41}(H_2O)_{0.59}$	(60.0), 39.5
NH4Fe1		25.586	18.822	2.72	$NH_4Fe_{2.72}(SO_4)_2(OH)_{5.16}(H_2O)_{0.84}$	61.4, 52.0
NH4Fe2		26.543	18.729	2.83	$NH_4Fe_{2.83}(SO_4)_2(OH)_{5.50}(H_2O)_{0.50}$	43.5
NH4Fe3		26.807	19.128	2.80	$NH_4Fe_{2.80}(SO_4)_2(OH)_{5.41}(H_2O)_{0.59}$	61.3, 50.5
KFe1	8.485	25.205	19.202	2.63	$K_{0.88}(H_3O)_{0.12}Fe_{2.63}(SO_4)_2(OH)_{4.88}(H_2O)_{0.10}$	64.5, 45.0
KFe3	8.566	24.580	18.819	2.61	$K_{0.91}(H_3O)_{0.09}Fe_{2.61}(SO_4)_2(OH)_{4.84}(H_2O)_{0.10}$	64.2
KFe4	7.975	25.367	19.397	2.62	$K_{0.82}(H_3O)_{0.18}Fe_{2.62}(SO_4)_2(OH)_{4.85}(H_2O)_{0.10}$	(64.2), 50.3
KFe5	8.163	24.346	19.954	2.44	$K_{0.82}(H_3O)_{0.18}Fe_{2.44}(SO_4)_2(OH)_{4.32}(H_2O)_{0.10}$	63.6, 47.0
KFe6	7.042	25.029	19.873	2.53	$K_{0.71}(H_3O)_{0.29}Fe_{2.53}(SO_4)_2(OH)_{4.56}(H_2O)_{0.10}$	47.3
KFeMIT[†]	2.589	7.469	4.975	3.00	$KFe_{3.00}(SO_4)_2(OH)_6$	65.0
$KFe_{natural}$				2.99	$KFe_{2.99}(SO_4)_2(OH)_{5.97}(H_2O)_{0.03}$	63.2, 50.6
KFeMIT♯11		33.27[♯]		2.98	$KFe_{2.98}(SO_4)_2(OH)_{5.94}(H_2O)_{0.06}$	62.5, 53.6
AgFe1		20.707	15.400	2.69	$AgFe_{2.69}(SO_4)_2(OH)_{5.07}(H_2O)_{0.93}$	N/A
AgFe2		22.643	16.578	2.73	$AgFe_{2.73}(SO_4)_2(OH)_{5.12}(H_2O)_{0.80}$	N/A
AgFe3		22.515	16.791	2.68	$AgFe_{2.68}(SO_4)_2(OH)_{5.05}(H_2O)_{0.95}$	44.3

[§] The Fe:S ratio was produced using the calibration curve between Fe 10ppm and 500ppm to make a comparison with KFeMIT, which further verifies that the oxidatative preparation produces 100% Fe coverage. [20]

[‡] A-site determination can not be carried out for elements Ag, Rb and NH_4 because it is not possible to obtain these A-sites with this experimental setup.

[†] The dissolved mass of this sample was small and therefore was in the calibration range of the Fe standards used.

[♯] Actual % weight value for Fe. Measurement taken on the same machine with a different calibration method.

kagomé network made up from Cr^{3+} ions, similarly shows that the magnetic system (which exhibits short range magnetic correlations to 0 K) is robust to site vacancies of Cr^{3+} ions [99].

An important result from the data shown in Table 6.4 is that the concentrations of A-site used have little effect on the Fe coverage, but does correlate with A-site uptake versus hydronium uptake; apart from the potassium jarosite where K uptake is far more preferable to hydronium uptake. These results confirm the formation mechanism for jarosites as explained in Chapter 4, that the jarosite precursor is not determined by the A-site. Increase in the the uptake of hydronium in the A-site results in a decrease in temperature for the magnetic transitions [159]. Non-hydronium jarosites generally show two transitions, labeled T_{N_1} and T_{N_2}. Transition T_{N_1} occurs higher in temperature (60-65 K) and T_{N_2} appears lower (45-55 K). Increase of hydronium in the A-site results in T_{N_1} becoming broader and eventually no longer discernible from the susceptibility data. Values of T_{N_1} that are broad are shown in parentheses in Table 6.4. Relative high occupations of hydronium in the A-site is seen to decrease the temperature at which the final (and sometimes only) transition occurs. Examples of samples with a high hydronium content and correspondingly low single magnetic transitions are RbFe3, NaFe3, NH4Fe3, KFe6 and AgFe3 (refer to Table 4.3 for synthesis conditions).

6.4 Conclusion of ICP-AES results

The ICP-AES results show some very important points in connection with the magnetism and the structure of jarosite mineral. Hydronium jarosite has less tolerance to Fe disorder before the structure deteriorates, an observation that may explain why hydronium jarosite is prone to crystal growth defects [23] shown in Figure 6.3.

Furthermore, increase in MeOH concentration for the solvent causes a decrease in T_g, though this is not necessarily closely related to Fe coverage as shown in Figure 6.2. Only very low values of T_g correspond to a decrease in Fe coverage, but that can also highlight the breakdown of the jarosite structure into other unwanted Fe-oxy-hydroxy sulphates. Susceptibility data for samples with very low values of T_g have an increase in the super-paramagnetic background susceptibility during and below T_g; whether this comes from non-jarosite phases of Fe oxy-hydroxy sulphates or from the jarosite sample itself is not clear, especially where a raised background susceptibility is noticed but no secondary phases are evidenced through SEM or

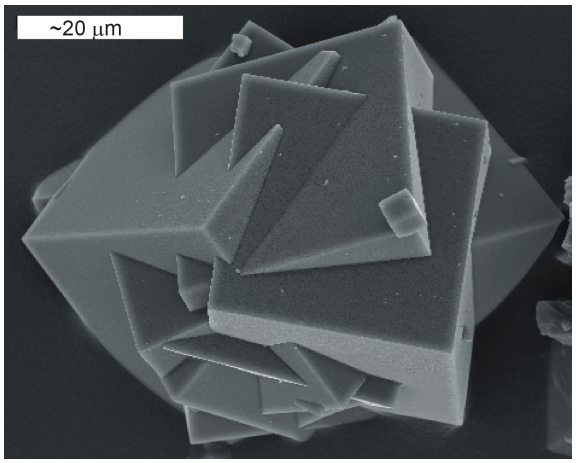

Figure 6.3: An SEM pictures showing crystal growth of interpenetrating twins arising in hydronium jarosite sample H3OFeS10. This sample returned 100% Fe coverage; a slight Fe loss results in more severe growth defects as shown in Figure 4.5(e).

powder XRD (as discussed in the next section). If it can be shown that the presence of unwanted Fe oxy-hydroxy sulphates are minimal or do not affect the bulk magnetic response and that the increase in super-paramagnetic susceptibility is from the hydronium jarosite sample and the Fe vacancies, then this may point towards the occurrence of solitons [160], moments decoupling from the frustrated manifold and propagating as singlets throughout the *kagomé* lattice.

Another very important result is the robustness of the structure of non-hydronium jarosites towards Fe vacancies. The structure can sustain a loss of up to 20% Fe, far more than hydronium jarosites. This clearly demonstrates that it is the A-site which determines the nature and temperature of the magnetic transition. The hydronium structure has the largest a parameter for the jarosites [3] and it is the slight structural differences due to the incorporation of the hydronium ion that is explored in the next two sections.

Chapter 7

Powder Diffraction Results and Analysis of Iron Jarosites

Powder diffraction is an extremely useful technique to determine the phase purity and the lattice parameters of crystalline materials. The results presented here are collected from two laboratory powder X-ray diffraction machines, a Bruker D8 ($Cu\,K_\alpha$) used for lattice parameters and pattern matching, and a Panalytical X'pert Pro ($Co\,K_\alpha$) for phase analysis.

7.1 Phase identification of the synthesised jarosites

Hydronium jarosite displays two strong reflections at approximate $2\theta \sim 14.50°$ and $14.26°$, d$\sim$ 3.08 Å and 3.13 Å respectively, (Figure 7.1(a)). The absence of two distinct reflections at approximately $2\theta \sim 14.30°$ and $13.72°$, d$\sim$ 3.12 Å and 3.25 Å, due to unwanted iron oxy-hydroxy sulphates (Figure 7.1(b)) indicates that the product is single phase jarosite. For comparison the X-ray powder diffraction pattern of H3OS36, collected on the D8 is shown in Figure 7.1(b). The sample has two phases: hydronium jarosite and an unwanted Fe oxy-hydroxy sulphate. The plot shows two non-jarosite reflections at $2\theta \sim 27°$.

Higher quality data collected for samples H3OFeS34, H3OFeS35 and H3OFeS36 using Co radiation on a Panalytical X'pert Pro with a Ge $< 111 >$ monochromator are shown in Figure 7.2. The jarosite peak positions were generated from a known structural model [21] and the unwanted phase was determined by pattern matching using the software EVA, by Bruker, as the Fe oxy-hydroxy sulphate phase to be Fe sulphate hydroxide, $Fe(OH)SO_4$ (ICDD reference 21:0428). The diffraction patterns

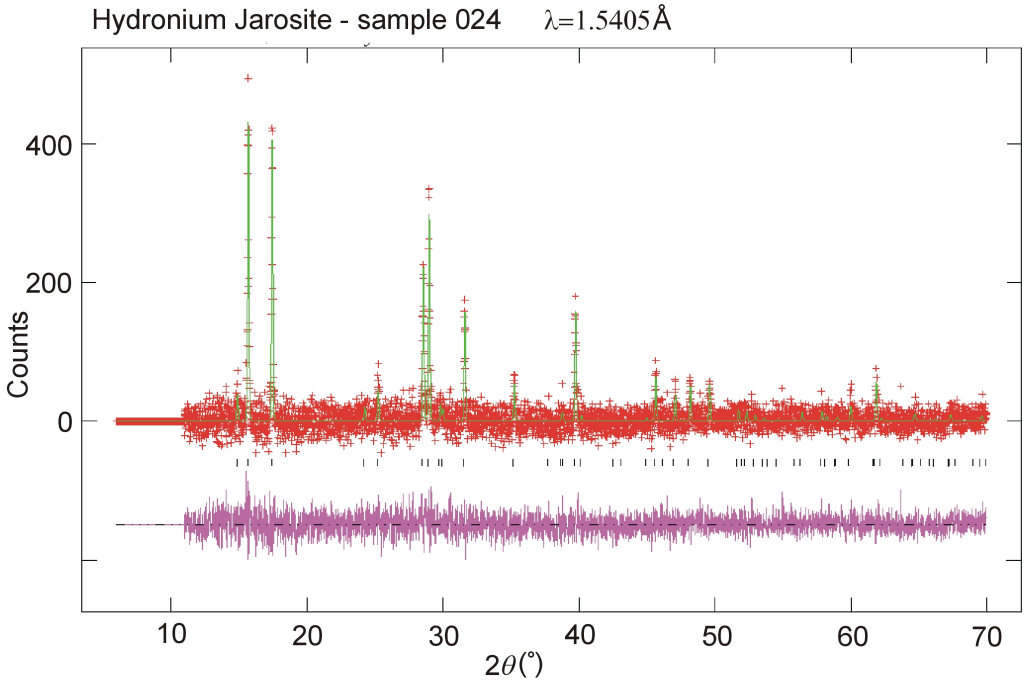

(a) H3OFe24 with no discernible impurity

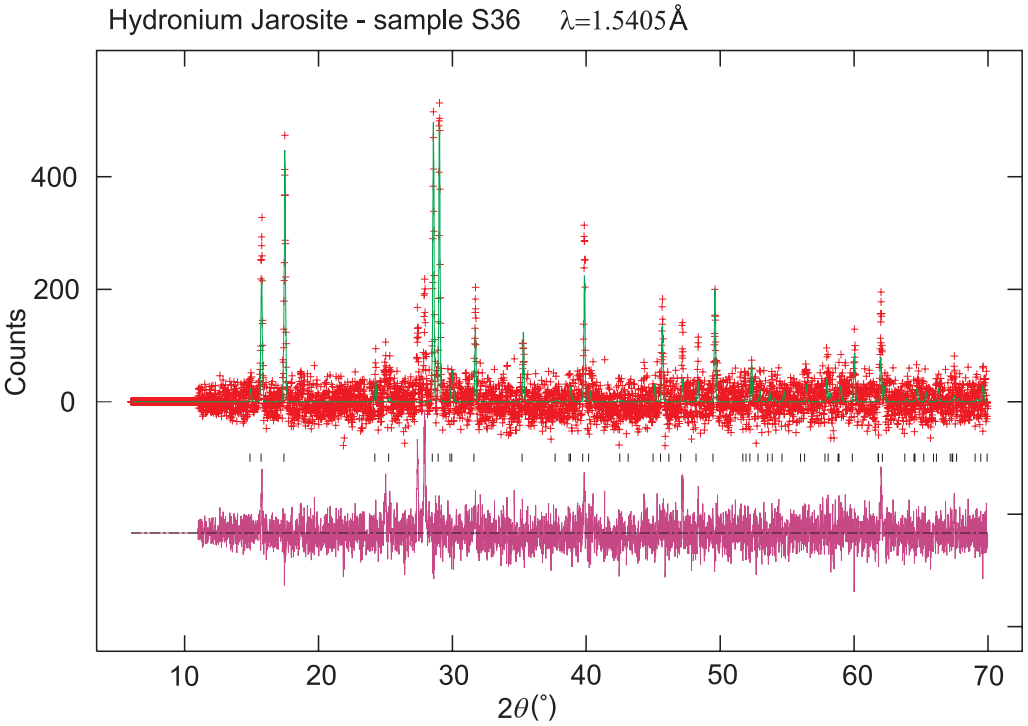

(b) H3OFeS36 with the appearance of unwanted Fe oxy-hydroxy sulphates

Figure 7.1: Rietveld refinement plots for hydronium jarosite samples H3OFe024 (top) and H3OFeS36 (bottom) taken from the D8 diffractometer at room temperature. There is a raised background due to the Cu radiation causing the Fe to fluoresce, leaving the data sufficient only to obtain lattice parameters. The purple plot is the difference between the observed data (red) and the model (green). The same set-up was used for all the other jarosites listed in Tables 7.1 and 7.2.

of samples H3OFeS35 and H3OFeS36 may contain reflections from other Fe sulphates hydrates/hydroxides that could not be determined. The small presence of unwanted Fe oxy-hydroxy sulphates may explain the reduction of the Fe occupation for these samples and those between H3OFeS34 (93 %) and H3OFeS37 (73 %) in the previous chapter as unwanted Fe oxy-hydroxy sulphates typically have a lower Fe % weight than hydronium jarosite.

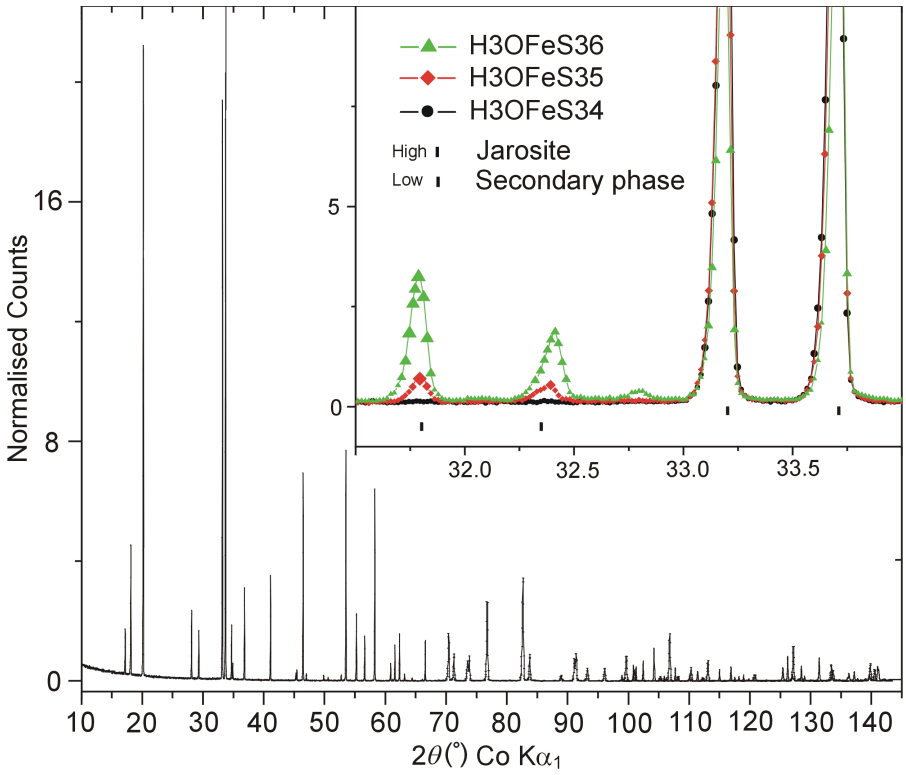

Figure 7.2: X-ray diffraction pattern for sample H3OFeS34, the data were collected on a Pananalytical X'pert Pro with a Co source and Ge <111> monochromator. The insert shows that sample H3OFeS34 (black circles) has no impurity phase, whereas samples H3OFeS35 (red diamonds) and H3OFeS36 (green triangles) clearly show an unwanted secondary phase present. The secondary phase were determined by the pattern matching software EVA and is likely to be a phase of $Fe(OH)SO_4$ (ICDD ref: 21:0428).

7.2 Comparison of lattice parameters with spin-glass transition temperature for hydronium jarosites.

All the lattice parameter data for the proceeding section relies on a Rietveld model from the refinement of neutron data from hydronium jarosite [21]. The CuK_α X-ray

data unfortunately suffers a high background because of the Fe fluorescence (Figure 7.1(a) and only lattice parameters could be investigated. Tables 7.1 and 7.2 show the synthesis conditions, lattice parameters and basic magnetic characterisation, including the spin glass freezing temperature, T_g, for hydronium jarosites. The errors for the lattice parameters are the e.s.d.'s generated by GSAS and the error in T_g is ± 0.2 K.

Diffraction patterns taken for all of the hydronium jarosites listed in Tables 7.1 and 7.2 on the D8 show strong correlations between lattice parameters and synthesis conditions, and the spin−glass transition, T_g. Figure 7.3 shows that the hydronium jarosite samples synthesised in 100% H_2O solvent have a remarkable correlation between synthesis temperature and the spin-glass freezing temperature.

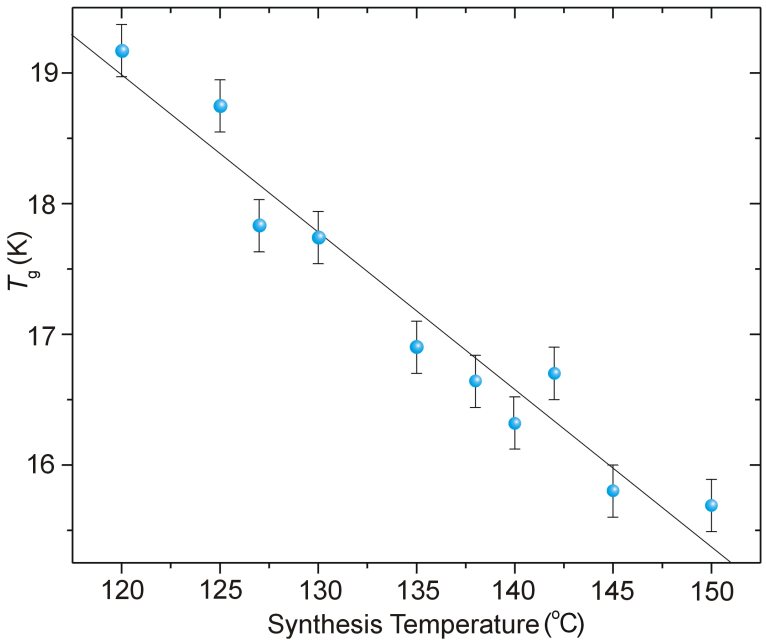

Figure 7.3: Spin-glass freezing temperatures plotted against the synthesis temperature of hydronium jarosites using 100% H_2O as solvent. It shows that the synthesis conditions can influence the spin-glass transition temperature and a strong correlation between synthesis temperature and T_g.

All the samples in Figure 7.3 were synthesised for a duration of 21 hours and clearly show that increasing the synthesis temperature lowers T_g, probably due to better crystals being formed.

Table 7.1: Table showing the synthesis conditions, lattice parameters and magnetic characterisation for hydronium jarosite samples prepared using 100% H_2O as the solvent. S.C. stands for single crystal and shows where the data were obtained, either NCS (Southampton) or SRS (Daresbury station 9.8). T_g is the spin-glass freezing temperature and θ_W is the Curie−Weiss temperature.

Synthesis				Lattice parameters (Å) (~ 298 K)			Magnetic characterisation (K)	
Sample	Temp. (°C)	%H_2O	yield (g)	a	c	S.C.	T_g (± 0.2 K)	$\theta_W(\pm 100)$
H3OFe31	120	100	0.081	7.36537(28)	17.0571(8)	N/A	19.7	−1485
H3OFe33	125	100	0.101	7.36820(30)	17.0618(8)	N/A	18.7	−1330
H3OFe44	127	100	0.312	7.3658(4)	17.0616(10)	N/A	18.0	−1465
H3OFe29	130	100	0.186	7.36940(34)	17.0548(12)	NCS	17.7	−1420
H3OFe42	135	100	0.371	7.3673(4)	17.0541(11)	SRS	16.9	−1410
H3OFe48	138	100	0.289	7.36992(25)	17.0546(6)	N/A	16.6	−1470
H3OFe30	140	100	0.340	7.37026(28)	17.0510(7)	N/A	16.3	−1475
H3OFe47	142	100	0.361	7.36796(23)	17.0460(6)	N/A	16.8	−1725
H3OFe49	145	100	0.353	7.36944(28)	17.0453(6)	NCS	15.8	−1510
H3OFe24	150	100	0.498	7.3698(4)	17.0403(9)	NCS	15.6	−1400
H3OFe16	150	100	0.458	7.3705(6)	17.0391(18)	NCS	15.8	−1580
H3OFe27	150	100	0.530	7.3688(4)	17.0389(15)	NCS	15.7	−1530

Table 7.2: Table showing the synthesis conditions, lattice parameters and magnetic characterisation for hydronium jarosite samples prepared using a mix of H_2O and MeOH as the solvent. S.C. stands for single crystal and shows where the data were obtained, either NCS (Southampton) or SRS (Daresbury station 9.8). T_g is the spin-glass freezing temperature and θ_W is the Curie−Weiss temperature.

Synthesis				Lattice parameters (Å) (~ 298 K)			Magnetic characterisation (K)	
Sample	Temp. (°C)	%H_2O	yield (g)	a	c	S.C.	T_g (± 0.2 K)	θ_W($\pm$100)
H3OFeS9	120	90	0.134	7.3668(4)	17.0613(9)	N/A	18.8	−1565
H3OFeS10	120	80	0.237	7.3650(4)	17.0547(12)	NCS	18.4	−1530
H3OFeS11	120	70	0.341	7.3670(5)	17.0513(14)	NCS	17.2	−1360
H3OFeS12	120	60	0.479	7.36833(33)	17.0488(9)	SRS	15.8	−1420
H3OFeS13	120	50	0.581	7.3699(4)	17.0421(10)	N/A	14.8	−1580
H3OFeS14	120	40	0.687	7.3706(9)	17.0211(29)	N/A	12.7	−1315
H3OFeS15	120	30	0.643	7.37523(32)	17.0125(7)	NCS	12.1	−1310
H3OFeS16	120	20	0.425	7.3738(8)	16.9960(29)	N/A	11.3	−1195
H3OFeS21	130	90	0.363	7.36734(26)	17.0540(6)	N/A	17.4	−1490
H3OFeS22	130	80	0.379	7.3694(4)	17.0520(10)	NCS	16.6	−1595
H3OFeS23_b	130	70	0.447	7.36981(34)	17.0515(8)	SRS	16.2	−1635
H3OFeS24	130	60	0.666	7.3701(5)	17.0412(15)	NCS	14.1	−1480
H3OFeS25	130	50	0.559	7.37265(32)	17.0345(8)	SRS	13.1	−1520
H3OFeS26	130	40	0.745	7.3726(5)	17.0144(13)	SRS	12.0	−1355
H3OFeS27	130	30	0.903	7.37262(29)	16.9936(6)	NCS	11.6	−1285
H3OFeS28	130	20	0.765	7.37631(29)	16.9846(6)	N/A	10.9	−1305
H3OFeS30	140	90	0.573	7.37231(24)	17.0378(7)	SRS	14.2	−1670
H3OFeS31	140	80	0.415	7.37206(29)	17.0491(9)	N/A	15.1	−1560
H3OFeS32	140	70	0.543	7.3698(4)	17.0360(11)	N/A	14.4	−1680
H3OFeS33	140	60	0.613	7.37401(29)	17.0365(9)	NCS	13.7	−1475
H3OFeS34	140	50	0.747	7.37193(23)	17.0289(7)	N/A	13.9	−1440
H3OFeS35	140	40	0.852	7.37506(25)	17.0203(8)	N/A	12.3	−1555
H3OFeSS36	140	30	1.022	Contains unwanted Fe hydroxy sulphates			11.5	−1500
H3OFeSS37	140	20	1.134	Contains unwanted Fe hydroxy sulphates			10.9	−1750
H3OFeS1	150	90	0.514	7.3746(4)	17.0554(14)	N/A	15.7	−1490
H3OFeS2	150	80	0.571	7.3726(4)	17.0426(12)	N/A	15.4	−1505
H3OFeS17	150	75	0.584	7.3686(5)	17.0327(14)	N/A	14.6	−1415
H3OFeS3	150	70	0.655	7.37246(26)	17.0393(9)	N/A	14.8	−1415
H3OFeS18	150	65	0.638	7.3712(4)	17.0316(12)	N/A	14.5	−1450
H3OFeS4	150	60	0.711	7.37436(27)	17.0308(10)	N/A	13.9	−1400

7.2.1 Relating the lattice parameters with T_g.

The lattice parameter refinements indicate that a contraction along the c lattice parameter correlates strongly with decreasing T_g as shown in Figure 7.4. This relationship continues for the hydronium jarosites prepared using MeOH/H_2O mixes shown in Figure 7.5.

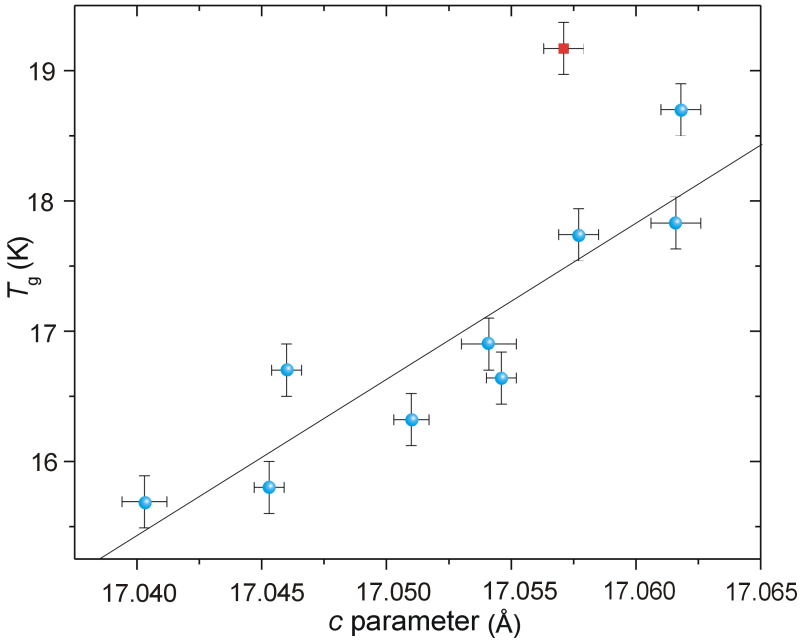

Figure 7.4: T_g plotted against the c parameter, diffraction data were collected at room temperature, of the crystal structure for hydronium jarosites synthesised in 100% H_2O solvent; the samples included are listed in Table 7.1. The graph shows how an increasing T_g correlates with an increasing c parameter of the unit cell. The red data point represents the lowest temperature synthesis of this series (120 °C) giving rise poorly formed jarosite, and this point is excluded in the data fit.

The data are limited in quantitative quality because of the high amount of fluorescence, short scan lengths and the collection of data at room temperature. Qualitatively the data are satisfactory especially when all the data points are shown together on one graph (Figure 7.5). It is likely the change along c axis occurs because of a contraction in the T-A-T sheeting across the 12 coordinate site, where the H_3O^+ unit resides in the A-site position.

Changes in synthesis conditions clearly affect the crystal structure, although the effects may appear slight in terms of lattice parameter differences, these changes affect the temperature for the spin glass transition. What structural changes are occurring are unknown from this powder diffraction data.

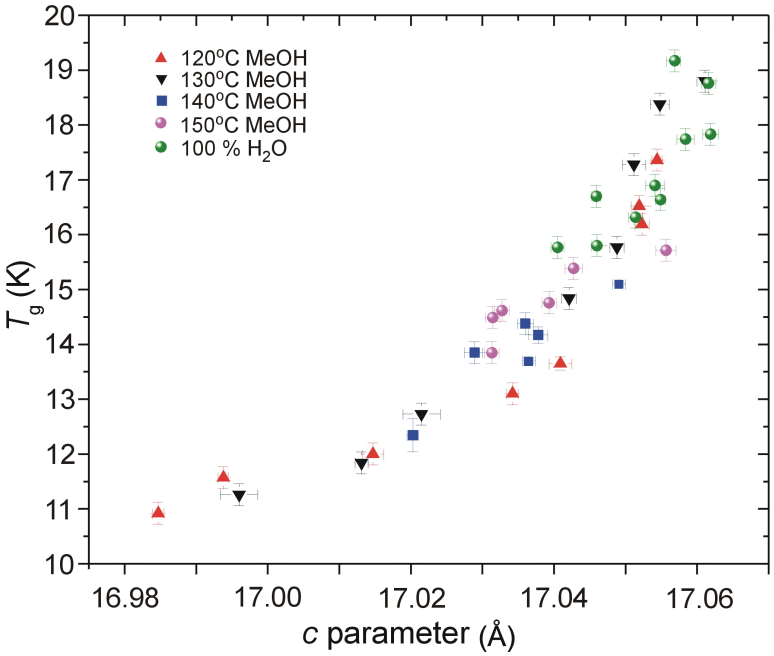

Figure 7.5: T_g plotted against the c parameter of the crystal structure for all hydronium jarosites shown in Tables 7.1 and 7.2. A clear structural change is occurring shown by an overall contraction along c whilst T_g decreases.

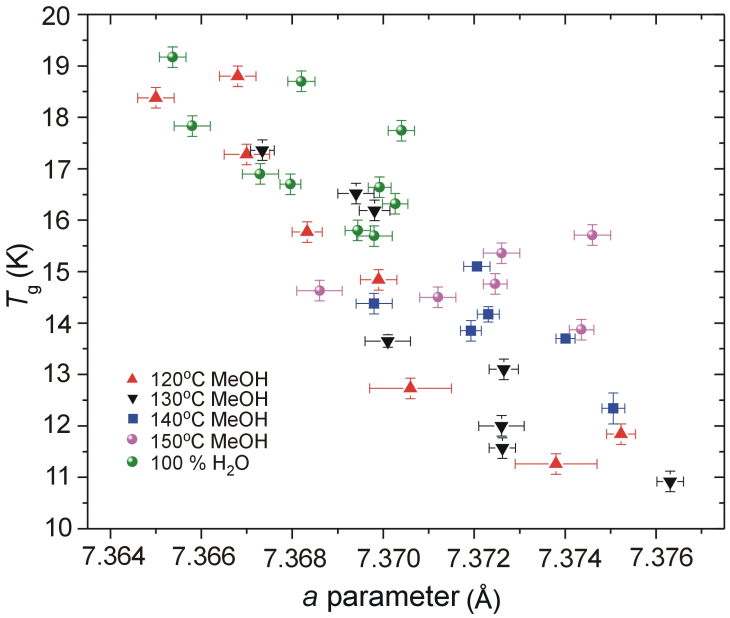

Figure 7.6: T_g plotted against the a parameter for all hydronium jarosites shown in Tables 7.1 and 7.2. It shows a structural change is occurring which causes an overall expansion along a that gives rise to a corresponding decrease in T_g. This highlights a trend only as the distribution in the a axis widens as T_g decreases.

The change in the a lattice parameter for the different samples shows a similar change this time. An expansion in the a axis correlates reasonably with a decrease in T_g as shown in Figure 7.6. The change in the a lattice parameter is opposite to the change in c with decreasing values of T_g. Changes in c with different B-site ions has been previously studied; the *kagomé* layers interpenetrate greater across the 12 coordinate A-site for Fe jarosite than compared to Ga jarosite or alunite [10,22,161]. Such interpenetration may give rise to a subsequent expansion in a.

7.3 Lattice parameters for potassium jarosites

Lattice parameter data, shown in Table 7.3, were obtained for some potassium jarosites synthesised under forced hydrolysis conditions which allowed for variations in the A-site occupation between K^+ and $(H_3O)^+$.

Table 7.3: Table showing the synthesis conditions, lattice parameters and magnetic characterisation for potassium jarosite samples with differing concentrations of K^+ present. The samples were powder only and the lattice parameter data were collected at room temperature. T_C is the Néel temperature and θ_W is the Curie−Weiss temperature.

Synthesis		Lattice parameters (Å)		Magnetic characterisation (K)	
Sample	K^+ (M)	a	c	T_C (± 0.2 K)	θ_W($\pm$100)
KFe4	0.148	7.3274(5)	17.2110(12)	(64.2), 50.3	−1420
KFe1	0.202	7.3228(3)	17.2409(9)	64.5, 45.0	−1485
KFe2	0.300	7.3242(3)	17.2349(10)	N/A	N/A
KFe3	0.339	7.3206(3)	17.2338(9)	64.2	−1465

The data show how significant competition between the K^+ and the $(H_3O)^+$ ions into the A-site results in an increase for the c lattice parameter and conversely a decrease in the a parameter with increasing K^+ content.

7.4 Summary of lattice parameters investigations

The powder X-ray diffraction data show that there is a clear relationship between the value of the c-axis parameter and T_g: large values of c correspond to high spin-glass freezing temperatures. The associated changes in the a parameter are weaker. As decreasing T_g relates to a decrease in c and an increase in a, the magnetic transition appears to be due to a specific property of the crystal structure. This will be discussed further in Chapter 8.

Chapter 8

Single Crystal Studies

To further investigate the crystallographic changes described in the previous chapter more detailed analysis of the crystal structure was required; this chapter concentrates on single crystal studies enabling structural changes between chemically and structurally similar Fe-jarosite samples to be measured.

The technique for data collection, structure solution and refinement are outlined in Chapter 3, Section 3.7. The final crystal structures included refinements for all atomic positions and anisotropic displacement factors for all atoms. The exceptions are: the hydrogens on the hydroxyl group were refined with isotropic temperature factors only, and the hydrogens on the H_3O^+ ion could not be located. All the positions are fully occupied unless otherwise specified. The X-ray single crystal studies are to look for structural changes brought about by the cation residing in the A-site, and because of the results from the ICP-OES analysis have shown that the Fe occupancies range from $\sim 95\%$ to full occupation, the occupancies of the Fe, OH, $(H_3O)^+$ were set to full occupation and possible H_2O units were ignored. As shown in the previous chapters, the A-site cation influences the magnetism.

Data were collected at two sources, Southampton University (laboratory source) and Daresbury SRS (synchrotron source). Single crystal data were collected at Southampton for the large and more uniform crystals, whereas smaller samples were studied at the SRS (Daresbury). Data collected on samples below 85 K were also obtained at the SRS, where data could be collected as low as ~ 15 K.

Table 8.1 shows derived parameters and statistics for many of the samples investigated and presented in this chapter and are provided as CIF format in the accompanying CD.

Table 8.1: Bond angles and distances for many of the samples used in this project. All the data presented here were collected at Southampton University at $\sim 85\,\mathrm{K}$ apart from KFeMIT11, which was collected SRS at $\sim 85\,\mathrm{K}$. P1 refers to where intensities have been extracted in primitive and merged to trigonal later in SHELX. Two new parameters ϕ and Δ are listed, these are introduced further in this chapter.

Sample ID	total No. measured I	No. indep. reflections	residual $e\rho$ rms	R (%) factor	wR (%) factor	crystal size face (mm)	R (%) merge	V ($\mathrm{Å}^3$)	
H3OFe024(P1)	3421	255	0.142	2.37	6.06	0.08	2.4	792.46(2)	
H3OFe029	1051	252	0.111	2.29	5.40	0.04	2.5	789.7(2)	
H3OFe044(P1)	2737	253	0.129	2.55	5.67	0.03	3.6	790.68(7)	
H3OFe049(P1)	3134	255	0.127	2.38	5.81	0.04	2.7	790.99(4)	
H3OFeS10	3616	249	0.097	2.01	4.93	0.03	5.4	789.27(4)	
H3OFeS11	2045	253	0.190	2.96	5.70	0.05	2.8	789.6(2)	
H3OFeS15	1952	252	0.198	3.43	9.19	0.05	4.1	786.7(2)	
H3OFeS22	1301	247	0.283	4.38	10.36	0.04	4.1	789.6(2)	
H3OFeS24	1046	250	0.217	2.93	7.17	0.04	4.0	786.3(2)	
H3OFeS27(P1)	2913	256	0.173	3.28	8.26	0.05	2.6	789.96(4)	
H3OFeS33(P1)	2566	258	0.140	2.65	6.29	0.03	4.1	789.56(6)	
KFeMIT11	2327	297	0.084	1.76	4.55	0.04	N/A	789.01(15)	
NH4FeMIT	3406	264	0.140	2.39	5.93	0.05	5.3	811.6(4)	
NaFeMIT	3655	244	0.107	1.86	4.96	0.12	3.4	771.9(3)	
RbFeMIT	3239	266	0.197	2.16	5.70	0.10	4.9	818.1(4)	
AgFeMIT	3622	245	0.151	2.48	5.69	0.10	4.5	766.2(3)	
PbFe - BM1966, 403	11461	506	0.187	2.01	4.88	0.08	5.1	1556.65(14)	
Sample ID	a (Å)	c (Å)	Fe-O_{ap} (Å)	Fe-O_{eq} (Å)	Fe-O-Fe angle (°)	Fe-Fe (Å)	ϕ angle (°)	Δ	T_g (K) ± 0.2K
H3OFe024	7.3494(1)	16.9411(4)	2.0402(19)	1.9942(9)	134.24(12)	3.6747(1)	20.82(16)	0.0225(10)	15.6
H3OFe029	7.3358(9)	16.944(3)	2.0377(18)	1.9900(8)	134.31(11)	3.6683(4)	20.78(17)	0.0234(10)	17.7
H3OFe044	7.3379(4)	16.9561(8)	2.039(2)	1.9907(10)	134.30(14)	3.6690(2)	20.79(20)	0.0237(11)	18.0
H3OFe049	7.3425(2)	16.9416(6)	2.0396(18)	1.9926(9)	134.20(12)	3.6713(1)	20.87(17)	0.0230(10)	15.8
H3OFeS10	7.3357(2)	16.9361(6)	2.0377(17)	1.9894(9)	134.40(12)	3.6679(1)	20.74(16)	0.0237(9)	18.4
H3OFeS11	7.3384(10)	16.931(3)	2.0373(19)	1.9903(9)	134.38(12)	3.6692(5)	20.78(18)	0.0231(10)	17.2
H3OFeS15	7.3372(10)	16.875(3)	2.035(3)	1.9923(12)	134.06(15)	3.6886(5)	20.90(22)	0.0210(16)	12.1
H3OFeS22	7.3344(9)	16.950(3)	2.038(3)	1.9904(11)	134.21(15)	3.6672(3)	20.85(20)	0.0234(16)	16.6
H3OFeS24	7.3304(10)	16.896(3)	2.0335(3)	1.9892(9)	134.23(12)	3.6656(5)	20.75(18)	0.0218(5)	14.1
H3OFeS27	7.3467(2)	16.9002(5)	2.038(3)	1.9959(15)	133.9(2)	3.6734(1)	20.93(31)	0.0207(17)	11.6
H3OFeS33	7.3373(2)	16.9349(10)	2.036(2)	1.9913(10)	134.19(14)	3.6686(1)	20.81(20)	0.0220(11)	13.7
KFeMIT11	7.2956(8)	17.117(2)	2.0610(12)	1.9803(6)	134.16(7)	3.6478(4)	20.10(11)	0.0392(7)	53.8, 62.5
NH4FeMIT	7.326(2)	17.461(4)	2.0600(19)	1.9872(9)	134.34(11)	3.6630(7)	20.36(17)	0.0353(10)	44.4, 61.0
NaFeMIT	7.328(2)	16.598(3)	2.0627(15)	1.9893(8)	134.12(9)	3.6647(7)	20.25(14)	0.0356(8)	N/A
RbFeMIT	7.326(2)	17.602(4)	2.0703(19)	1.9858(10)	134.53(12)	3.663(1)	20.21(18)	0.0408(10)	T_{N_2}, 63.4
AgFeMIT	7.333(2)	16.455(4)	2.041(3)	1.9857(13)	134.78(17)	3.6665(7)	20.59(22)	0.0271(16)	T_{N_2}, 59.3
PbFe -BM1966,403	7.3146(3)	33.595(2)	2.015(2)	2.0169(11)	133.04(14)	3.6998(7)	21.53(21)	0.0010(11)	N/A
($Pb_{0.45}Rb_{0.1}Fe_{2.91}$)			2.089(2)	1.9564(11)	134.99(16)	3.6148(9)	19.22(23)	0.0635(11)	N/A

8.1 Non-hydronium jarosites

Previous studies [3, 13, 14, 162, 163] had shown that the lattice parameters differ considerably between jarosite samples but there is no correlation with the size of the cation in the 12-coordinate A-site. Table 8.1 shows lattice parameters for a variety of jarosites. The non-hydronium jarosites display a wider range of lattice parameters between the possible A-sites and therefore an expectation of greater distortions to occur within the Fe octahedron. It is worthwhile to note, with reference to beaverite [13, 14] and all other alunite/jarosite systems [2, 3, 9, 10, 12, 14, 23, 50, 161–163], that changes in the A-site affects the c axis and deficiencies or substitution on the B-site affects the a axis; vacancies on the B-site result in an expansion along the a axis [2, 3, 13].

The lead jarosite structure [3, 13, 165, 166] is significant as it allows us to gather more information about the structural differences that might give rise to spin glass behaviour shown in hydronium and lead jarosites [164] which is discussed further in Section 8.3.

8.1.1 Structural information

Table 8.2 gives the crystallographic details for KFeMIT11 sample which was measured at the SRS as part of a thermo-diffraction study. The crystal structure is displayed in Figure 8.1 and shows the tilted Fe octahedra tethered by the rigid sulphate groups. The *kagomé* layers are separated by the A-site (K) which reside in the cavity where the Fe octahedra point away from each other. It is the angle of this canting of the Fe-octahedra around the A-site that is of primary interest, trying to relate the A-site cation with the magnetism displayed in the jarosites. In the jarosite structure the Fe, S and A-site reside respectively on the $2/m$, $3m$ and $\bar{3}$ symmetry sites, and as such these special positions help increase the precision for any crystallographic calculations involving these atoms.

Table 8.2: Single crystal data for potassium jarosite sample KFeMIT11. Data were collected at the SRS with an X-ray wavelength of 0.68930 Å at 85(2)K. Solved using Direct Methods and refined using SHELX-97 The space group is $R\bar{3}m$ with a unit cell of $a = b = 7.2956(8)$Å and $c = 17.117(2)$Å. The R value is 0.0169

Atom	x	y	z	Multiplicity/ Occupancy	U_{iso} (Å^2)	
K	0	0	0	3	0.0073(2)	
Fe	0	$\frac{1}{2}$	$\frac{1}{2}$	9 / 97.3(4)%	0.00236(15)	
S	$\frac{2}{3}$	$\frac{1}{3}$	0.02442(4)	6	0.0026(2)	
O(Fe_{apical})	-0.44397(10)	0.1121(2)	0.61306(6)	18	0.0051(3)	
O(S_{apical})	$-\frac{1}{3}$	$\frac{1}{3}$	0.72766(12)	6	0.0049(4)	
O($Fe_{equatorial}$)	-0.20606(10)	0.20606(10)	0.46873(7)	18	0.0054(3)	
H(OH)	-0.153(3)	0.153(3)	0.449(2)	18	0.019(8)	
			$U_{anisotropic}$ (Å^2)			
Atom	U_{11}	U_{22}	U_{33}	U_{23}	U_{13}	U_{12}
K	0.0079(3)	0.0079(3)	0.0061(4)	0.000	0.000	0.00394(14)
Fe	0.00152(19)	0.00189(17)	0.00354(18)	0.00003(5)	0.00006(10)	0.00076(9)
S	0.0026(2)	0.0026(2)	0.0027(3)	0.000	0.000	0.00131(12)
O(Fe_{apical})	0.0061(4)	0.0027(5)	0.0055(5)	-0.0007(4)	-0.00033(19)	0.0013(3)
O(S_{apical})	0.0059(6)	0.0059(6)	0.0029(8)	0.000	0.000	0.0029(3)
O($Fe_{equatorial}$)	0.0037(4)	0.0037(4)	0.0083(5)	-0.0007(2)	0.0007(2)	0.0014(5)

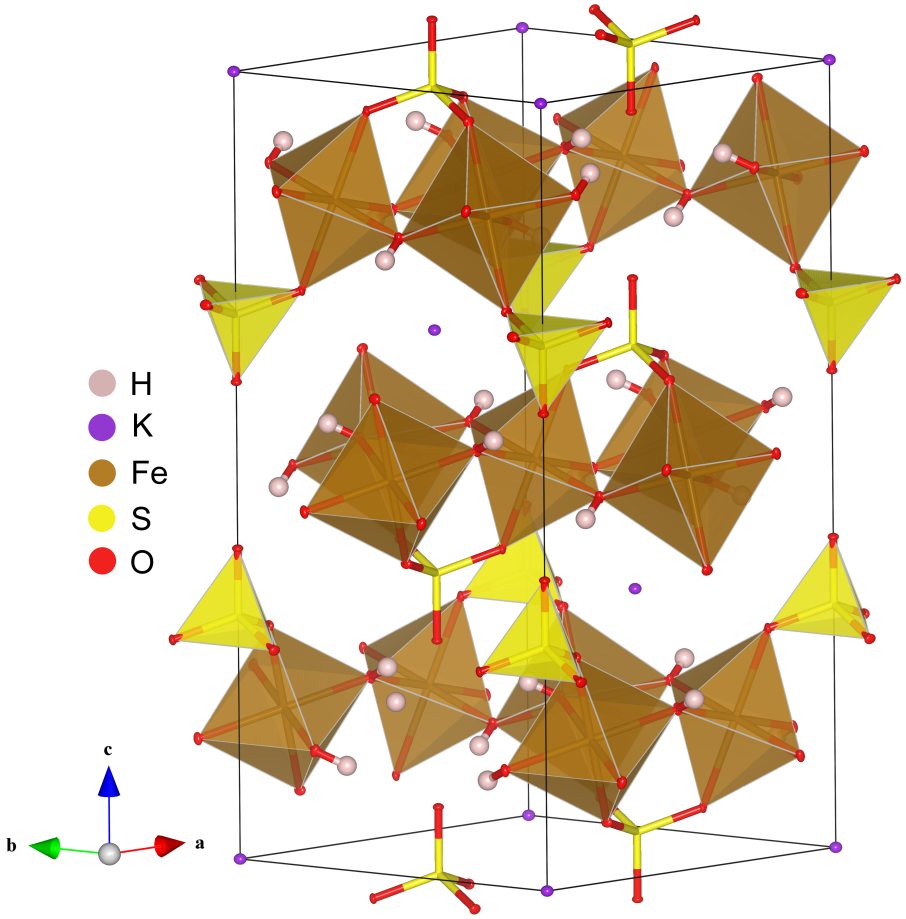

Figure 8.1: Polyhedra representation of potassium jarosite, KFeMIT11; the data were taken at the SRS at 85(2) K. The sulphate groups are shown by the yellow tetrahedra and the 6 coordination B-sites are shown by the brown octahedra. The hydroxyl groups bridge together the B-site Fe^{3+} ions to form the *kagomé* network, and oxygens from the sulphate groups above and below the *kagomé* plane complete the Fe coordination octahedra, which tilt away from being collinear with the c axis, leaving the A-site cation to occupy the 12 coordination cavity.

8.1.2 Discussion on crystal structure and elemental analysis

Previous research into jarosites suggests that, if present, Fe deficiencies are not significantly large; ∼97% Fe coverage for the hydronium jarosites [37, 167]; ∼99% for oxidative methods [20]. Though occupation can fall to ∼80% for jarosites not synthesised under hydrothermal conditions [14, 137]. Substitution with an appropriate cation on the B-site can occur still maintaining a very high B-site coverage [10,13,19]. As shown earlier (Section 6.3) the ICP-OES results indicate that the displayed magnetism is robust to deficiencies in the B-site where this may occur. As previously discussed in Chapter 6, B-site coverage is usually very high if not close to full oc-

cupancy. A-site coverage is also extremely high, though there is a much greater tolerance towards loss of the A-site ion because vacancies will always be assumed to be filled with the hydronium ion, $(H_3O)^+$ [3, 12]. The single crystal data collected on all the jarosites samples confirm the rigidity of the sulphate tetrahedron, it maintains its structure across the range of jarosites: the apical oxygen - sulphur bond length is ~ 1.463 Å and the equatorial oxygen - sulphur bond length is ~ 1.484 Å.

8.2 Hydronium jarosites

Initial investigations concentrated upon hydronium jarosite samples because many samples with different T_g and lattice parameters could be prepared, and many produced single crystals large enough for single crystal diffraction. Table 8.3 shows data for hydronium jarosite sample No. 24 (100% H_2O solvent, 150 °C) collected at Southampton University at 85(2) K, which provides an example of the data collected (giving atomic coordinates, Fe occupancy and anisotropic thermal parameters).

8.2.1 Measuring crystallographic changes

It is very difficult to ascertain a direct correlation between changes in the A-site coordination geometry and T_g; clearer correlations can be seen originating within the Fe octahedra. The Fe^{3+} ions have point symmetry $2/m$ as they reside on the $9d$ site of the space group and are coordinated by 4 hydroxyl oxygen atoms in the equatorial (eq) plane and 2 apical (ap) oxygen atoms from the sulphate groups as shown in Figures 8.2(a) and 8.2(b). The Fe octahedra are canted slightly out of the *kagomé* plane described by the deviation from collinearity with the c axis (Figure 8.2(a) shows the apical oxygen bond distance ($\sim$2.036 Å) which is slightly longer than the equatorial oxygen bond distance ($\sim$1.989 Å)). The first noted structural change correlating with T_g and the Fe coordination was the collinear angle ϕ: the measure of tilt the Fe octahedra makes with the c axis. As the angle ϕ becomes smaller it corresponds to the orientation of iron octahedra becoming more co-planar with respect to the *kagomé* plane as shown in Figure 8.2(c): a pictorial representation of angle ϕ which is the angle the Fe-O_{axial} bond makes with respect to the c axes.

Angle ϕ was determined firstly by calculating the distance, r, between the iron and axial oxygen in the ab plane, represented in Figure 8.2(c). The difference in z fractional coordinates between the iron and axial oxygen gave the length along the c axis and the equation (8.1) was determined to calculate ϕ.

Table 8.3: Single crystal data for hydronium jarosite sample No. 24. Data were collected at Southampton University with Mo K_α radiation at 85(2) K. Solved using Direct Methods and refined using SHELX-97 The space group is $R\bar{3}m$ with a unit cell of $a = b = 7.34940(10)$ Å and $c = 16.9411(4)$ Å. The R value is 0.0229.

Atom	x	y	z	Multiplicity/ Occupancy	U_{iso} (Å^2)
$O(H_3O)$	0	0	0	3	0.0236(14)
Fe	$\frac{1}{2}$	$\frac{1}{2}$	0	9 / 97.8(6)%	0.0052(2)
S	$\frac{2}{3}$	$\frac{1}{3}$	0.14193(6)	6	0.0042(3)
$O(Fe_{apical})$	0.55692(16)	0.44308(16)	0.11254(11)	18	0.0077(5)
$O(S_{apical})$	$\frac{2}{3}$	$\frac{1}{3}$	0.2282(2)	6	0.0083(7)
$O(Fe_{equatorial})$	0.20584(17)	0.4117(3)	0.03157(13)	18	0.0097(5)
H(OH)	0.155(4)	0.310(7)	0.053(3)	18	0.023(13)

	$U_{anisotropic}$ (Å^2)					
Atom	U_{11}	U_{22}	U_{33}	U_{23}	U_{13}	U_{12}
$O(H_3O)$	0.026(2)	0.026(2)	0.019(3)	0.000	0.000	0.0129(10)
Fe	0.0061(3)	0.0061(3)	0.0047(3)	0.00062(9)	-0.00062(9)	0.0040(2)
S	0.0052(4)	0.0052(4)	0.0023(5)	0.000	0.000	0.0026(2)
$O(Fe_{apical})$	0.0108(7)	0.0108(7)	0.0056(8)	0.0003(3)	-0.0003(3)	0.0084(8)
$O(S_{apical})$	0.0117(11)	0.0117(11)	0.0015(14)	0.000	0.000	0.0059(5)
$O(Fe_{equatorial})$	0.0044(7)	0.0052(11)	0.0199(11)	0.0064(9)	0.0032(4)	0.0026(5)

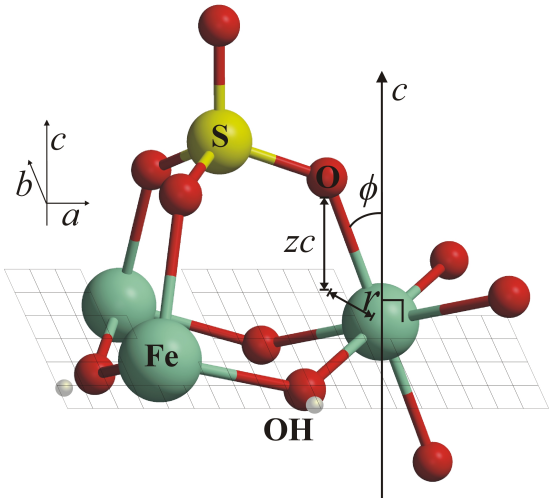

(a) Knowledge of r and the distance between Fe and O in the z direction gives us the collinear angle ϕ. Length $r = xa\sqrt{3}$ and is graphically represented in c)

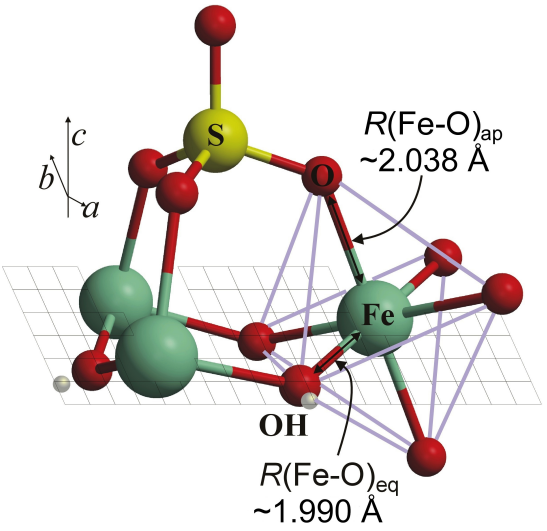

(b) A graphical description of the Fe octahedra showing deviation from perfect octahedral symmetry. The apical bond (ap) is slightly longer than the equatorial bond (eq).

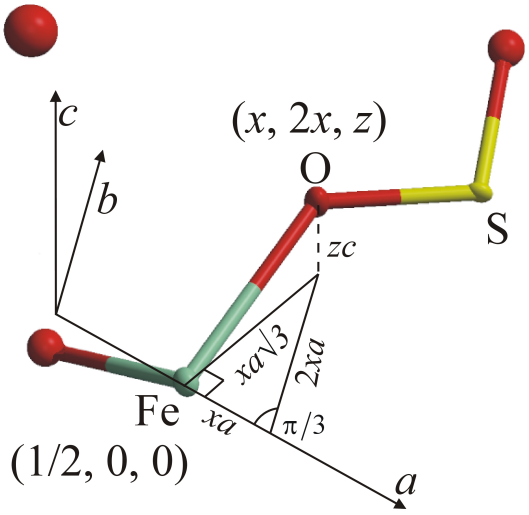

(c) Graphical derivation of length $r = xa\sqrt{3}$

Figure 8.2: a) and b) show two pictorial representations of the slight crystallographic distortions centred around the Fe octahedra. a) is the tilt of the Fe octahedra away from collinearity with the c axis and b) is the distortion of the Fe coordination octahedra away from perfect octahedral symmetry. c) is a graphical derivation of length $r = xa\sqrt{3}$ which is the distance between the iron and the axial oxygen in the ab plane. The calculation was simplified by the oxygen residing in the Wyckoff site 18h - x,2x,z.

$$tan\phi = \frac{\sqrt{3}a|x_{Fe} - x_O|}{c|z_{Fe} - z_O|}. \tag{8.1}$$

8.2.2 Results - collinear angle

Angle ϕ was plotted against T_g for all hydronium jarosite samples where single crystal data were obtained (Figures 8.3(a) and 8.3(c)). Figure 8.3(a) shows data sets collected at $\sim$ 85 K and Figure 8.3(c) shows data collected at 15(2) K. There is a relationship between the angle of tilt of the Fe octahedron out of the *kagomé* plane and the spin-glass freezing temperature. The greater the tilt, the lower the value for T_g. The error bars for the angle are large and for such a close spread of T_g values, angle ϕ is probably not suited as measure of the Fe-octahedron conformation for the hydronium jarosites.

Figures 8.3(b) and 8.3(d) show extrapolations of this relationship to include two non-hydronium jarosite samples, KFeMIT11 and NH4FeMIT, whose data were collected at SRS and Southampton respectively at $\sim$ 85 K. The non-hydronium jarosites are plotted with two magnetic transitions, the higher temperature value is T_{N_1} and the lower is T_{N_2}. The crystallographic data collected at $\sim$ 85 K show the possibility of the relationship extending to T_{N_2}. Plotting the angle ϕ values collected at 15(2) K near to T_g for the hydronium jarosites and 50(2) K for KFeMIT11 close to $T_{N_2} = 51.7$ K, does show there is relationship between the tilt of the Fe-octahedron and the magnetic transitions within all the Fe-jarosites. Unfortunately only sample KFeMIT11 had data collected at a range of temperature that included T_{N_1} and T_{N_2}, this is presented later in this chapter. The extrapolations clearly suggest there is an overall relationship within all the jarosites, but a better measure is required to reduce the spread and associated error bars of the data points. Another crystallographic parameter is needed too further confirm the relationship between the Fe-octahedron coordination and the temperature of the magnetic transitions and to utilise the quantity of crystallographic data collected at $\sim$ 85 K.

Using angle ϕ as a measure, it can be seen that the more collinear the orientation of the Fe octahedra with the c axis, the higher the transition temperature, T_g which looks likely to correspond with T_{N_2} of the non-hydronium jarosites. This suggests the presence of an anisotropy resulting from changes in the crystal structure giving rise to a single ion anisotropy or the Dzyanloski-Moryia interaction as previously discussed in Section 2.6.3.

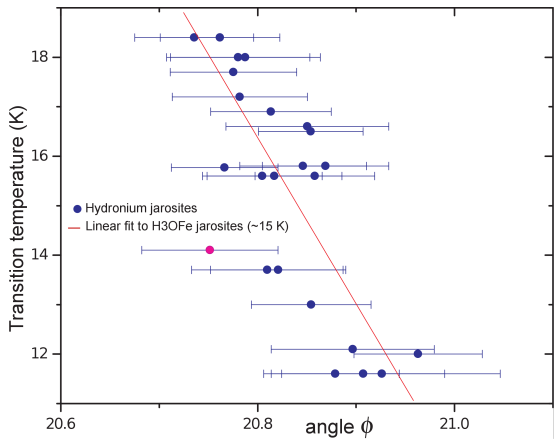

(a) Plot showing a reasonable relationship between angle ϕ and T_g for the hydronium jarosites. The data were collected at $\sim 85\,K$ at both Southampton and SRS. Data point in pink has been ignored from the linear fit.

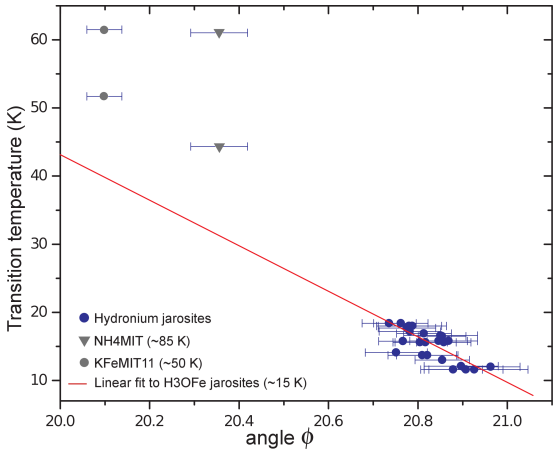

(b) The relationship in a) has been extended to see whether it extrapolates to include non-hydronium jarosites whose data were collected at $\sim 85\,K$.

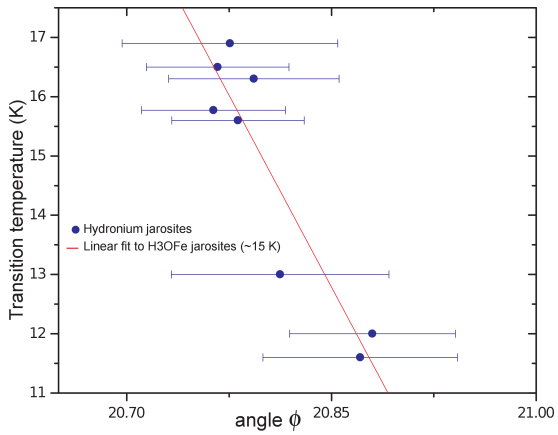

(c) Plot showing the relationship between angle ϕ and T_g for the hydronium jarosite data collected at $\sim 15\,K$ at the SRS.

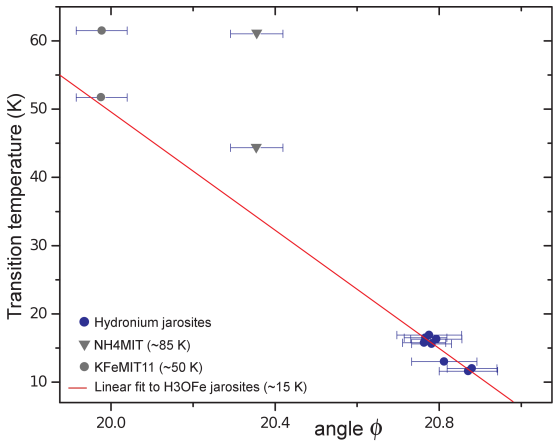

(d) The relationship in c) has been extended to see whether it extrapolates to include non-hydronium jarosites. The ϕ value for KFeMIT11 was collected at 50 K and the relationship does extend to include $T_{N_2} = 51.7\,K$.

Figure 8.3: Plots a) and b) show the relationship between ϕ and T_g for crystallographic data collected at $\sim 85\,K$ from Southampton and SRS. Plot b) shows an extrapolation of this relationship to see whether it extends to include ϕ values, also collected at $\sim 85\,K$, for transitions, T_{N_1} and T_{N_2}, for samples KFeMIT11 (●) and NH4FeMIT (▼). The relationship does not extend to the non-hydronium jarosites. Plots c) and d) plot ϕ data collected at the SRS at very similar temperatures to T_g ($\sim 15\,K$) or T_{N_2} ($\sim 50\,K$) for the samples shown, except for NH4FeMIT where ϕ was only collected at $\sim 85\,K$ at Southampton. Plot d) shows the extrapolation of the relationship between ϕ and T_g for the hydronium jarosites does extend to include T_{N_2} for the non-hydronium jarosites.

8.2.3 Bond ratio measurements

There are problems using ϕ as a measure of collinearity of the Fe octahedron with the c axis. First, ϕ requires several parameters to calculate, including the larger quantities of the lattice parameters and the associated e.s.d.'s in comparison to the smaller quantities of the atomic positions. Single crystal data lacks the resolution needed for lattice parameter determination to reduce the error in ϕ. Second, the Fe octahedron has a point group of $2/m$ and is therefore not a regular octahedron and measuring ϕ does not necessarily account for changes within the octahedron; the bonds between the Fe and oxygen atoms in the apical and equatorial planes are different in length. X-ray single crystal diffraction data collected at $\sim$ 85 K from hydronium jarosites showed the equatorial bonds, Fe–O–Fe, are shorter with a variation in length between 1.988–1.994 Å. The apical Fe–O(–S) bonds are slightly longer with a similar variation in lengths, 2.034–2.040 Å. Therefore, a better measure and a more accurate approach, with no account of lattice parameters, was to take the ratio of these bond lengths and plot this against T_{g} as shown in Figure 8.4(a). It shows as the bond ratio approaches 1 (closer to O_h symmetry) then the lower T_{g} becomes.

Instrumental differences

The ratio of the Fe-O bond lengths that make up the octahedron gives a much smaller value in comparison to ϕ and as such highlighted differences between the instrumentation where the data were collected. Each instrument showed similar correlations between the bond ratio and T_{g}, however, the two data sets could not be merged together (Figure 8.4(a)), unlike the data for ϕ, even though more data sets were collected at $\sim$ 85 K.

Figure 8.4(a) displays all the data sets collected at Southampton (laboratory data) and SRS (synchrotron data) at 85 K taking the bond length ratio between the Fe–O equatorial and the Fe–O apical. The results once again show a correlation between Fe coordination octahedra and T_{g}: the more symmetrical the Fe octahedra the lower the value for T_{g}. This suggests that the greater the distortion away from $\mathrm{O_h}$ symmetry the greater anisotropy and raising of the magnetic transition temperature, and underpins that it is a anisotropy driven spin glass freezing transition.

Figure 8.4(a) shows the differences between the two instruments which could not be reconciled for the hydronium jarosite samples. One attempt at Southampton

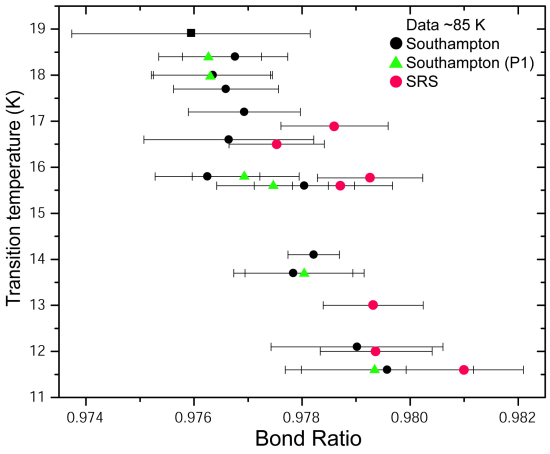

(a) Measuring the bond ratio shows up the differences between the two X-ray sources, laboratory and synchrotron, collected at $\sim 85\,\mathrm{K}$.

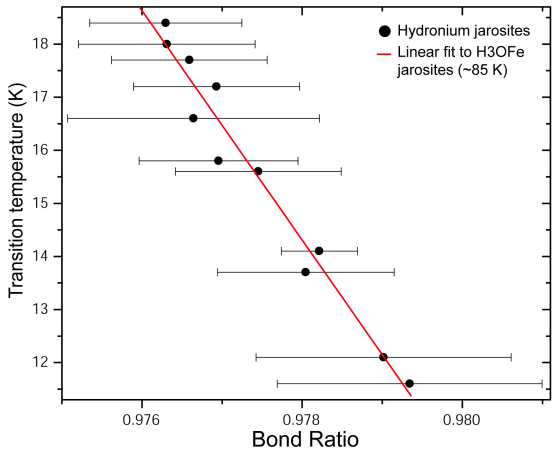

(b) The bond length ratio taken between the equatorial and the apical oxygens bonding to the Fe^{3+} ions from data collected only at $\sim 85\,\mathrm{K}$ at Southampton.

Figure 8.4: Plot a) combines data collected from the SRS (●) with a wavelength of 0.6768 Å and Southampton data where the integrated intensities were either collected and merged in the trigonal crystal system (●) or collected in primitive and later merged within SHELX (▲). Collecting intensities in P1 for the Southampton data did help to slightly improve the final refinement for some data sets, which in turn modestly changed the bond ratio. b) shows a good correlation exists between the distortion of the Fe coordinated octahedra and the spin glass freezing temperature, T_g for the data only collected at Southampton at $\sim 85\,\mathrm{K}$. Both plots show the more distorted the Fe octahedra the higher value for T_g.

was to collect intensities from $\frac{1}{2}$ of reciprocal space then allow SHELX to carry out the merging into the trigonal crystal system. This aided the refinement for some of the jarosite crystal data collected at Southampton. There were several differences between the data sets from these sources: more *hkl* reflections from the SRS had to be omitted from the refinement process due to some very high $F\sigma^2$ values; many data sets collected at SRS returned R1 values above 3% - the deemed acceptable threshold for hydronium jarosites due to their relative high symmetry, compact structure and good scattering potential; there were $\sim$ 231 independent reflections collected at the SRS compared to $\sim$ 224 at Southampton. Simply, the much smaller crystals used at the SRS had large scatter occurring. It was decided upon for consistency that data taken from Southampton would only be used towards the bond ratio study. This might be contrary to expectation choosing laboratory sources over synchrotron, however, jarosite crystal growth is a thermodynamic process via the Ostwald mechanism [16], larger crystals perhaps will be greater in quality than smaller, not fully ripened crystals.

8.2.4 Results - bond ratio

Figure 8.4(b), displays data collected only from Southampton, presents a clearer correlation of the distortion of the Fe octahedra with T_g. Greater distortion away from O_h symmetry correlates with higher spin glass freezing transitions. It may, therefore be concluded that this provides the anisotropy energy scale required to induce a critical spin-glass transition.

A new parameter was created at the suggestion of Michel Gringras of a distortion parameter, $\Delta = 1 - [\mathrm{r(Fe\text{-}O)_{axial}}/\mathrm{r(Fe\text{-}O)_{equatorial}}]$. Δ would therefore be zero for isotropic bonding. Larger values of the distortion parameter, Δ were found to correlate with higher spin glass freezing temperatures which is shown in the upper graph of Figure 8.5.

The transition is critical because the small anisotropy provides a sharp crossover from a system with no defects to one with a number of defects. It does this by creating an energy barrier to the reorientation of moments out of the *kagomé* plane, thereby leading to an increase in spin stiffness producing defects where the spin folds intersect.

Extrapolation of the relationship between Δ and T_g allows comparison of the hydronium jarosites with these that show Néel order. This is done for the K^+ and NH_4^+ jarosites in Figure 8.6. The excellent agreement with the values of the T_{N_2} for these samples indicates that the distortion of the Fe octahedron is again definitive in this transition.

Conclusions

Two measures of the conformation of the Fe-octahedron have both highlighted a good correlation within the hydronium jarosites samples between Fe-conformation and the spin-glass freezing temperature and this has been successfully extended to encompass two non-hydronium samples, KFeMIT11 and NH4FeMIT.

The similar values of T_{N_1} of $\sim$ 60-65 K for the non-hydronium jarosites, and as shown in both Figures 8.3(d) and 8.6, T_{N_1} is independent of this relationship which indicates that this transition is affected by another interaction. The differing types of magnetic order in the hydronium and non-hydronium jarosites may therefore be defined by another, stronger, energy scale. The DMI, allowed in the jarosites, is likely possibility and that both crystal field effects and DMI co-exist.

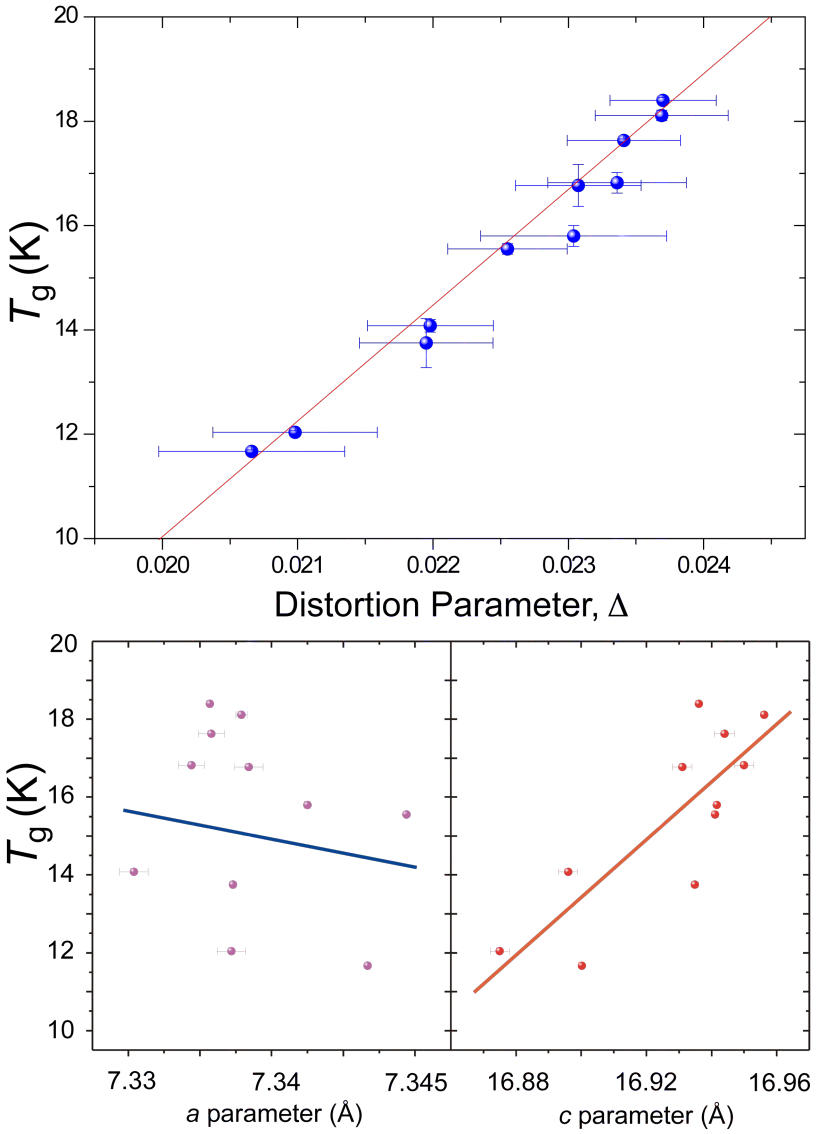

Figure 8.5: The upper graph shows the correlation between the distortion and spin glass transition temperature. The error bars shown are the e.s.d.'s from the Fe-O equatorial bond distance. The distortion is described as a distortion parameter, Δ: the difference between 1 and the bond ratio. The greater the distortion the higher the value of T_g. The strong linear correlation suggests that the anisotropy responsible for the spin glass transition is proportional to the extent of the distortion. The bottom two graphs confirm the results obtained from powder diffraction: there is a correlation between compression in the c axis and increasing T_g; but no relationship is discernible from changes within the a axis. The data shown here were collected at Southampton at $\sim 85\,\mathrm{K}$.

8.3 Pb jarosite

The lead jarosite features a $R\bar{3}m$ structure that is doubled along the c-axis, with respect to the jarosites. For this reason two values of ϕ are presented in Table 8.1.

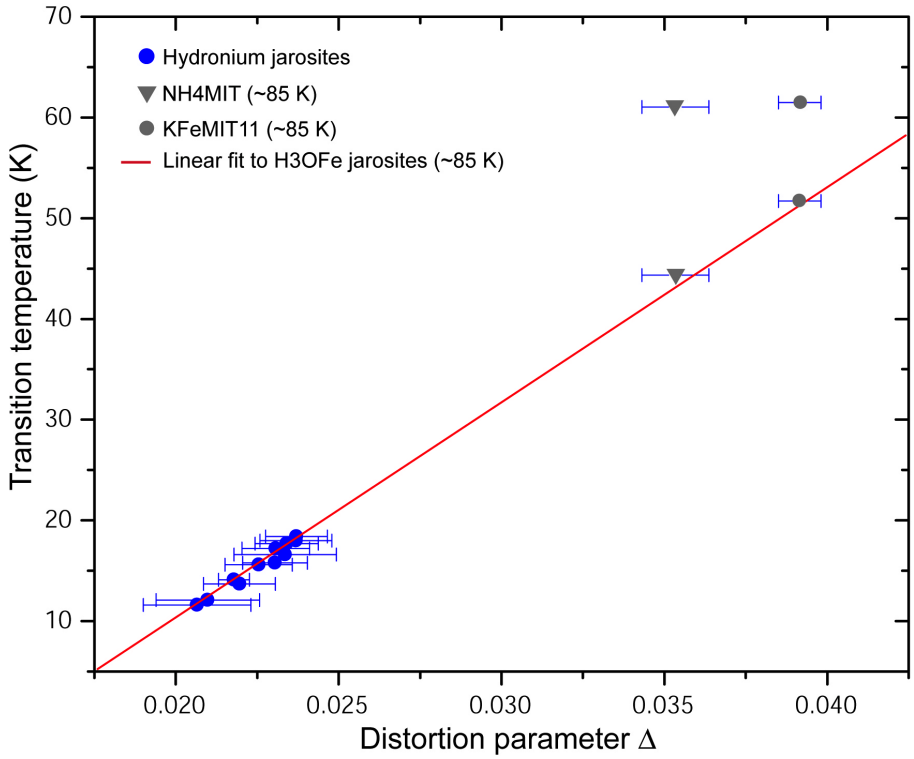

Figure 8.6: The measurement of the deviation from octahedral symmetry is a measure of the increase in anisotropy present. The greater the distortion the higher the value for T_g. The approximately linear correlation suggests that the anisotropy responsible for the spin glass transition is proportional to the extent of the distortion and that the same linear function fitted for hydronium jarosite can be extended to the antiferromagnetic Néel ordering temperatures of $KFe_3(SO_4)_2(OH)_6$ (●) and $(NH_4)Fe_3(SO_4)_2(OH)_6$ (▼). There are two data points for the non-hydronium jarosites samples, representing T_{N_1} and T_{N_2}. The values for T_{N_2} are those that fall upon the extension to the linear fit shown by the red line. The error values are 1σ for Δ taken from both Fe-O bond lengths.

This doubled structure has one crystallographic Fe position at $x, 2x, z$ site with point symmetry m. There are correspondingly 6 layers of vertex sharing Fe^{3+} ions with the bridging equatorial oxygens on the same site symmetry position, m, at $x, 2x, z$. The crucial point that arises from this, is that the vertex network is now made up of equilateral triangles alternating in size. The structure remains in the $R\bar{3}m$ space group and the Pb is segregated in alternate T-A-T layers.

Pb jarosite structural details

In the natural sample studied the less than full occupancy of Pb^{2+} requires the inclusion of other cations for charge balancing. It was found that oxygen on the other $\bar{3}m$ site did not provide enough electron density and the following cations

Table 8.4: Single crystal data for natural lead jarosite sample (BM1966, 403). Data were collected at Southampton University with Mo X-ray radiation at 80(2) K. Solved using Patterson methods in $R\bar{3}$ and refined using SHELX-97. The space group is $R\bar{3}m$ with a unit cell of $a = b = 7.3146(3)$ Å and $c = 33.595(2)$ Å. The R value is 0.0197. The occupancies give the following formula $Pb_{0.45}Rb_{0.1}Fe_{2.91}(SO_4)_2(OH)_{5.73}(H_2O)_{0.27}$.

Atom	x	y	z	Occupancy	site symmetry	U_{iso} (Å^2)
Pb	0	0	0	0.892(5)	$\bar{3}m$	0.01031(14)
Rb	0	0	$\frac{1}{2}$	0.186(6)	$\bar{3}m$	0.0185(19)
Fe	0.16860(3)	0.33721(7)	0.084157(12)	0.969(5)	m	0.0042(2)
S1	0	0	0.15482(4)	1	$3m$	0.0056(4)
S2	$\frac{1}{3}$	$\frac{2}{3}$	0.01027(4)	1	$3m$	0.0053(4)
O1	0.0000	0.0000	0.19837(12)	1	$3m$	0.0084(9)
O2	0.11024(19)	0.2205(4)	0.13994(7)	1	m	0.0086(6)
O3	0.4634(2)	0.5366(2)	0.09731(8)	1	m	0.0085(5)
O4	-0.1228(2)	0.1228(2)	0.06515(7)	1	m	0.0076(5)
O5	0.22288(19)	0.4458(4)	0.02545(7)	1	m	0.0074(6)
O6	$\frac{1}{3}$	$\frac{2}{3}$	-0.03322(13)	1	$3m$	0.0082(9)
H1	-0.155(5)	0.155(5)	0.2721(17)	1	m	0.026(15)
H2	0.158(5)	0.842(5)	0.226(2)	1	m	0.037(19)

	$U_{anisotropic}$ (Å^2)					
Atom	U_{11}	U_{22}	U_{33}	U_{23}	U_{13}	U_{12}
Pb	0.01107(16)	0.01107(16)	0.0088(2)	0.000	0.000	0.00553(8)
Rb	0.020(2)	0.020(2)	0.016(3)	0.000	0.000	0.0098(11)
Fe	0.0037(3)	0.0034(3)	0.0066(3)	0.00052(18)	0.00026(9)	0.00172(16)
S1	0.0047(5)	0.0047(5)	0.0072(7)	0.000	0.000	0.0024(2)
S2	0.0044(5)	0.0044(5)	0.0071(7)	0.000	0.000	0.0022(2)
O1	0.0099(13)	0.0099(13)	0.0054(19)	0.000	0.000	0.0049(6)
O2	0.0092(9)	0.0056(12)	0.0096(11)	0.0005(9)	0.0002(5)	0.0028(6)
O3	0.0070(9)	0.0070(9)	0.0114(12)	0.0013(5)	-0.0013(5)	0.0034(10)
O4	0.0060(8)	0.0060(8)	0.0115(12)	0.0006(5)	-0.0006(5)	0.0037(10)
O5	0.0073(9)	0.0041(12)	0.0098(11)	-0.0003(9)	-0.0001(4)	0.0020(6)
O6	0.0090(13)	0.0090(13)	0.0066(19)	0.000	0.000	0.0045(6)

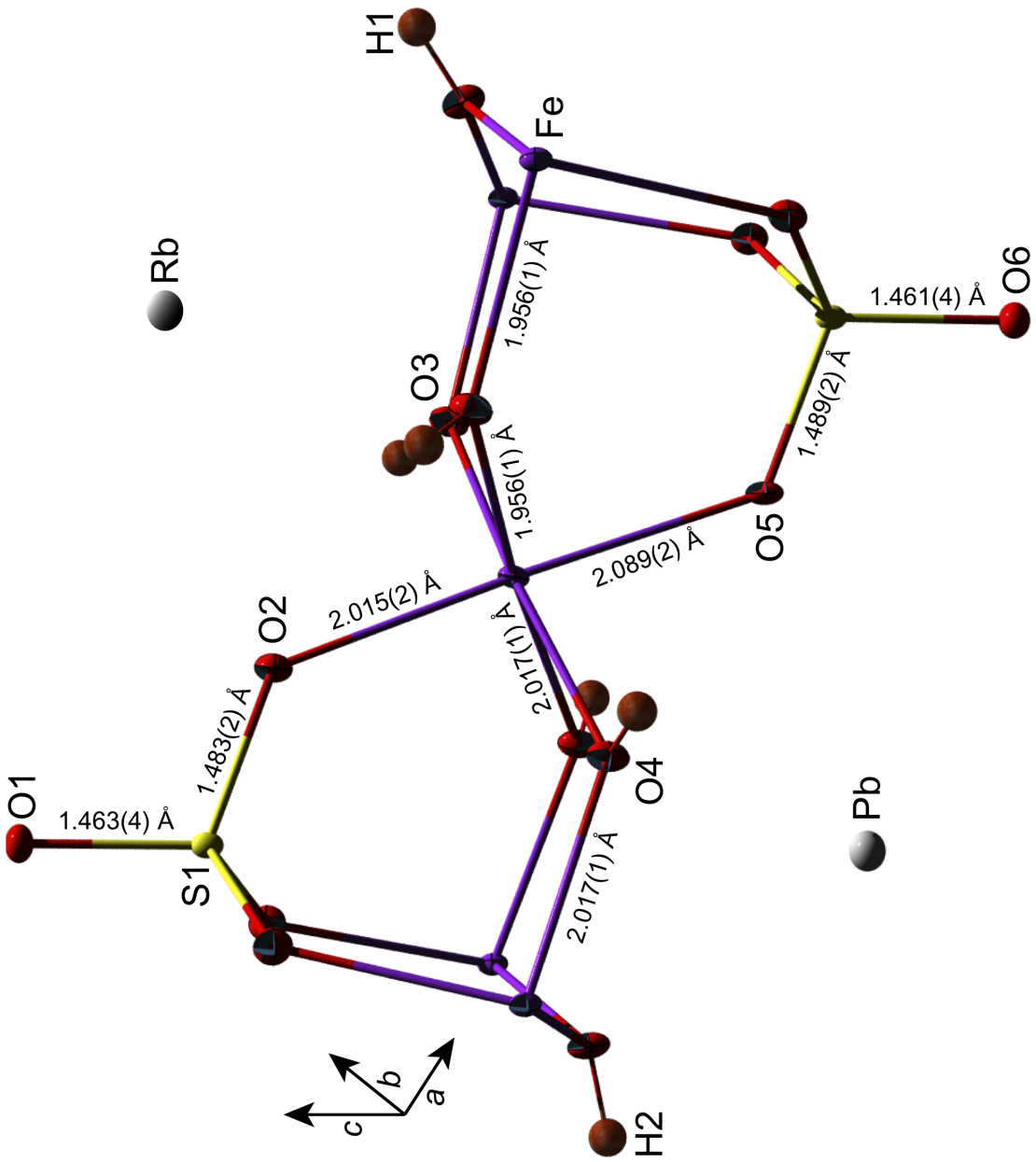

Figure 8.7: Ortep-III plot of natural lead jarosite (BM1966, 403). Space group is $R\bar{3}m$, with a unit cell of $a = b = 7.3146(3)$ Å and $c = 33.595(2)$ Å. There are two different conformations surrounding the Fe octahedra, each determined by the contents of the nearest A-site. This leads to two Fe–Fe distances, Δ and ϕ values.

were modelled in this available A-site: Na^+, K^+, Rb^+, Tl^+ and Pb^{2+}. The choice of cation made little or no difference to the atomic coordination of the cell contents, and the R factors too were very similar, ~ 0.0200. The Pb and Fe occupancy, irrespective of A-site cation, refine to a stoichiometric value of 0.446(5) and 2.907(6) respectively based upon the general formula: $Pb_{0.5}Fe_3(SO_4)_2(OH)_6$. This leaves a positive charge deficit of $\sim +0.1$ within the A-sites. The refined stoichiometric values for Na^+, K^+ over compensated for the charge deficit. Cations Tl^+ and Pb^{2+} refined to give the same occupation, but Tl^+ did not provide enough charge, whereas the small amount of Pb^{2+} on the alternate A-site, closely charge balances. The inclusion of Rb^+ does charge balance the A-sites best, with a stoichiometric value of 0.093(6). To be certain of the elements present and their quantities, elemental analysis will be necessary. The full structural details of lead jarosite are shown in Table 8.4 with the corresponding Ortep-III plot in Figure 8.7. The structure has been depicted with Rb in essence to show the segregation of the A-site in the doubled cell, a very small amount of Pb probably does reside in the other A-site as total segregation of Pb^{2+} ions may not be achieved.

8.3.1 A-site discussion

Lead jarosite shows again that the jarosite structure is remarkably robust. While the A-site cations are not included in the magnetic exchange, they do dictate the degree of distortion of the Fe-octahedron. Pb jarosite sample BM1966, 403 shows that the Fe octahedron in the Pb environment has little distortion away from O_h symmetry, $\Delta = 0.001(1)$, but is countered by a much more distorted Fe octahedra in the alternate A-site environment, $\Delta = 0.0636(11)$. In less segregated samples two transitions are noted, $T_C = 28$ and 42 K, and a separation in the ZFC and FC susceptibility, typical of a spin glass like transition [164]. It is difficult to speculate as to the reasons for this behaviour as it is not known whether the ordered and spin glass phases coexist or are segregated.

One argument for the long range magnetic ordering in the non-hydronium jarosites and spin glass like behaviour for hydronium jarosite is the involvement of remote hydrogen bonding [37]. This is unlikely as this discussion has shown the A-site has a direct influence on the crystals structure.

8.4 Conclusions for all jarosites

The data presented here and outlined in Table 8.1 clearly show that the A-site dictates the bond lengths, Fe–Fe intra-distance and the transition temperatures. Looking at the collinear angles, ϕ, shown in Table 8.1, the hydronium jarosite has the greatest deviation from collinearity with the c axis with the smallest values for Δ, suggesting the Fe-octahedron is the most relaxed within the hydronium jarosite structure and is the closest to O_h symmetry. The anisotropy present in the hydronium jarosites are presumed to be weaker because of the lower transitions temperatures and lack of Néel ordering compared to the non-hydronium jarosites.

It is still necessary to look for further evidence of the relationship between crystal structure and magnetism within the jarosite crystal structure.

8.4.1 Interpenetration of the A-site cavity

Investigating the interpenetration of the T-O-T sheets across the T-A-T layer, the layers are illustrated in Figure 8.8, is useful to see what the relationship between the 12 coordination site has with the Fe octahedron.

Measuring the distance along the z direction between a sulphate oxygen with site symmetry $3m$ across the T-A-T sheeting to another sulphate oxygen with site symmetry m gives the penetration into the T-A-T layer. Figure 8.9 shows the interpenetration of the T-O-T layers into the 12 coordinate site increases with decreasing T_{g}. The linear fit is reasonably good to indicate that the crystallographic change originates from the A-site, though the red data point highlights that with so many crystallographic permutations in the jarosite structure that there is not necessarily a single determinant which produces the changes seen. Considering the rigidity of the sulphate groups, the protrusion will expect to have a uniform effect down through into the Fe octahedra. The nature of the trivalent metal is therefore relevant. Studies of solid solution of Fe-jarosites and the Al-alunites [10, 50, 137, 161] show that the T-O-T distance in the jarosite is longer, but the overall c lattice parameter remains similar because the greater ability of the T-O-T sheets to interpenetrate each other within the jarosite structure [50]. Since the OH-OS is fixed $\sim 2.92\,\text{Å}$ for both alunite and jarosite [168], the different lengths of the Fe-OH and Al-OH bonds cause changes across the T-A-T layer. Studies of the lattice parameters of Ga^{3+} substituted Fe-jarosites indicate that the Fe^{3+} leads to greater interpenetration of the T-O-T sheets [10, 137].

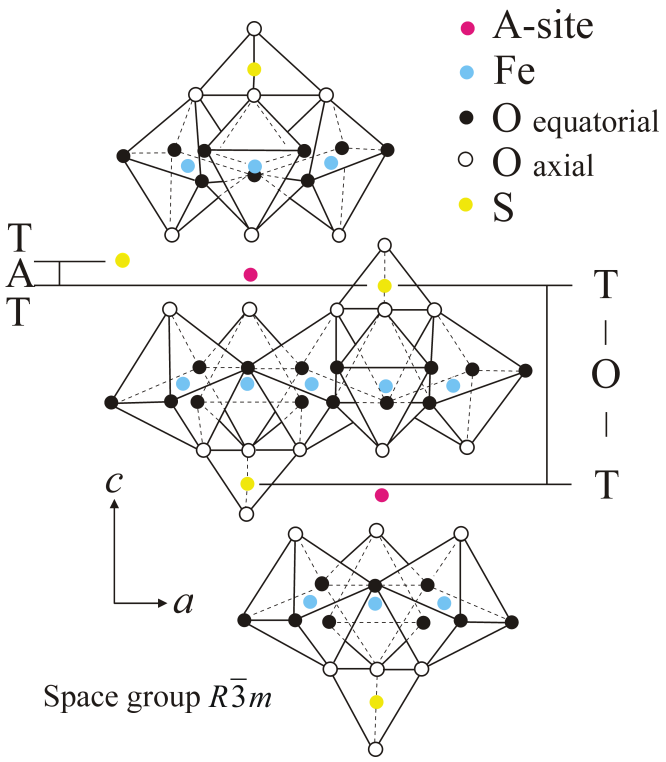

Figure 8.8: Polyhedra representation of the jarosite structure with a c axis unit cell of $\sim$ 17 Å, showing the two sheets that make up of the jarosite structure. The distance between the sulphate groups across the *kagomé* plane is the T-O-T sheet, this distance stays reasonably fixed and it is the small distance across the A-site that changes the most and determines the c parameter for the jarosites.

8.4.2 Thermo-diffraction study, SRS

A thermo-diffraction study was undertaken to measure the changes in ϕ as function of temperature. Data were collected at the SRS (Daresbury) by William Clegg and Ross Harrington using a helium cryostat to cool the sample down to 15 K. Data sets were collected at 15 K and 5 K intervals from 40 K to 75 K and 85 K. The sample used was the potassium jarosite sample, KFeMIT11, synthesised using the oxidative method. Figure 8.10 shows the plot of angle ϕ (■) with temperature superimposed upon the field cooled susceptibility (▲).

Data collected during the magnetic transitions shows angle ϕ changes, whereas, above and below the magnetic transitions it remains fairly stable. The lack of data points from this experiment does not allow us to draw any further conclusions as to the nature of the transition, but does demonstrate further that the crystal structure and the magnetism are intrinsically coupled.

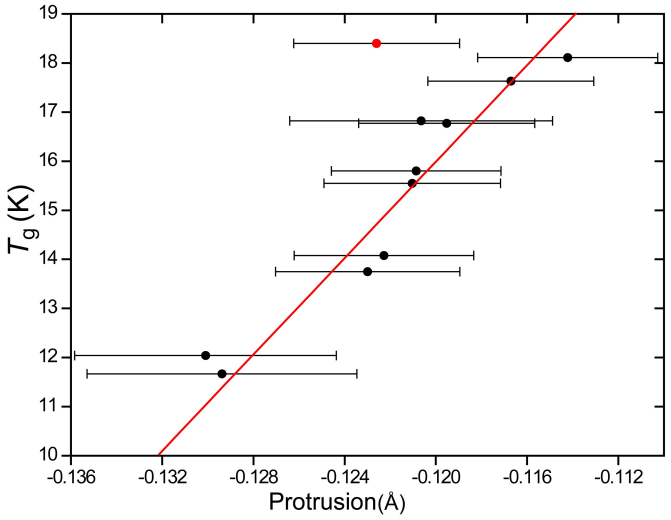

Figure 8.9: Plot of the interpenetration of the sulphate groups across the T-A-T layer within the hydronium jarosites using the Southampton data collected at $\sim$ 85 K. The sulphate protrusion measures the z distance between a sulphate oxygen with site symmetry $3m$ to a sulphate oxygen with m site symmetry on the opposite side of the T-A-T layer. There is a reasonable correlation between T_g and the sulphate protrusion: lower T_g the greater the interpenetration across the T-A-T layer. Protrusion is negative to produce a positive gradient. The red data point, with the highest T_g, and has been ignored from the linear fit. The error bars are a 1σ for the z atomic position of the oxygens.

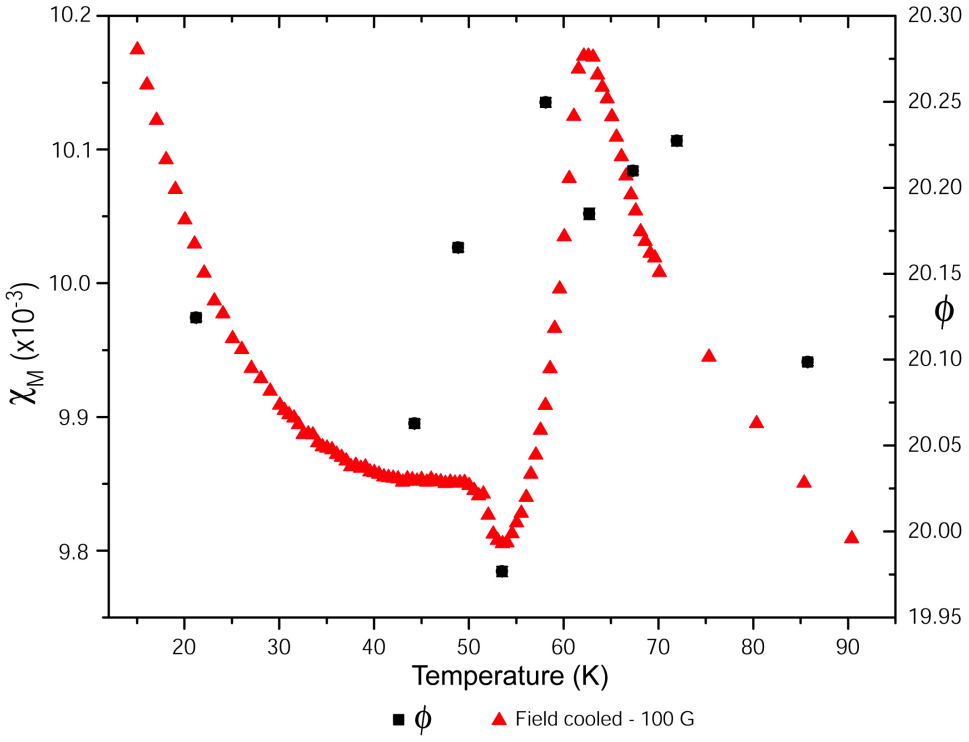

Figure 8.10: The data shows the change in angle ϕ as the sample is warmed from 15 K to 85 K with 5 K intervals between 40 and 75 K. Any disorder in ϕ is unclear unfortunately because with 5 K steps being the smallest experimentally obtainable there are not sufficient data points to ellicit any further information.

8.4.3 Final conclusion

Studies of single crystals of the jarosites show a clear coupling between the magnetic behaviour and the crystal structure. The good agreement between the spin glass freezing temperature of the hydronium jarosites and the Néel temperature, T_{N_2}, of the non-hydronium jarosites indicate that both are driven by an anisotropy parameter related to the distortion of the Fe coordination octahedron. T_{N_1} in the non-hydronium members may be driven by a different energy scale.

Chapter 9

Neutron thermo-diffraction Studies

Powder neutron diffraction studies were carried on deuterated hydronium jarosite, deutronium jarosite, in an effort to determine whether the $(D_3O)^+$ units froze into an ordered configuration at low temperature. There have been many neutron scattering experiments on Fe-jarosites, both elastic and inelastic, however, these have predominately concerned potassium analogues [18, 169–171] rather than hydronium jarosite [21].

9.1 Method

Diffraction data were collected using the D20 diffractometer at the ILL. The sample was held in a 5.5 mm vanadium can with a filling depth of 50 mm.

9.2 Results

A Rietveld refinement was carried out and the fit is shown in Figure 9.1. The best fit that could be obtained required the introduction of a deuterium unit to generate deutronium ions. These are shown in Figure 9.2, though the atoms are displayed without the thermal parameters.

As part of the refinement the A-site oxygen was from (0,0,0) to (0,0,-0.01076) [21]. This did not improve or worsen the refinement and there was no chemical reason to move it off the special position. The addition of a deuterium atop of the apical oxygen on the sulphate group, improved the thermal parameters on the deuteri-

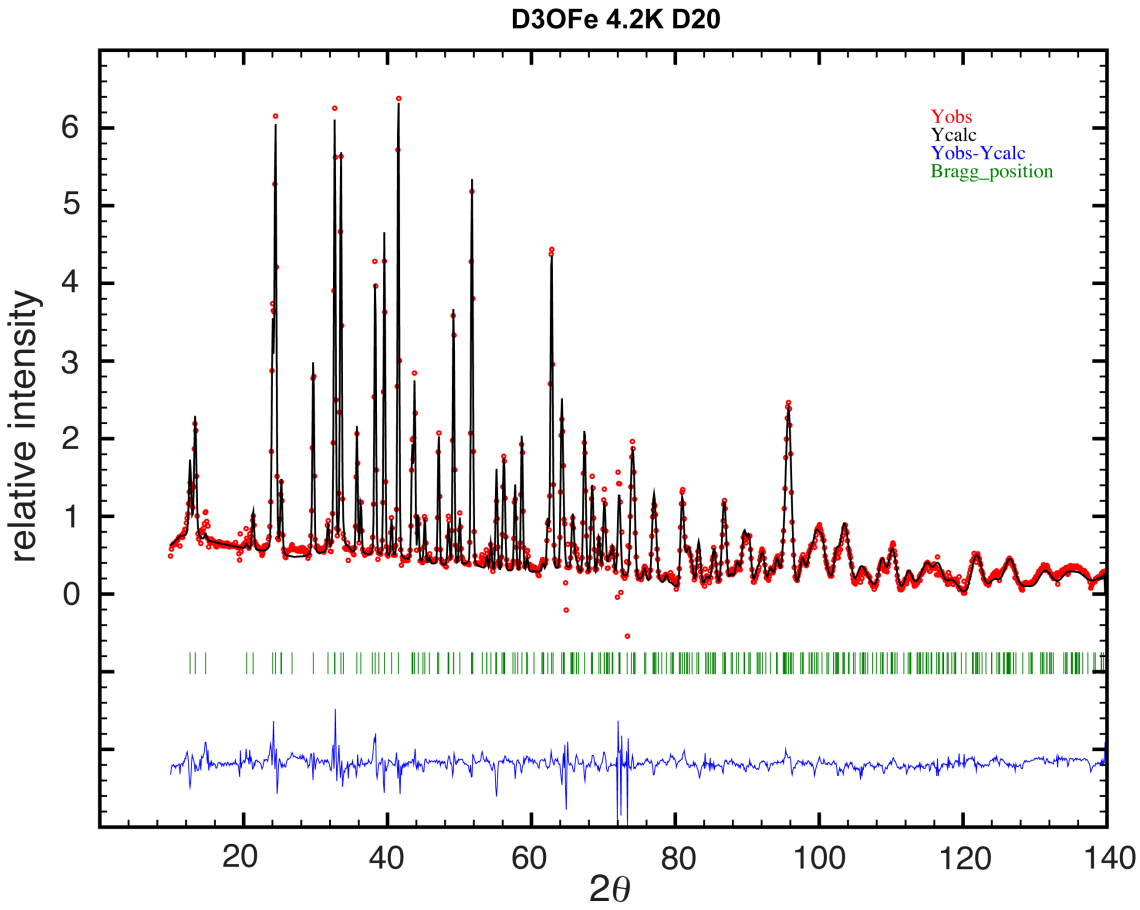

Figure 9.1: Rietveld fit for powder neutron data of hydronium (D_3O) jarosite at 4.2 K. The data were collected at ILL D20 using a wavelength of 1.3 Å using an orange cryostat. Fullprof was used for the Rietveld refinement, using profile function 5 - pseudo-Voigt. The statistics are, with the background: Rwp: 16.3, χ^2: 80.6 and DW: 1.5234.

ums that make up the $(D_3O)^+$ unit. Though this lead to a very unstable thermal parameter for the apical sulphate oxygen. Refining the $(D_3O)^+$ oxygen occupancy did reduce the thermal parameter on that oxygen, but no improvement to the refinement. There was no chemical reason for reducing the occupation either with regards to the conclusions drawn from the elemental analysis for the A-site oxygen and B-site Fe. There is a significant reduction on the synthesis yield when using D_2O, which may require elemental analysis to determine any differences (this will be difficult as oxygen composition is usually inferred from ICP-OES). The results from the refinement are shown below in Table 9.1.

Table 9.1: Atomic and cell parameters for Deuteriated D_3O jarosite at 4.2 K. Data were collected on the D20 instrument at the ILL at 1.3 Å. The space group is $R\bar{3}m$ with a unit cell of $a = b = 7.34940(10)$ Å and $c = 16.9411(4)$ Å. The R_{wp} value is 0.0231.

atom	x	y	z	B_{iso}	Multiplicity
O1	0	0	0	3.255(458)	3
Fe2	$\frac{1}{2}$	0	$\frac{1}{2}$	0.667(53)	9
S3	0	0	0.30925(72)	0.415(197)	6
O4	0.12796(34)	-0.12796(34)	0.13490(30)	0.996(71)	18
D5	0.19451(43)	-0.19451(43)	0.10586(32)	2.906(191)	18
O6	0.44659(63)	0.22335(31)	0.05384(22)	0.771(73)	18
O7	0	0	0.39467(47)	0.817(107)	6
D2	0.51536(446)	0.25770(223)	0.37906(158)	16.283(999)	9

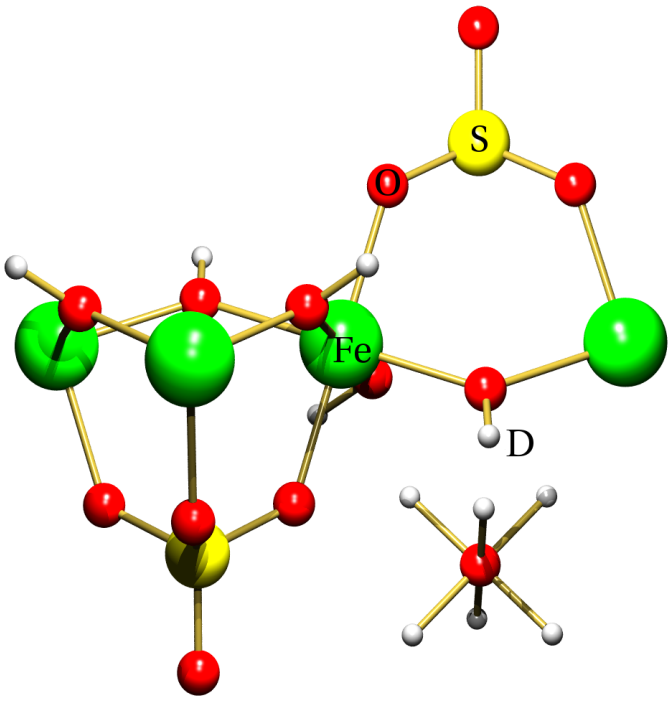

Figure 9.2: The crystal structure of hydronium (D_3O) jarosite at 4.2 K. Data were collected on the D20 using a wavelength of 1.3 Å. It clearly shows that the deuterium atoms have begun to freeze into a three-fold position with the deuterium atoms pointing towards the O–D bond of the bridging hydroxyl groups. The oxygen in the D_3O unit resides on the inversion centre and there is little evidence for this to shift from this site, therefore three more deuteriums positions are possible. The likelihood is for the D atoms to be evenly distributed between these 6 possible sites. A very large thermal displacement parameter suggests smearing of this D atoms about these positions but does indicate the presence of a crystallographic distortion upon freezing of the D_3O unit.

The results from Table 9.1 are shown in Figure 9.2. The main point of interest are the values of B_{iso}: for atom D2 it would suggest a smearing of the deuteriums in around that position. The conclusion to be drawn is that the $(D_3O)^+$ unit is still mobile and not frozen far below the magnetic transition. This would suggest that hydrogen bonding within the 12 coordinate site has little to do with the magnetism and that the differing transitions are attributed to an anisotropy generated from within the Fe co-ordination octahedra.

Chapter 10

Conclusions

The iron jarosites show a remarkable array of differing magnetic interactions. In this thesis it is shown that the cross-over between long-range magnetic order and an unconventional spin glass phase can be induced by changing the cations of the A-site. The selection of these ground states is controlled by structural changes of the Fe coordination octahedron with the greater distortion resulting in long range order.

Fe jarosite formation is very sensitive to the synthesis conditions. Investigating the synthesis conditions showed there are two mechanisms to the formation of jarosites: the oxidation method which produces samples with near perfect stoichiometry and macroscopically large single crystals; and forced hydrolysis, which produces hydronium jarosite, and provided a means to alter the composition of the jarosites, and in turn their magnetic properties. Comparing the two routes clearly demonstrated that it is not Fe coverage, but the nature of the A-site cation which defines the magnetic properties.

All the Fe jarosites display very large values of the Curie-Weiss temperature ($\sim -1500\,\mathrm{K}$), indicating spin-spin correlations persist at temperatures far above the transition temperatures (12-60 K), regardless of the magnetic ordering displayed. This implies that the magnetic exchange between the Fe^{3+} ions of the *kagomé* network are very similar throughout the Fe jarosites.

The different types of magnetic transitions displayed by the Fe-jarosites arise from an anisotropy upon the *kagomé* network. The nature of this anisotropy was investigated within the hydronium jarosites by magnetisation hysteresis experiments. There is no displacement with respect to applied field, pointing towards the presence of crystal electric field anisotropy rather than the DMI.

The non-hydronium jarosites have been found in previous work to order to a Néel state. This project has shown that the two transitions ($T_{N_1} \sim 65\,K$, $T_{N_2} \sim 55\,K$) displayed by the non-hydronium jarosites are affected differently with increasing uptake of the hydronium ion into the A-site: the higher temperature transition is destroyed and only a broadened transition at a lower temperature ($\sim 45\,K$) remains. Increase in the hydronium content also leads to a contraction in the c parameter of the crystal lattice.

Single crystal X-ray diffraction studies revealed a correlation between the rotation of the Fe co-ordinated octahedra away from co-linearity with the c axis and the transition temperatures defined by the angle ϕ. A more precise dependence was found by measuring the distortion of the Fe-octahedra away from uniformity, defined by the ratios of the Fe-O equatorial and apical bonds. Greater distortion corresponds to higher spin glass freezing temperatures. Extrapolation revealed that this relationship extends to T_{N_2}. The driver behind this spin glass transitions in hydronium jarosite is therefore an anisotropy rather than disorder of the magnetic sites. This conclusion is reinforced by the chemical analyses of the different hydronium and non-hydronium jarosites.

Appendix A

Inductively Coupled Plasma Elemental Analysis Techniques

A.1 Introduction to Inductively Coupled Plasma

The use of Inductively Coupled Plasma (ICP) as a technique to provide elemental analysis was developed through research into uranium. There are two methods of elemental analysis using IC: the first involves producing ions from the sample to be analysed and pass them through a mass spectrometer (MS), the second records the atomic emission spectra (AES). Both have their advantages: ICP-MS is very sensitive and is useful to measure trace elements within a sample and has an error of about 10%; however, the concentrations measured are in ppb. ICP-AES is more useful for bulk elemental analysis and gives a very low error of about 0.1% but concentrations are measured in ppm. A detailed description for both ICP-MS [158] and ICP-AES [181] can be found in the book, *Modern analytical geochemistry edited* [182]. Only ICP-AES was used to analyse jarosite samples and this appendix will concentrate on ICP-AES.

The plasma is generated by the induction of an electric current of a radio frequency to argon gas passing through a copper coil. This produces ionisation and a breakdown leading to the formation of a plasma, reaching temperatures of 10 000 K at the core. The temperatures inside a plasma of argon are sufficient to ionise most elements that are introduced into the plasma for elemental analysis yet is cheaper than helium as a large flow rate is needed. The argon gas is introduced through a quartz tube before the copper coil. Inside, running along the centre of the tube is a second very thin quartz tube where the nebulized sample solution is mixed in

with argon gas. A small amount (volume similar to a pipette drop) is introduced to prevent extinguishing the plasma. A third quartz tube sheaths the first tube and argon gas flows in the gap between the two tubes to cool down the first quartz tube.

A.1.1 Acquisition of the ions for elemental analysis

Specially designed cones made from nickel are inserted into the plasma pointing towards the plasma flame which help separate the ions to be measured from the argon. A small aperture in the centre of the cone, approximately 0.5 mm for AES, allows only those elements for analysis to pass through for the atomic emission spectra to be measured whilst minimising the number of surrounding argon ions. The cone for the AES is positioned further from the centre, in a cooler part of the plasma flame to measure the spectra resulting from electronic transitions. AES measurements are taken directly from the emission spectra using sophisticated optics. The AES technique gathers spectral information simultaneously and is ideal to obtain large elemental percentage weight values very accurately within a sample.

A.1.2 Calibration

Calibration is imperative for this technique. Standards of the elements to be analysed at various concentrations - ppm concentration are used for AES - are measured and a calibration curve of counts per second against concentration are plotted for each element by subtracting a blank background from the standards. Ideally, a linear fit through each of the points is required; the better the fit, the more accurate the results will be. The calibration curves also set the limits for the maximum and minimum concentration values that can be measured with confidence. Measurements of concentrations above the maximum on the calibration curve will assume that the straight line fit can be extrapolated.

Throughout the course of an extensive set sample measurements, the machine will drift: for example, fluctuations in room temperature will slightly alter the configuration. The other contributing factor during the measurement of samples that can cause a drift in calibration is the performance of the peristalsis pump. This draws up the sample into the plasma chamber and the precision of the volume sprayed into the chamber may alter throughout a run of measurements. A drift monitor was placed between every 10 samples to measure changes in calibration.

Calibration for some elements may be more problematic; some elements poorly

ionise, for instance only 30% of phosphorus ionises. Although allowing for a weighting of ionisation, lighter elements are still slightly under counted: because of their lighter mass they have a greater radial axial distribution as they travel through the plasma flame and thus are more likely to be deflected by the nickel cone or caught in the charged net.

A.1.3 Sample Preparation

Good sample preparation is crucial for ICP analysis as many of the errors in a measurement may come from human error. Both ICP methods require solutions which involve complicated processes to ensure that all the sample is dissolved and to minimise interference (explained below). The following method was used for jarosite digestion [14]: dissolve 60mg of jarosite sample in approximately $5cm^3$ aqua regia, warming on a heating bath until dissolved. The solution was then made up to $25cm^3$ using a 2% HNO_3 solution. 2% HNO_3 is required to achieve the right viscosity to pass through the ICP machine. The blank must also go through the same process of preparation.

A.1.4 Sources of Errors

- **Human error** A large source of error comes from sample preparation. For example in weighing and measuring. Loss of sample during the process necessary to produce a homogeneous solution for elemental analysis, usually through the solution spitting or evaporating whilst on the hotplate. Other source of human error is poor calibration of the instrumentation and measurements.

- **Systematic errors** The two most common are linked to the injection of the sample into the plasma flame. The most widely used method for uptake of the prepared solution into the machine is through a peristalsis pump, although highly efficient, the very nature of the mechanism of delivery may not provide a continuous flow into the nebulizer which in turn is another source of error. Only 1-2% of the sample which reaches the nebulizer is actually turned into a spray and the volume of spray is never constant.

- **Systemic errors "interference"** Considerable errors can come from the properties of the plasma and because its flame is open to atmosphere.

A problem with ICP-AES can be a possible overlap with the spectral lines, that should be resolved with higher resolution instruments. Sulphur represents a major difficulty, as its spectral line appears in the UV range and is at the limit for the optics (mechanical problems from scanning such a large range), but also importantly, the UV is absorbed by oxygen present in the machine and thus will reduce the intensity of the signal. In order to reduce this, the analysis would have to be carried out under a low atmospheric pressure environment which requires a larger flow rate of argon.

Another limitation with the ICP-AES comes with high percentage weight of atoms which can be easily ionised. As the cone for ICP-AES is in the cooler part of the flame light ions like potassium or sodium may undergo electronic transitions and emit emissions before passing through the cone and therefore a slight drop in intensity may be noticed for such elements.

A.1.5 Collection of results

ICP-AES results were collected on two different machines. A commercial service using the Varian Vista-Pro ICP-AES with a simultaneous solid-state detector at the Natural History Museum. Here the results were returned as percentage weight and as a service the preparation and result collection was undertaken by the machine operator. The solutions were dissolved in HCl following the method set out by A.M. Smith [14]. The ICP-AES ran with a high argon flow (low oxygen) and the optics were fully functional. The second machine was a Perkin-Elmer ICP-AES at Kingston university. Two batches of samples were run, as there was uncertainty in the sulphur being adequately being detected in the first batch.

The results from the experiment were returned as ppm and were converted as a weight percentage. This requires normalisation to an element. Oxygen is not recorded because of the air content and thus to work out the chemical formula the assumption is that the sulphate is always in full occupation for jarosites which has the value of 2.

Bibliography

[1] U. Becker and B. Gasharova, Physics and Chemistry of Materials **28**, 545 (2001).

[2] J. E. Dutrizac, Metallurgical And Materials Transactions B-Process Metallurgy And Materials Processing Science **14**, 531 (1983).

[3] J. E. Dutrizac and S. Kaiman, The Canadian Mineralogist **14**, 151 (1976).

[4] J. E. Dutrizac, J. L. Jambor, and T. T. Chen, Canadian Metallurgical Quarterly **26(2)**, 103 (1987).

[5] J. E. Dutrizac and J. L. Jambor, Hydrometallurgy **17**, 251 (1987).

[6] J. E. Dutrizac and J. L. Jambor, Canadian Metallurgical Quarterly **26(2)**, 91 (1987).

[7] J. E. Dutrizac and J. L. Jambor, Reviews in Mineralogy and Geochemistry **40**, 405 (2000).

[8] J. E. Dutrizac and O. Dinardo, J. Met. **35**, 96 (1983).

[9] J. E. Dutrizac and T. T. Chen, The Canadian Mineralogist **19**, 559 (1981).

[10] J. E. Dutrizac and T. T. Chen, Canadian Metallurgical Quarterly **39**, 1 (2000).

[11] J. E. Dutrizac, in *Hydrometallurgical Process Fundamentals*, edited by R. G. Bautista (Plenum Press, New York, -, 1984), Chap. The Behaviour of impurites during jarosite precipitation, pp. 125 – 169.

[12] J. Kubisz, Mineralogia Polonica **1**, 47 (1970).

[13] J. Jambor and J. Dustrizac, The Canadian Mineralogist **21**, 101 (1983).

[14] A. M. L. Smith, Ph.D. thesis, University of London, 2004.

[15] A. M. L. Smith, K. A. Hudson-Edwards, W. E. Dubbin, and K. Wright, Geochimica Et Cosmochimica Acta **70**, 608 (2006).

[16] K. Sasaki and H. Konno, The Canadian Mineralogist **38**, 45 (2000).

[17] B. Gasharova, J. Gottlicher, and U. Becker, Chem. Geol. **215**, 499 (2004).

[18] M. G. Townsend, G. Longworth, and E. Roudaut, Physical Review B **33**, 4919 (1986).

[19] S. A. Earle, A. P. Ramirez, and R. J. Cava, Physica B-Condensed Matter **262**, 199 (1999).

[20] D. Grohol, D. G. Nocera, and D. Papoutsakis, Physical Review B **67**, 064401 (2003).

[21] A. S. Wills and A. Harrison, Journal Of The Chemical Society-Faraday Transactions **92**, 2161 (1996).

[22] A. S. Wills, A. Harrison, C. Ritter, and R. I. Smith, Physical Review B **61**, 6156 (2000).

[23] J. A. Ripmeester, C. I. Ratcliffe, J. E. Dutrizac, and J. L. Jambor, The Canadian Mineralogist **24**, 435 (1986).

[24] W. Bisson and A. S. Wills, Zeitschrift fur Kristallographie Supplement **26**, 511 (2007).

[25] J. G. Bednorz and K. A. Muller, Zeitschrift fr Physik B Condensed Matter **64**, 189 (1986).

[26] P. W. Anderson, Science **256**, 1526 (1992).

[27] P. W. Anderson, Science **235**, 1196 (1987).

[28] P. W. Anderson and E. Abrahams, Nature **327**, 363 (1987).

[29] J. E. Greedan, Journal Of Materials Chemistry **11**, 37 (2001).

[30] A. P. Ramirez, Nature **421**, 483 (2003).

[31] A. P. Ramirez, Annual Reviews in Material Science **24**, 453 (1994).

[32] M. J. Harris, S. T. Bramwell, D. F. McMorrow, T. Zeiske, and K. W. Godfrey, Physical Review Letters **79**, 2554 (1997).

[33] S. T. Bramwell and M. J. P. Gingras, Science **294**, 1495 (2001).

[34] S. H. Lee, C. Broholm, W. Ratcliff, G. Gasparovic, Q. Huang, T. H. Kim, and S. W. Cheong, Nature **418**, 856 (2002).

[35] V. Cannella and J. A. Mydosh, Physical Review B **6**, 4220 (1972).

[36] A. S. Wills, V. Dupuis, E. Vincent, J. Hammann, and R. Calemczuk, Physical Review B **62**, R9264 (2000).

[37] A. S. Wills, Can. J. Phys. **79**, 1501 (2001).

[38] P. C. Singer and W. Stumm, Science **167**, 1121 (1970).

[39] A. W. Rose and C. A. Cravotta III, in *Coal Mine Drainage Prediction and Prevention in Pennsylvania*, edited by K. B. C. Brady, M. W. Smith, and J. Schueck (Pennsylvania Department for Enviromnetal Protection, -, 1998), Chap. Geochemistry of coal mine drainage.

[40] A. Blanco and J. M. Luzon, Antiquity **43**, 124 (1969).

[41] J. E. Dutrizac, J. L. Jambor, and J. B. O'Reilly, CIM Bulletin **76**, 78 (1983).

[42] N. F. Gray, Water Research **30**, 1551 (1996).

[43] N. F. Gray, Environmental Geology **27**, 358 (1996).

[44] N. F. Gray, Water Research **32**, 2122 (1998).

[45] L. A. Baker, A. T. Herlihy, P. R. Kaufmann, and J. M. Eilers, Science **252**, 1151 (1991).

[46] M. E. E. Madden, R. J. Bodnar, and J. D. Rimstidt, Nature **431**, 821 (2004).

[47] K. M. Scott, American Mineralogist **75**, 1176 (1990).

[48] U. Schwertmann and R. M. Cornell, *Iron Oxides in the Laboratory: preparation and Characterization* (Wiley and Sons, -, 2000).

[49] G. Klingelhofer, R. V. Morris, P. A. De Souza, D. Rodionov, and C. Schroder, Hyperfine Interactions **170**, 169 (2006).

[50] C. J. Serna, C. P. Cortina, and J. V. G. Ramos, Spectrochimica Acta **42A**, 729 (1986).

[51] G. M. Loiacono, G. Kostecky, and J. S. White, American Mineralogist **67**, 406 (1982).

[52] W. Gilbert, in *De Magnete, Magneticisque Corporibus et de Magno Magnete Tellure (Facsimile of 1893 Mottelay translation)*, edited by P. F. Mottelay (Dover Publications, -, 1600).

[53] L. Neel, Annales de Physique (Paris) **3**, 137 (1948).

[54] J. A. Mydosh, *Spin Glasses: An Experimental Introduction* (Taylor and Francis, -, 1993).

[55] J. N. Onuchic, Z. LutheySchulten, and P. G. Wolynes, Annual Review Of Physical Chemistry **48**, 545 (1997).

[56] K. H. Fischer and J. A. Hertz, *Spin Glasses* (Cambridge University Press, -, 1991).

[57] P. Bonville, V. Dupuis, E. Vincent, P. E. Lippens, and A. S. Wills, Hyperfine Interactions **168**, 1085 (2006).

[58] A. S. Wills, Physical Review B **6305**, 064430 (2001).

[59] A. S. Wills, G. S. Oakley, D. Visser, J. Frunzke, A. Harrison, and K. H. Andersen, Physical Review B **6409**, 094436 (2001).

[60] A. S. Wills, A. Harrison, S. A. M. Mentink, T. E. Mason, and Z. Tun, Europhysics Letters **42**, 325 (1998).

[61] A. S. Wills, Ph.D. thesis, University of Edinburgh, 1996.

[62] D. Grohol, K. Matan, J.-Y. Cho, S.-H. Lee, J. W. Lynn, D. G. Nocera, and Y. S. Lee, Nature Materials **4**, 323 (2005).

[63] D. Grohol and D. G. Nocera, Journal Of The American Chemical Society **124**, 2640 (2002).

[64] R. L. Carlin, *Magneto Chemistry* (Springer-Verlag, -, 1986).

[65] B. M. Bartlett and D. G. Nocera, J. Am. Chem. Soc **127**, 8985 (2005).

[66] T. Moriya, Phys. Rev. **120**, 91 (1960).

[67] I. E. Dzyaloshinski, JETP Lett **47**, 750 (1988).

[68] J. M. Kosterlitz and D. J. Thouless, J. Phys. C **6**, 1181 (1973).

[69] J. Villain, Phys. Rev. B **33**, 31 (1979).

[70] G. Toulouse, Commun Phys **2**, 115 (1977).

[71] J. Bardeen, L. N. Cooper, and J. R. Schrieffer, Phys. Rev. **108**, 1175 (1957).

[72] P. W. Anderson, P. A. Lee, M. Randeria, T. M. Rice, N. Trivedi, and F. Zhang, Journal of Physics: Condensed Matter **16**, R755 (2004).

[73] J. Kondo, Progress Of Theoretical Physics **32**, 37 (1964).

[74] M. A. Ruderman and C. Kittel, Physical Review **96**, 99 (1954).

[75] K. H. Fischer and J. A. Hertz, in *Spin Glasses*, edited by D. Edwards and D. Melville (Cambridge University Press, ADDRESS, 1991).

[76] J. D. Reger, W. Kinzel, and K. Binder, Phys. Rev. B **30**, 4028 (1984).

[77] R. Mathieu, Ph.D. thesis, University of Uppsala, 2002.

[78] S. F. Edwards and P. W. Andersen, J. Phys. F. **5**, 965 (1975).

[79] D. Sherrington and S. Kirkpatrick, Phys. Rev. Lett. **35**, 1972 (1975).

[80] S. Miyashita and H. Kawamura, J. Phys. Soc. Jpn. **54**, 3385 (1985).

[81] J. T. Chalker, P. C. W. Holdsworth, and E. F. Shender, Phys. Rev. Lett. **68**, 855 (1992).

[82] S. Bekhechi and B. W. Southern, Phys. Rev. B **67**, 144403 (2003).

[83] N. Elstner and A. P. Young, Phys. Rev. B **50**, 6871 (1994).

[84] I. Ritchey, P. Chandra, and P. Coleman, Phys. Rev. B **47**, 15342 (1993).

[85] A. Kuroda and S. Miyashita, J. Phys. Soc. Jpn. **64**, L4509 (1995).

[86] M. Elhajal, B. Canals, and C. Lacroix, Phys. Rev. B **66**, 014422 (2002).

[87] J. N. Reimers and A. J. Berlinsky, Phys. Rev. B **48**, 9539 (1991).

[88] E. F. Shender, V. B. Cherepanov, P. C. W. Holdsworth, and A. J. Berlinsky, Phys. Rev. Lett. **70**, 3812 (1993).

[89] N. D. Mermin, Rev. Mod. Phys. **51**, 591 (1979).

[90] A. Chubukov, Physical Review Letters **69**, 832 (1992).

[91] A. B. Harris, C. Kallin, and A. J. Berlinsky, Phys. Rev. B **45**, 2899 (1992).

[92] P. Chandra and P. Coleman, Phys. Rev. Lett. **66**, 100 (1991).

[93] A. V. Syromyatnikov and S. V. Maleyev, Physical Review B **66**, 132408 (2002).

[94] A. Auerbach, *Interacting Electrons and Quantun Magnetism* (Springer-Verlag, N. Y., -, 1994).

[95] C. Broholm, G. Aeppli, G. P. Espionosa, and A. S. Cooper, Physical Review Letters **65**, 3173 (1990).

[96] A. P. Ramirez, G. P. Espionosa, and A. S. Cooper, Phys. Rev. Lett. **64**, 2070 (1990).

[97] X. Obradors, A. Labarta, A. Isalgue, J. Tejada, R. J., and M. Pernet, Solid State Communications **65**, 189 (1988).

[98] S. H. Lee, C. Broholm, G. Aeppli, T. G. Perring, B. Hessen, and A. Taylor, Physical Review Letters **76**, 4424 (1996).

[99] P. Mendels, A. Olariu, F. Bert, D. Bono, L. Limot, G. Collin, B. Ueland, P. Schiffer, R. J. Cava, N. Blanchard, F. Duc, and J. C. Trombe, Journal Of Physics-Condensed Matter **19**, 145224 (2007).

[100] J. S. Helton, K. Matan, M. P. Shores, E. A. Nytko, B. M. Bartlett, Y. Yoshida, Y. Takano, A. Suslov, Y. Qiu, J. H. Chung, D. G. Nocera, and Y. S. Lee, Physical Review Letters **98**, 107204 (2007).

[101] M. Hermele, Y. Ran, P. A. Lee, and X. G. Wen, Physical Review B **77**, 224413 (2008).

[102] O. Ma and J. B. Marston, Physical Review Letters **101**, 027204 (2008).

[103] M. A. de Vries, K. V. Kamenev, W. A. Kockelmann, J. Sanchez-Benitez, and A. Harrison, Physical Review Letters **100**, 157205 (2008).

[104] A. Zorko, S. Nellutla, J. van Tol, L. C. Brunel, F. Bert, F. Duc, J. C. Trombe, M. A. de Vries, A. Harrison, and P. Mendels, Physical Review Letters **101**, 026405 (2008).

[105] M. P. Shores, E. A. Nytko, B. M. Bartlett, and D. G. Nocera, Journal Of The American Chemical Society **127**, 13462 (2005).

[106] R. S. W. Braithwaite, K. Mereiter, W. H. Paar, and A. M. Clark, Mineralogical Magazine **68**, 527 (2004).

[107] T. Imai, E. A. Nytko, B. M. Bartlett, M. P. Shores, and D. G. Nocera, Physical Review Letters **100**, 077203 (2008).

[108] M. Rigol and R. R. P. Singh, Physical Review Letters **98**, 207204 (2007).

[109] M. Rigol and R. R. P. Singh, Physical Review B **76**, 184403 (2007).

[110] J. Frunzke, T. Hansen, A. Harrison, J. S. Lord, G. S. Oakley, D. Visser, and A. S. Wills, Journal Of Materials Chemistry **11**, 179 (2001).

[111] `http://www.daichem.co.jp/eng/products/ace_glass/ace_glass1_en.html`.

[112] R. Gill, in *Modern analytical geochemistry*, edited by R. Gill (Longman, -, 1997), Chap. Electron Beam Methods, pp. 206–214.

[113] C. Panagopoulos, M. Majoros, T. Nishizaki, and H. Iwasaki, Physical Review Letters **96**, 047002 (2006).

[114] C. Giacovazzo, H. L. Monaco, G. Artioli, D. Viterbo, G. Ferraris, G. Gilli, G. Zanotti, and M. Catti, in *Fundamentals of Crystallography*, edited by C. Giacovazzo (Oxford University Press, -, 2002).

[115] A. K. Cheetham and P. Day, in *Solid-State Chemistry Techniques*, edited by A. K. Cheetham and P. Day (Clarendon Press, Oxford, -, 1986).

[116] G. L. Squires, *Introduction to the Theory of Thermal Neutron Scattering* (Dover Publications, -, 1997).

[117] H. M. Rietveld, Acta Cryst. **22**, 151 (1967).

[118] H. M. Rietveld, Journal Of Applied Crystallography **2**, 65 (1969).

[119] R. A. Young, in *The Rietveld Method*, edited by R. A. Young (Oxford University Press, -, 1995).

[120] `http://www.ccp14.ac.uk/ccp/ccp14/ftp-mirror/gsas/public/gsas/manual/GSASManual.pdf`.

[121] A. R. Denton and N. W. Ashcroft, Phys. Rev. A **43**, 3161 (1991).

[122] B. H. Toby, Journal of Applied Crystallography **34**, 210 (2001).

[123] A. Larson and R. Von Dreele, Los alamos national laboratory report laur 86-748, Los Alamos National Laboratory (unpublished).

[124] L. W. Finger, D. E. Cox, and A. P. Jephcoat, Journal Of Applied Crystallography **27**, 892 (1994).

[125] `http://www.ill.eu/sites/fullprof/`.

[126] `http://wwwold.ill.fr/YellowBook/D20/NeutronOptics/Frame.html`.

[127] U. Shmueli, *Theories and techniques of crystal structure determination* (International Union of Crystallography (Oxford University Press), ADDRESS, 2007).

[128] G. M. Sheldrick, Technical report, Bruker AXS Inc. (unpublished).

[129] R. J. Cernik, W. Clegg, C. R. A. Catlow, G. Bushnell-Wye, J. V. Flaherty, G. N. Greaves, M. Hamichi, I. Burrows, D. J. Taylor, and S. J. Teat, J. Synchotron Radiation **4**, 279 (1997).

[130] B. A. Inc, Bruker SMART APEX2 CCD diffractometer, 2004.

[131] B. A. Inc, Data reduction and Cell refinement, 2004.

[132] G. M. Sheldrick, Acta Crystallographica Section A **64**, 112 (2008).

[133] L. J. Farrugia, J. Appl. Cryst. **32**, 837 (1999).

[134] A. L. Spek, Journal Of Applied Crystallography **36**, 7 (2003).

[135] A. L. Spek, PLATON, A Multipurpose Crystallographic Tool, 1998.

[136] J. Majzlan, R. Stevens, J. Boerio-Goates, B. Woodfield, A. Navrotsky, P. Burns, M. Crawford, and T. Amos, Physics and Chemistry of Minerals **31**, 518 (2004).

[137] A. Taroni, Master's thesis, University College London, 2003.

[138] R. M. Ziff and B. Sapoval, J. Phys. A: Math. Gen. **19**, L1169 (1986).

[139] R. M. Ziff and P. N. Suding, Journal Of Physics A-Mathematical And General **30**, 5351 (1997).

[140] K. Kandori, T. Shigetomi, and T. Ishikawa, Colloids And Surfaces A-Physicochemical And Engineering Aspects **232**, 19 (2004).

[141] Y. Umetsu, K. Tazawa, and K. Sasaki, Canadian Metallurgical Quarterly **16**, 111 (1977).

[142] G. W. Morrison, G. S. Teale, and I. Hodkinson, in *Pacific Rim Congress 87: Geology and gold mineralization at Mount Leyshon, North Queensland, Australia*, edited by P. R. Congress (Parkville: Australina Institue for Mining, -, 1987).

[143] J. L. Jambor, D. K. Nordstrom, and C. N. Alpers, Reviews in Mineralogy and Geochemistry **40**, 303 (2000).

[144] N. Lazaroff, W. Sigal, and A. Wasserman, Applied and Enviromental Microbiology **43**, 924 (1982).

[145] B. Breidenstein, J. Schluter, and G. Gebhard, Neues Jahrbuch fur Mineralogie-Monatshefte **5**, 213 (1992).

[146] J. Szymanski, The Canadian Mineralogist **26**, 923 (1988).

[147] K. Kandori, J. Sakai, and T. Ishikawa, Physical Chemistry Chemical Physics **2**, 3293 (2000).

[148] S. Music, Z. Orehovec, S. Popovic, and J. Czakonagy, Journal of Materials Science **29**, 1991 (1994).

[149] D. Baron and C. D. Palmer, Geochimica Et Cosmochimica Acta **60**, 185 (1996).

[150] J. M. Bigham, L. Carlson, and E. Murad, Mineralogical Magazine **58**, 641 (1994).

[151] S. Shimizu and H. Hamada, Angew. Chem. Int. Ed. **38**, 2725 (1999).

[152] M. Wildner and G. Giester, Neues Jahrbuch Fur Mineralogie-Monatshefte **7**, 296 (1991).

[153] J. Rodriguez-Carvajal, Physica B: Condensed Matter **192**, 55 (1993).

[154] T. Roisnel and J. Rodriguez-Carvajal, Epdic 7: European Powder Diffraction, Pts 1 And 2 **378-3**, 118 (2001).

[155] A. A. Zavitsas, Journal of Physical Chemistry B **105**, 7805 (2001).

[156] V. Dupuis, E. Vincent, J. Hammann, J. E. Greedan, and A. S. Wills, Journal of Applied Physics **91**, 8384 (2002).

[157] R. Moessner and A. J. Berlinsky, Physical Review Letters **83**, 3293 (1999).

[158] K. E. Jarvis, in *Modern analytical geochemistry*, edited by R. Gill (Longman, -, 1997), Chap. Inductively coupled plasma-mass spectrometry, pp. 171–187.

[159] D. Grohol and D. G. Nocera, Chemistry Of Materials **19**, 3061 (2007).

[160] P. G. Drazin and R. S. Johnson, *Solitons: an introduction* (Cambridge University Press, -, 1989).

[161] W. W. Rudolph, R. Mason, and P. Schmidt, European Journal Of Mineralogy **15**, 913 (2003).

[162] L. C. Basciano and R. C. Peterson, American Mineralogist **92**, 1464 (2007).

[163] K. A. Hudson-Edwards, A. M. L. Smith, W. E. Dubbin, A. J. Bennett, P. J. Murphy, and K. Wright, European Journal Of Mineralogy **20**, 241 (2008).

[164] A. S. Wills, A. M. L. Smith, W. E. Dubbin, K. A. Hudson-Edwards, and K. Wright, Journal Of Magnetism And Magnetic Materials **272-76**, 1300 (2004).

[165] W. Mumme and T. Scott, American Mineralogist **51**, 443 (1966).

[166] J. T. Szymanski, The Canadian Mineralogist **23**, 659 (1985).

[167] A. M. L. Smith, K. A. Hudson-Edwards, W. E. Dubbin, and K. Wright, Applied Geochemistry **21**, 1251 (2006).

[168] S. Menchetti and C. Sabelli, Neues Jahrbuch Fur Mineralogie-Monatshefte **9**, 406 (1976).

[169] T. Inami, S. Maegawa, and M. Takano, Journal Of Magnetism And Magnetic Materials **177**, 752 (1998).

[170] K. Matan, D. Grohol, D. G. Nocera, T. Yildirim, A. B. Harris, S. H. Lee, S. E. Nagler, and Y. S. Lee, Phys. Rev. Lett. **96**, 247201 (2006).

[171] F. C. Coomer, A. Harrison, G. S. Oakley, J. Kulda, J. R. Stewart, J. A. Stride, B. Fak, J. W. Taylor, and D. Visser, Journal of Physics-condensed Matter **18**, 8847 (2006).

[172] T. Yildirim and A. B. Harris, Phys. Rev. B **73**, 214446 (2006).

[173] M. A. de Vries, T. K. Johal, A. Mirone, J. S. Claydon, G. J. Nilsen, H. M. Ronnow, G. van der Laan, and A. Harrison, Physical Review B **79**, 045102 (2009).

[174] A. Abragam and B. Bleaney, Technical report, Oxford (unpublished).

[175] S. Geshwind, Phys. Rev. **121**, 363 (1961).

[176] A. M. Afanasev, V. D. Gorobchenko, D. S. Kulgawczuk, and I. I. Lukashevich, Phys. Stat. Solidi (a) **26**, 697 (1974).

[177] S. H. Lee, C. Broholm, M. F. Collins, L. Heller, A. P. Ramirez, C. Kloc, E. Bucher, R. W. Erwin, and N. Lacevic, Physical Review B **56**, 8091 (1997).

[178] T. Inami, T. Morimoto, M. Nishiyama, S. Maegawa, Y. Oka, and H. Okumura, Physical Review B **6405**, 054421 (2001).

[179] T. Morimoto, M. Nishiyama, S. Maegawa, and Y. O., The Physcial Society of Japan **72**, 2085 (2003).

[180] A. Keren, K. Kojima, L. P. Le, G. M. Luke, W. D. Wu, Y. J. Uemura, T. Takada, H. Dabkowska, and M. J. P. Gingras, Physical Review B **53**, 6451 (1996).

[181] J. N. Walsh, in *Modern analytical geochemistry*, edited by R. Gill (Longman, ADDRESS, 1997), Chap. Inductively coupled plasma-atomic emission spectrometry, pp. 41–66.

[182] R. Gill, in *Modern analytical geochemistry*, edited by R. Gill (Longman, -, 1997).